Heterogeneity and Flow in the Deep Earth

by

Sanne Cottaar

A dissertation submitted in partial satisfaction of the
requirements for the degree of
Doctor of Philosophy

in

Earth and Planetary Science

in the

GRADUATE DIVISION
of the
UNIVERSITY OF CALIFORNIA, BERKELEY

Committee in charge:
Professor Barbara Romanowicz, Chair
Professor Bruce Buffett
Professor Stephen Morris

Spring 2013

Heterogeneity and Flow in the Deep Earth

Abstract

Heterogeneity and Flow in the Deep Earth

by

Sanne Cottaar

Doctor of Philosophy in Earth and Planetary Science

University of California, Berkeley

Professor Barbara Romanowicz, Chair

Over the past half century, study of deep regions in the Earth has revealed them to be complex and dynamic. Much of our knowledge comes from seismological data, and ultimately these observations need to be linked to results from geodynamics and mineral physics in order to make inferences about compositional heterogeneities and flow.

One example of a strongly-heterogeneous region is the lower thermal boundary layer of the mantle, i.e. the layer of several hundred kilometers thickness above the core-mantle boundary, commonly referred to as D″. This region appears to be characterized by two large provinces of distinctive slow shear velocities, 4000-5000 km across, one beneath the Pacific and one beneath Africa. Surrounding these regions, seismic velocities are faster, and often interpreted as corresponding to a graveyard of slabs. A recently discovered phase transition from perovskite to postperovskite may also occur in this depth range and has been associated with an intermittently observed seismic discontinuity at the top of D″. This study adds to the seismological evidence for complexities both in isotropic seismic velocities as well as in anisotropic velocities and how those can be linked to flow of material.

We map a distinctive small "pile" of slow shear velocity beneath Russia through direct

waveform evidence. This "pile" is less than 1000 km across, and thus much smaller than the Pacific and African provinces. Its height is several hundreds of kilometers and its velocity reduction suggests it is composed of the same material as the large provinces of slow shear velocity.

Beneath Hawaii, at the northern edge of the Pacific province, we find an extended thin zone of ultra-low velocities. This is the first time the three-dimensional extent of such a zone is constrained with some accuracy. The constraints on its morphology come from the presence of strong postcursors to shear waves diffracted along the core-mantle boundary, delayed by 30 to 50 seconds with respect to the main diffracted arrival. The zone is almost 1000 km across and roughly 25 km high. Its shear velocity is reduced by $\sim 20\%$ with respect to the global average, which is possible through strong iron enrichment or the presence of partial melt. Given its location, one can speculate that this zone may represent an anchor to a whole-mantle plume reaching the surface of the Earth beneath the Hawaiian hotspot and may also represent the source of geochemical anomalies in Hawaiian basalts.

Around the southern margin of the African low shear velocity province, we map strong variations in anisotropic velocity structure. These could be interpreted as evidence for strong flow outside the region of slow velocity, and insignificant flow within. To understand observations of seismic anisotropy in terms of flow in a more general context, we adopt a multi-disciplinary approach. We forward model anisotropic texture development through geodynamical models, reflecting mineral-physical constraints on the deformational behavior and elastic constants of possible compositions. In both two and three-dimensional models, we find that perovskite and post-perovskite result in distinctive anisotropic patterns. Deformation on different crystallographic lattice planes within post-perovskite also results in different signatures. In general, the presence of post-perovskite appears to best explain seismic observations of anisotropy in the deep mantle.

One other region of strong heterogeneous and anisotropic velocity variations is the inner core. In the last chapter, we model thermal histories to assess the possibility of episodes of convection over the course of the inner core growth. Our numerical model predicts strains due to convective flow that could cause texturing and seismic anisotropy. An early termination of this convection can explain the stronger anisotropy seen in the innermost inner core (the most central 500 km).

Professor Barbara Romanowicz
Dissertation Committee Chair

To my family

Contents

List of Figures

List of Tables

Acknowledgments

First and foremost, I would like to thank Prof. Barbara Romanowicz. You have inspired me and supported me. It has been a humble experience to work with you. You also have happened to organize the best conferences I have been to!

I also like to thank other advisors and committee members, Prof. Bruce Buffett, Prof. Rudy Wenk and Prof. Stephen Morris. Thank you for your continued support. You have taught me a lot. I am grateful for the collaborations with my other co-authors Prof. Allen McNamara, Mingming Li, Prof. Ved Lekic and Prof. Adam Dziewonski. It was a real pleasure to be part of Barbara's vibrant group. Thank you to all its current members (here and at IPG Paris) and those who have passed through.

None of this work would be possible without the exquisite support of the computer and administrative staff in our department. I would like to thank all the members of the Berkeley Seismological Laboratory and the wider Earth and Planetary Science department for creating a friendly, inspiring, science-driven community. I feel lucky to have been a part of this community.

I would like to thank all the amazing and interesting people I got to meet and spend time with over the years. Many of you have become dear friends and have kept me sane during set-backs. I won't list your names here, but you know who you are.

I would like to thank my family and friends abroad. Many of you came to visit, which has been a pleasure. Thank you mom and dad, you are my biggest supporters and have given me a wonderful youth. Thanks to my brothers and sister and families, you have created more than sufficient distractions from my work over the years. I would like to thank my grandparents for their love and support. Especially, Opa Heerlen, for being an inspiring geophysicist. Oma Geertje, I wish you were here to see this moment.

Thank you Californian sun, for all your warmth and light, for ripening lovely fruits and vegetables, and making outdoor swimming year-round a pleasure. I will miss you in England.

Chapter 1

Introduction

Many questions remain to be answered on the composition and dynamics of the interior of our planet. The deep Earth has proven to be a complex system that is both heterogeneous and dynamic; understanding its complexity requires collaboration between different fields studying the deep Earth, including seismology, geodynamics and mineral physics. The work here extends our knowledge of the seismic complexity of the lowermost mantle through new observations and seismic modeling (*Chapters 2-4*), while in *Chapters 5-6* we go further, explaining seismic observations in terms of dynamics from a multi-disciplinary point of view.

From tectonic activity on our surface, as well as geodynamical modeling and seismic mapping of the interior, we know the mantle is convecting. Igneous rocks bring up chunks of mantle material that inform us of the composition of the upper mantle, while geodetic and seismic measurements reveal the direction of flow. However, how that convection extends into the lower mantle is unknown. The question remains whether the mantle convects continuously throughout its entire depth or whether the mantle is dynamically layered with some degree of separate convection between the upper and lower mantle, making it more likely that the composition differs between these layers. To answer these questions, we primarily have to rely on observations of seismic waves that sample the deep Earth.

The general dynamics of mantle convection are understood (Ricard, 2007). The cooling of our planet drives convection in the rocky silicate mantle that surrounds the hot liquid iron-nickel outer core of the Earth. Cooling through conduction in the mantle is insufficient to transfer heat from the core, causing dynamic instabilities to originate at the core-mantle boundary. The core-mantle boundary region is the lower thermal boundary layer in mantle convection. Understanding the dynamics of this layer is crucial to the overall understanding of the dynamical and thermal history of our planet.

In the 1940s, Bullen produced one of the first seismic velocity profiles with depth (Bullen, 1947). This model showed a change in the velocity-gradient a few hundred kilo-

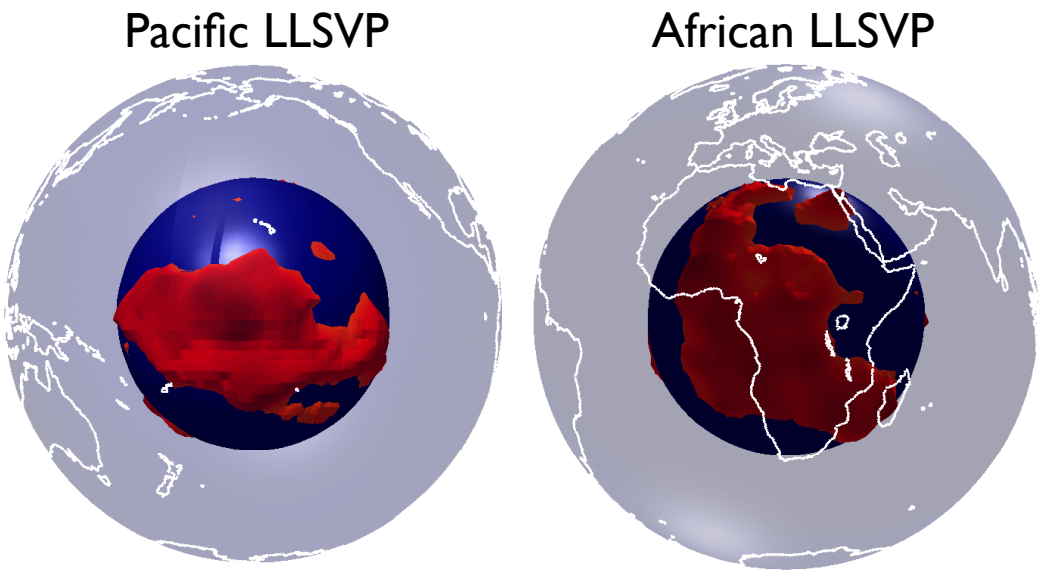

Figure 1.1: Cartoons depicting African and Pacific LLSVPs in red. The core is solid blue, while the continents are drawn on a transparent blue surface.

meters above the core-mantle boundary. Bullen was the first to characterize the lowermost mantle as a separate layer. In his model, Bullen labeled the different layers of the Earth alphabetically, naming the lower mantle the D-layer. Most of the lower mantle became the D$'$ layer, while the lowermost part was dubbed the D$''$ ('D-double-prime').

Currently, D$''$ is not only characterized by a change in gradient in the radial seismic velocity profile, but has in many ways appeared as a seismically strongly heterogeneous region. Global seismic tomography indicates that the spectrum of lateral heterogeneity increases near the bottom of the lower mantle. In the bottom 300-500 km of mantle tomographic images, the structure is dominated by pronounced long wavelengths variations (degrees 2 and 3 in a spherical harmonics expansion). This is caused by the presence of two large low shear velocity provinces (LLSVPs), also referred to as 'superplumes' or 'thermo-chemical piles' (e.g. Dziewonski et al., 2010; Lekic et al., 2012).

One of these LLSVPs is located beneath the south-central Pacific Ocean and the other under Africa (see Figure 1.1). Both are situated around the equator, but mainly in the southern hemisphere[1]. Shear wave velocities in the provinces are a few percent slower than in surrounding material. Local studies show that the edges of the LLSVPs are very sharp, with lateral gradients that are difficult to explain by variations in temperature alone (e.g. Ritsema et al., 1998; Bréger and Romanowicz, 1998; Wen et al., 2001; Ni et al., 2002; To et al., 2005; He and Wen, 2009). There are indications that the base of the LLSVPs might be denser than surrounding regions (e.g. Ishii and Tromp, 1999, 2004).

[1]Actually, roughly the same percentage of the LLSVPs is situated in the southern hemisphere as continental lithosphere at the surface on the northern hemisphere.

There is mounting evidence for lateral variations of structure at shorter scales than the LLSVPs. Localized zones of slow material, named ultra-low velocity zones (ULVZ, e.g. Garnero et al., 1998; Lay et al., 1998; Thorne and Garnero, 2004), have been found in various locations, mainly at the edges of LLSVPs (McNamara et al., 2010). Their shear wave velocity reductions with respect to surrounding material are on the order of tens of percent. The exact relationship of ULVZs to the edges of LLSVPs is still unclear (Garnero and McNamara, 2008; Rost et al., 2010).

Additional seismic observations make the D″ distinct from the rest of the lower mantle. While most of the lower mantle appears seismically isotropic, D″ has shown to be a region of strong seismic anisotropy (Lay et al., 1998; Kendall and Silver, 1998), i.e. the seismic wave speeds vary with direction of propagation and polarization. Observations of seismic anisotropy could be a direct indicator of mantle flow, as they appear to be in the uppermost mantle (e.g. Karato, 1998).

Seismic waves, when observed at large distances from the earthquake source, contain information on the heterogeneity and dynamics around the core-mantle boundary. In these studies we mainly use the shear phases that reflect ('ScS') and diffract ('Sdiff') on the core-mantle boundary. Large (Mw>6), deep (400-600 km) earthquakes are most suitable to study the deep Earth. One reason is that seismic complexities in the upper mantle on the source side do not complicate the observations of the deep mantle. Another is that possible postcursors (scattered waves that arrive later due to complexities) do not interfere with the depth phases (phases that travel upward from the source and then reflect off the surface). Deep earthquakes only occur in subduction zones around the globe, limiting the coverage; most are located in the ring of subduction around the Pacific. Besides the locations of suitable earthquakes, coverage is further limited by the location of seismic stations: arrays of seismic stations are especially valuable when looking for consistency in waveform complexities. The recent endeavor on station coverage has been USArray (IRIS), an array of 400 broadband stations that has been moving across the lower 48 states. This array has greatly improved the seismic coverage of the deep mantle beneath the central Pacific from deep subduction zone earthquakes in the southwest Pacific.

We observe many waveform complexities that can not be taken into account in standard tomographic models. Here we confirm the causes of these complexities by forward modeling full waveforms with the spectral element method. We use a computationally effective version that allows for strong 3D anomalies only in the lowermost mantle (Capdeville et al., 2003).

In *Chapter 2*, we introduce the most striking waveform complexities observed in diffracted shear waves ('Sdiff'). The shear waves originate at a deep earthquake near Papua New-Guinea and arrive at USArray in North America. In the lowermost mantle, these waves sample the central Pacific beneath Hawaii. At a specific azimuth range from the event, the wave energy refracts and scatters, arriving at the stations as postcursors roughly 30 to 50 seconds later than expected. From the observation of postcursors across the entire US-Array, we are able to map the three-dimensional structure that causes these complexities. The structure consists of a zone of slow material (a.k.a. an ultra-low-velocity-zone, ULVZ)

on the core-mantle boundary to the west of the Hawaiian Island Chain. The zone is about the size of Texas ($\sim$ 1000 km in diameter) and roughly 20-30 km high. The material in the zone reduces the speed of seismic shear waves by $\sim$ 20% compared to the surrounding material. We confirm the parameters of a cylindrical model representing the zone, and investigate their trade-offs, by forward-modeling the waveforms through the structure and reproducing the postcursors. One aspect about these complexities is that they only appear in waveforms with periods below 30 seconds. In other words, long-wavelength energy is not sensitive to the velocity reduction in the zone. This allows us to constrain the height of the structure. The frequency-dependence of the observation also explains why this zone is not seen in global tomography models, which are generally derived from seismic waves of periods longer than 30 seconds. Additionally inversion methods cannot include strong waveform complexities and infer strong anomalies.

The Perm anomaly is a slow-velocity anomaly that consistently appears across all global tomographic models. The Perm anomaly is located on the core-mantle boundary beneath the Russian city, Perm, and the Ural mountains. *Chapter 3* introduces direct observations of delayed and focused waveforms that propagate through this anomaly from the deep event beneath Spain to stations in Japan and Taiwan, as well as from Japan to stations in Northern Africa. The Perm anomaly has a lateral extent similar to the Hawaiian zone in the previous chapter. Even though its velocity reduction is a lot weaker, the anomaly shows up in all global tomographic models because its height: it extends hundreds of kilometers above the core-mantle boundary. The observations we make are also not constrained to a specific frequency range of the seismic waves. The anomaly in shear wave velocity appears weaker in global tomography than the African and Pacific LLSVPs. This could, however, be due to its smaller size, which causes the anomaly to be underestimated as a result of waveform healing. In our full-waveform modeling, which reflects wavefront healing effects, we show that the waveforms are consistent with the Perm anomaly having velocity reductions similar to the LLSVPs, implying that the anomaly could consist of similar compositionally distinctive material[2].

Besides isotropic velocity variations, we can also observe the presence of anisotropic velocities, i.e. different seismic velocities for different directions of propagation. In *Chapter 4* we utilize the polarization of shear-diffracted waves to observe strong variations in seismic anisotropy across the southern margin of the African LLSVP. A shear-diffracted wave that travels along the core-mantle boundary becomes horizontally polarized, as the vertically polarized component loses energy quickly due to interaction with the core. When the phase turns up from the core-mantle boundary its polarization can change again when it interacts with seismic anisotropy. In *Chapter 4* we observe and model elliptical polarizations that have interacted with an anisotropic medium at large distances for an event in Fiji to stations in Southern Africa. We can rule out the possibility that this is caused by seismic anisotropy in the upper mantle, leaving the lowermost mantle as the strongest candidate region for the presence of anisotropy. We model the type of anisotropy and confirm it by waveform modeling. The constraints of this data set are limited as data coverage is

[2]Whatever that might be...

only from one direction. Strikingly, the presence of anisotropy and elliptical polarizations decreases towards the LLSVP margin, and there is no apparent anisotropy within. This implies that there is a different flow regime inside and outside the African pile and further suggests compositionally distinctive piles.

Chapter 5 investigates the link between observed deep mantle seismic anisotropy and material flow in a multidisciplinary forward modeling approach. This includes collaboration with several geodynamicists and mineral physicists. The resolution of seismic observations is on the order of hundreds of kilometers; to come to a full understanding, the observations have to be linked to mineralogical knowledge (on a microscopic scale) through multi-scale modeling. We start from 2D and 3D geodynamical models of the mantle to constrain the deformation in a subducting slab that impinges on the core-mantle boundary. Next, we model the deformational behavior on a microscopic level as material flows, which results in a preferred orientation of the individual crystals. As the single crystals are intrinsically seismically anisotropic, their preferred orientation leads to seismic anisotropy on the macroscopic scale. We evaluate what anisotropy patterns are consistent with seismic observations. This study builds on the exciting discovery in 2004 of a mineral phase that might occur at pressures in the lowermost mantle, called 'post-perovskite' (Murakami et al., 2004; Oganov et al., 2005). Laboratory measurements of microscopic deformational behavior as well as seismic velocities of this phase are very recent. We observe that the deformational behavior in post-perovskite is most consistent with seismic observations, while the behavior of the alternative mineral phase, perovskite, is not consistent with seismic observations.

Besides the Earth's mantle, deep seismic anisotropy is observed in the inner core, with possibly stronger anisotropy in an innermost inner core. Even though some of the iron phases that could be stable there are intrinsically anisotropic, a mantle-like model of convection causing deformation creating anisotropy seems implausible since the inner core is not heated by a hotter inner sphere and is unlikely to have substantial radioactive heating from within. In *Chapter 6* we investigate the hypothesis of a convecting inner core. The inner core continues to grow through the freezing of iron at its surface[3](Buffett et al., 1996). If the growth of the inner core is faster than presently—as it is thought to be in its early stages— the inner core might not cool sufficiently through conduction. In that case, cold thermal instabilities can form at the top and sink to the center, creating convection. The speed of growth and the possible resulting convection depends on the rate of cooling at the top, which ultimately depends on the heat flux at the core-mantle boundary (as the outer core is vigorously convecting). The cooling also depends strongly on the conductivity of the inner core. As recent results on thermal conductivity of iron at inner core conditions show much higher values than previously thought (Pozzo et al., 2012), this mechanism becomes less plausible. If it occurs, though, it is more likely to happen early in the history of the inner core when growth was rapid. Early deformation through convection, and the later cessation of convection, might be an explanation for observations of a stronger seismic anisotropy in an innermost inner core.

[3]Presently at a rate on the order of 10^{11} kg/yr

Bibliography

Bréger, L., Romanowicz, B., 1998. Three-dimensional structure at the base of the mantle beneath the central Pacific. Science 282 (5389), 718–720.

Buffett, B. A., Huppert, H. E., Lister, J. R., Woods, A. W., 1996. On the thermal evolution of the Earths core. J. Geophys. Res 101, 7989–8006.

Bullen, K. E., 1947. An introduction to the theory of seismology. University Press, Cambridge.

Capdeville, Y., To, A., Romanowicz, B., 2003. Coupling spectral elements and modes in a spherical Earth: an extension to the sandwichcase. Geophys. J. Int. 154 (1), 44–57.

Dziewonski, A. M., Lekic, V., Romanowicz, B. A., 2010. Mantle Anchor Structure: An argument for bottom up tectonics. Earth Plan. Sci. Lett. 299, 69–79.

Garnero, E., Revenaugh, J., Williams, Q., 1998. Ultra-low velocity zone at the core-mantle boundary. Geodynamics . . . 28, 319–334.

Garnero, E. J., McNamara, A. K., 2008. Structure and dynamics of Earth's lower mantle. Science 320 (5876), 626.

He, Y., Wen, L., 2009. Structural features and shear-velocity structure of the Pacific Anomaly. J. geophys. Res 114, B02309.

Ishii, M., Tromp, J., 1999. Normal-mode and free-air gravity constraints on lateral variations in velocity and density of Earth's mantle. Science 285 (5431), 1231–1236.

Ishii, M., Tromp, J., 2004. Constraining large-scale mantle heterogeneity using mantle and inner-core sensitive normal modes. Phys. Earth. Plan. Int. 146 (1-2), 113–124.

Karato, S., 1998. Some remarks on the origin of seismic anisotropy in the D" layer. Earth Planets and Space 50, 1019–1028.

Kendall, J., Silver, P., 1998. Investigating causes of D" anistropy. Geodynamics Series 28, 97–118.

Lay, T., Williams, Q., Garnero, E. J., 1998. The core-mantle boundary layer and deep Earth dynamics. Nature 392 (6675), 461–468.

Lekic, V., Cottaar, S., Dziewonski, A. M., Romanowicz, B., 2012. Cluster analysis of global lower mantle tomography: A new class of structure and implications for chemical heterogeneity. Earth Plan. Sci. Lett. 357-358, 68–77.

McNamara, A. K., Garnero, E. J., Rost, S., Oct. 2010. Tracking deep mantle reservoirs with ultra-low velocity zones. Earth Plan. Sci. Lett. 299 (1-2), 1–9.

Murakami, M., Hirose, K., Kawamura, K., Sata, N., Ohishi, Y., 2004. Post-perovskite phase transition in MgSiO3. Science 304 (5672), 855–858.

Ni, S., Tan, E., Gurnis, M., Helmberger, D., 2002. Sharp sides to the African superplume. Science 296 (5574), 1850–1853.

Oganov, A., Marton˜a'k, R., Laio, A., Raiteri, P., Parrinello, M., 2005. Anisotropy of Earth's D layer and stacking faults in the MgSiO3 post-perovskite phase. Nature 438 (7071), 1142–1144.

Pozzo, M., Davies, C., Gubbins, D., Alfè, D., 2012. Thermal and electrical conductivity of iron at Earth's core conditions. Nature 485 (7398), 355–358.

Ricard, Y., 2007. Physics of mantle convection. Treatise on Geophysics 7, 31–87.

Ritsema, J., Ni, S., Helmberger, D., Crotwell, H., 1998. Evidence for strong shear velocity reductions and velocity gradients in the lower mantle beneath Africa. Geophys. Res. Lett. 25 (23), 4245–4248.

Rost, S., Garnero, E. J., Stefan, W., Jun. 2010. Thin and intermittent ultralow-velocity zones. J. Geophys. Res. 115 (B6), 1–12.

Thorne, M. S., Garnero, E. J., 2004. Inferences on ultra-low velocity zone structure from a global analysis of SPdKS waves. J. Geophys. Res 109, B08301.

To, A., Romanowicz, B., Capdeville, Y., Takeuchi, N., 2005. 3D effects of sharp boundaries at the borders of the African and Pacific Superplumes: Observation and modeling. Earth Plan. Sci. Lett. 233 (1-2), 1447–1460.

Wen, L., Silver, P., James, D., Kuehnel, R., 2001. Seismic evidence for a thermo-chemical boundary at the base of the Earth's mantle. Earth Plan. Sci. Lett. 189 (3-4), 141–153.

Chapter 2

An unusually large ultra-low-velocity-zone on the core-mantle boundary near the Hawaiian hotspot

2.1 Introduction

The lowermost ∼200 km of the mantle are dominated by two large antipodal regions of low shear velocities, also called 'superplumes' or large low shear velocity provinces (LLSVPs). Both are centered close to the equator, one beneath Africa and the other one beneath the Pacific. LLSVPs are responsible for the strong and dominant "degree two" in global shear wave velocity models in the lowermost 1000 km of the mantle (e.g. Dziewonski et al., 2010). Local waveform studies indicate that the edges of the LLSVPs are sharp (e.g. Ni et al., 2002; To et al., 2005; Sun et al., 2009) and LLSVPs may be denser than their surroundings (Ishii and Tromp, 2004; Trampert et al., 2004), suggesting that they may be chemically distinct. In particular, it has been proposed that they might consist of primitive, non-pyrolitic material (Deschamps et al., 2011). The role of the LLSVPs in the global dynamics is still a question of debate. It is difficult to model stable super-domes (Davaille, 1999), as material tends to accumulate in more ridge-like features (McNamara and Zhong, 2004). Locations of denser material could be controlled by the forces exerted by the surrounding downwelling material (McNamara and Zhong, 2005; Tan et al., 2011; Steinberger and Torsvik, 2012), or, alternatively, the LLSVPs might represent long lived structures that control the surrounding mantle circulation (Dziewonski et al., 2010).

Local waveform studies, which have higher resolution than global tomography, have documented the occurrence of ultra low velocity zones (ULVZs) mostly near the borders of

LLSVPs. An overview map of the possible lateral extent of ULVZs based on estimates of data sensitivity kernels is given in the supplementary material of McNamara et al. (2010)). The corresponding shear wave velocity reductions are in the range of -10 to -30%. To date, the documented ULVZs heights are constrained at ∼5-30 kilometers, while little is known about the lateral extent (due to data coverage). The seismic phases used to detect these structures include reflected phases (PcP, e.g. Rost et al. (2010), ScP, e.g. Rost et al. (2005)), scattered core phases (SPdKS, e.g. Thorne and Garnero (2004), SKS, e.g. Rondenay and Fischer (2003), PKP, e.g. Luo et al. (2001), PKKP, e.g. Rost et al. (2006)) and diffracted phases (Sdiff, e.g. To et al. (2011)). ULVZs might also have a signature in normal mode splitting functions (Koelemeijer et al., 2012). At this point it is unclear if the variations in ULVZ geometries are due to the large uncertainties in lateral extent and trade-offs between dimension and velocity reduction in seismic studies, or if a range of ULVZs exists on the CMB. Geodynamic modeling (Bower et al., 2011) suggests a range of different ULVZs of different sizes and shapes as a function of density contrast and amount of dense material available. The cause of ULVZs is mainly thought to be iron enrichment (Wicks et al., 2010; Mao et al., 2006) and/or the presence of melt inclusions (Williams and Garnero, 1996; Hier-Majumder, 2008).

Here we present a dataset of transverse component S/Sdiff waveforms from three western Pacific events observed at stations in North America, that illuminate an unusually large ULVZ at the northern edge of the Pacific LLSVP, near Hawaii. Owing to the strong sensitivity of the data to the structure, we can forward model a simplified 3D ULVZ, and provide constraints on its geometry and strength including, for the first time, its lateral extent.

2.2 Data and observations

2.2.1 Event 1. March 20th 2010 event

The main event we considered (Event 1) is a deep earthquake (Mw 6.6; depth= 414 km) which occurred on March, 20th, 2010 in the New Ireland Region, Papua-New Guinea (Table 1). Piercing points 40 km above the CMB as predicted for a 1D model (PREM, (Dziewonski and Anderson, 1981)) are plotted in map view in Figure 2.1 for all S/Sdiff paths (gray circles). The USArray transportable array (http://www.iris.edu/earthscope/usarray) and numerous other broadband networks provide dense station coverage in North America. The background tomographic model shows how the paths sample the northern Pacific LLSVP boundary. The radiation pattern for SH is shown in Figure 4.5 for the take-off angle of the diffracting phase. The pattern is favorable with strong SH amplitudes in the azimuthal range covered by the data.

This data set contains strong waveform complexities. At azimuths larger than about 48°, the S/Sdiff phase is split into a weaker first arrival and a strongly delayed second phase, which we call 'postcursor I'. The postcursor has the same polarity as the main phase. The presence and move-out of postcursor I is mainly a function of azimuth, but the amplitude

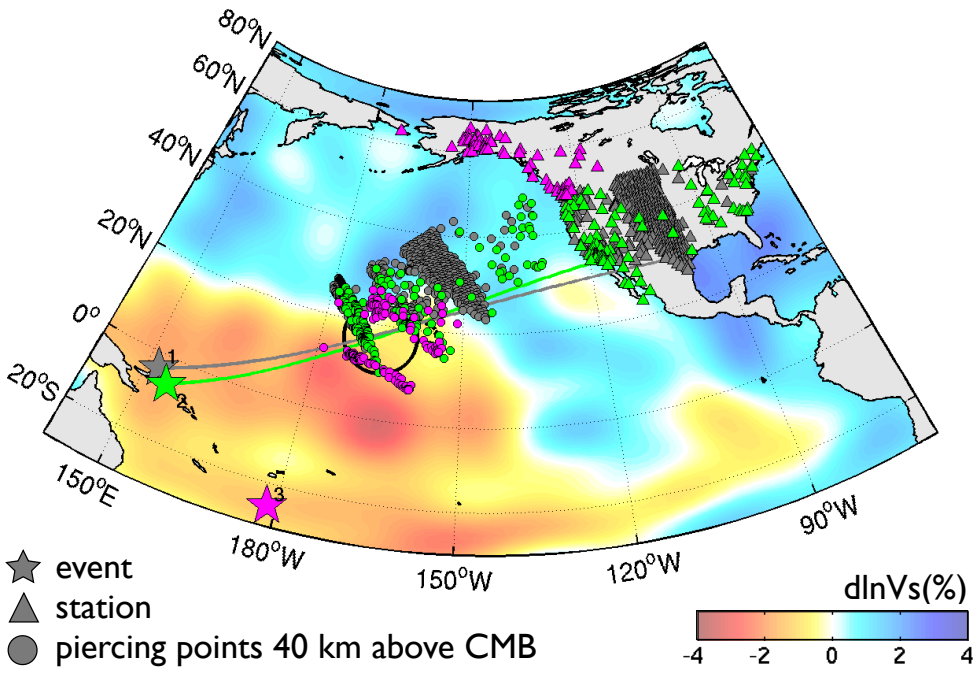

Figure 2.1: Coverage of the Event 1 (gray), Event 2 (green) and Event 3 (magenta) events across the northern boundary of the Pacific LLSVP. The circles represent the entry and exit points of the Sdiff phases approximately 40 km above the CMB. Background model is SAW24B16 (Mégnin and Romanowicz, 2000) at a depth of 2750 km ($\sim$ 150 km above the CMB). Black circle shows location of the proposed ULVZ.

ratio between postcursor I and the main phase becomes larger with increasing distance (Figure 4.6bc).

To process the data, the seismic instrument responses are deconvolved and horizontal components are rotated to radial and tangential. Tangential component S and Sdiff waveforms for Event 1, filtered with a bandpass butterworth filter between 10-20s (0.05-0.1Hz), are shown in Figure 4.6 for distance ranges of 88-94° (panel a), 94-100° (panel b) and 100-110° (panel c). The waveforms are shifted to align with the predicted S/Sdiff arrival time for PREM.

Additionally, we show the diffracted phases for Event 1 in different frequency bands, in Figure 2.4, to illustrate their frequency dependence. When comparing waveforms filtered between 10 and 30 s in the second panel with the first panel, filtered between 10 and 20 s, some differences become apparent. The large main phase arrival does not decay much with azimuth, indicating that the longer periods are less sensitive to the structure causing the waveform complexities. Additionally, an intermediate postcursor appears that is only minimally delayed around 46° but moves out towards postcursor I at the larger azimuths.

Name	Date	Lat	Lon	Depth	Mw	# of Traces
Event 1	March 20th 2010	-3.36	152.24	414.6	6.6	455
Event 2	June 12th 2003	-5.99	154.76	186.3	6.2	167
Event 3	February 21st 2011	-25.95	178.47	567.5	6.5	57

Table 2.1: Events used in this study. Number of traces represent usable traces after selection by eye.

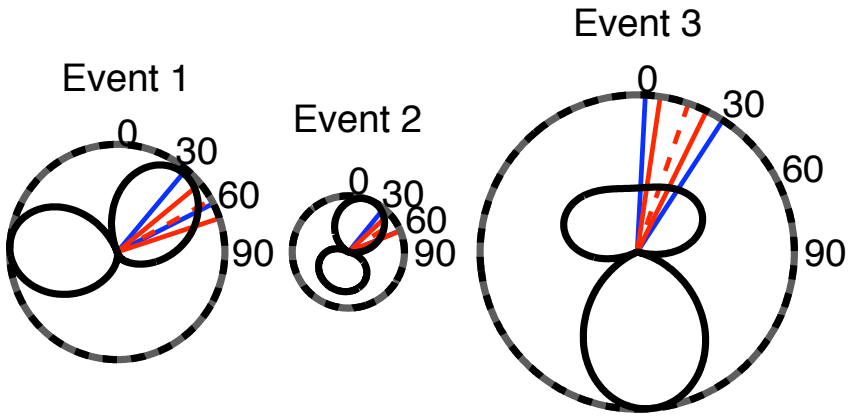

Figure 2.2: Radiation patterns of SH for all events for distances of 100°. Blue lines indicate the bounds of azimuths represented in the data coverage. Red azimuth bounds show those affected by the proposed ULVZ, with the red dashed line going through its center. Radiation patterns are scaled to moment magnitude.

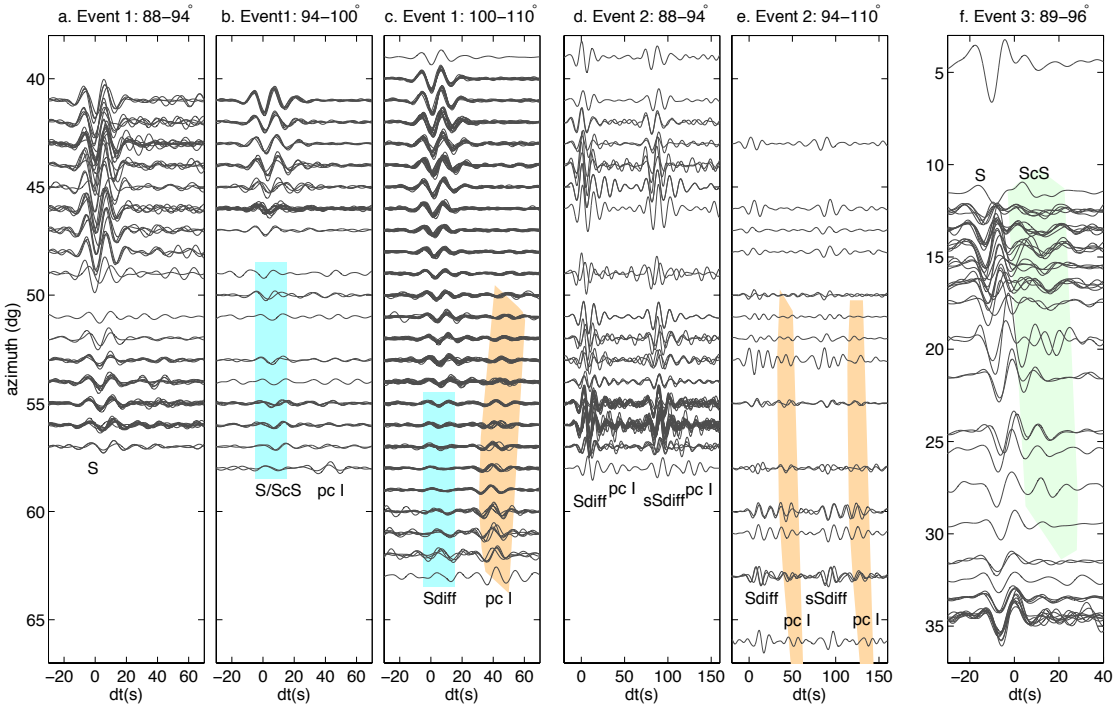

Figure 2.3: Tangential velocity waveforms for Event 1 at distances between 88-94° (a), 94-100°(b), and 100-110° (SHdiff, c), for Event 2 between 88-94° (d) and 94-110° (e) and for Event 3 between 89-96° (f). Traces are plotted in azimuth bins of one degree. Data are filtered between period of 10-20s (a-e) and 10-30s (f). All traces within one event are normalized by the same constant. Shaded bands indicate the strongest occurrences of postcursor I in Sdiff (orange) and in ScS data (green) and the strongest distortion of the main phase (blue) . Most modeling of this study is focused on fitting the 316 traces at the furthest distances of Event 1 (panel c).

We name this postcursor II. Postcursor II is Sdiff energy to the north of the ULVZ that becomes slightly refracted towards the south as part of its sensitivity kernel senses the low velocities of the ULVZ. As the sensitivity kernel broadens for longer periods, this postcursor mostly shows up in the broader period band. At periods longer than 30s (third panel), there are no obvious complexities, only a slight move-out and amplitude increase in the Sdiff towards the south. The longer wavelengths appear to be insensitive to whatever structure is causing the scattered phases, and their move-out and amplitude increase can be explained as solely due to the low shear velocities in the LLSVP. The frequency-dependent variations constrain the height of the ultra-slow structure, as shown below. The depth sensitivity variations with period of diffracted phases on the CMB is very similar to that of surface waves, and therefore this case can be compared to slow structures in the shallow crust (e.g. sedimentary basins). Also similar to surface waves is the limited lateral resolution due to the integrated sensitivity along the path of the Sdiff. For core diffracted phases this is even worse due to longer wavelengths at the CMB boundary for similar periods, and further complications arise from the source and receiver side legs through the mantle.

The Pdiff waveforms are shown in Figure 2.5, filtered between 10-20s. The move-out of the Pdiff phase with azimuth is a lot weaker than that of the Sdiff phase (Figure 2.8), consistent with P velocity variations being weaker than S in the D″ (Masters et al., 2000). At the higher azimuths ($> 55°$) the Pdiff travel times flatten out, while the Sdiff travel times increase strongly. This suggests the Pdiff phase is less affected by the slow structures than the Sdiff phase.

2.2.2 Event 2. June 12th 2003 event

A second event, which occurred 400 km to the southeast of Event 1, shows similar complexities. At that time, which was before the deployment of the USArray, the station coverage in North America was not as good. Event 2, however, did occur during the deployment of the NARS-baja array (Clayton et al., 2004), offering extended coverage towards the south. Waveforms on the tangential component are shown in Figure 4.6de filtered between 10 and 20s. This event is shallower, and thus the S(diff) and depth phases are only 80 seconds apart and are both shown. The sS(diff) phase has significant amplitude, while the pS(diff) cannot be distinguished. Similar postcursors as for Event 1 are visible, and also present an increased move-out in the delay of postcursor I towards the south. The reduction in amplitude of the main phase is not as apparent as in Event 1. This event has previously been studied by To et al. (2011) and we compare our results with theirs in the discussion section.

Similar complexities could in principle also be seen after the main Sdiff phase at similar azimuths for every other event we looked into. Waveforms for one other event (on September 4th 1997) are presented by To et al. (2011) along with Event 2. Coverage for this event is significantly less dense and its magnitude is smaller. Other, nearby, recent events (on 2010/08/04, 2010/08/15, 2010/12/13, 2011/02/07, 2011/12/14) since the deployment of USArray, show disappearance of the main arrival and delayed postcursor energies, but none

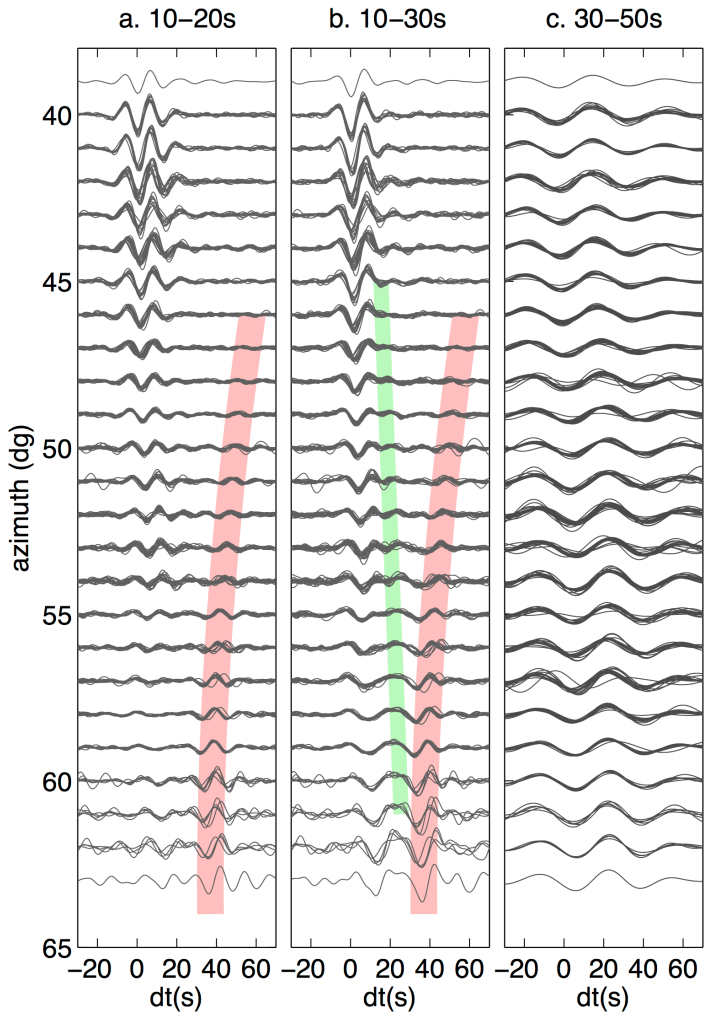

Figure 2.4: Tangential velocity waveforms for Event 1 at diffracted distances. Data are filtered between period of 10-20s (a), 10-30s (b) and 30-50s (c) to illustrate frequency dependence of the observations. All traces are normalized by the same constant and plotted in one degree azimuth bins. With increasing azimuth, waveforms broaden for the longer periods. Most striking in the longer periods is the decrease in amplitude of the main phase and the existence of a postcursor that moves out with decreasing azimuth. Pink and green bands indicate the occurrence of postcursor I and II, respectively. Each panel contains 316 traces.

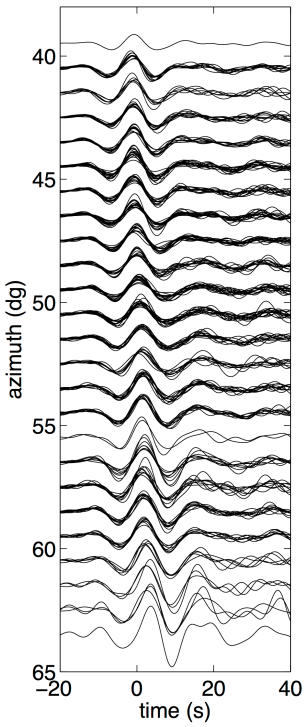

Figure 2.5: Vertical component velocity waveforms windowed around Pdiff arrivals for Event 1 as a function of azimuths.

are suitable for in-depth analysis. A number of events are too shallow (< 150 km), so that the postcursor and depth phases interfere, making it difficult to analyze them. Other events are too small, or have nodal planes in the azimuthal direction of interest. [1]

2.2.3 Event 3. February 21st 2011 event in Fiji

We also consider a recent deep (567 km) event in the Fiji Islands from which diffracted waves to Alaska and USArray illuminate the same D″ region but from a different angle (Figure 2.1, magenta). In the distance range available (89-96°), the ScS wave should arrive less than 3 s after the S phase, based on a 1D reference model. However, significant time delays in the 5-27° azimuth range (Figure 4.6f) indicate that it is affected by a localized very slow anomaly, not sensed by the S wave. Some of the traces exhibit strong scattering, with at least one apparent postcursor.

[1] During the final stages of this project, the most suitable event after Event 1 so far occurred on 2012/04/17 and confirms all the observations seen here.

2.3 Data analysis

2.3.1 Waveform clustering

Clustering of the waveforms provides an objective way to classify the strong variation in waveforms in a qualitative way (e.g. Houser et al., 2008; Adelfio et al., 2012). We choose a 60 s window around the predicted arrival time for SHdiff in the 1D reference model PREM (Dziewonski and Anderson, 1981). The measure of coherence is the correlation between the two waveforms (in other words, the distance metric used between two waveforms is one minus the correlation between the two waveforms). Clustering can be done in various ways. Here we preferred k-means clustering (Hartigan and Wong, 1979) over hierarchical clustering as it resulted in smaller distances within the clusters. For k-means the number of clusters needs to be fixed beforehand. Initially, random centroids are chosen for these clusters. Next, all the waveforms are assigned to these clusters, after which the centroid of the cluster is recomputed. These last two steps are iterated, until the solution is stabilized. As local minima might occur, the whole procedure is repeated 100 times with different initial starting points. Clustering for Event 1 is applied to the diffracted phases filtered between 8 and 100s for distances between 98 and 110° and results are shown at their exit points from the D″ in Figure 2.6. The boundaries of the clusters mostly depend on azimuth. There is a clear correlation between the three clusters, and the parts of the lowermost mantle sampled by the corresponding paths, as defined by global shear wave tomographic model SAW24B16 (Mégnin and Romanowicz, 2000): the most northerly cluster corresponds to paths sampling the fast side of the LLSVP; the most southerly cluster consists of paths sampling the slow side and shows scattering due to small-scale heterogeneities; and the middle cluster appears to correspond to the LLSVP boundary. A number of stations in the most northerly cluster, fall into the middle cluster. These stations lie above the Yellowstone plume, causing wave complexities due to near-receiver structure. From the clustering combined with the global model, we define the boundary of the LLSVP to lie around 50° in azimuth for Event 1. Clear and similar clusters separated by azimuth also result for S and sSdiff phases, while SKS and SKKS phases are more scattered and show more variation with distance.

Figure 2.7a shows the three clusters for Event 2 (June 6th 2003) . The boundary of the clusters and the waveforms in Figure 2.7b behave in a way similar to Event 1. The three clusters group in a similar manner.

2.3.2 Travel times

As cross-correlation measurements are unsuitable for the strongly distorted and attenuated Sdiff-phases at azimuths greater than 54°, we measure travel times by lining up the first peak of the waveform with synthetic 1D PREM reference waveforms. Travel times for the Sdiff main phase are presented in Figure 2.8 together with travel times for SKS and Pdiff. As the path enters the LLSVP, the delay in the Sdiff phase is gradual, lacking a sharp

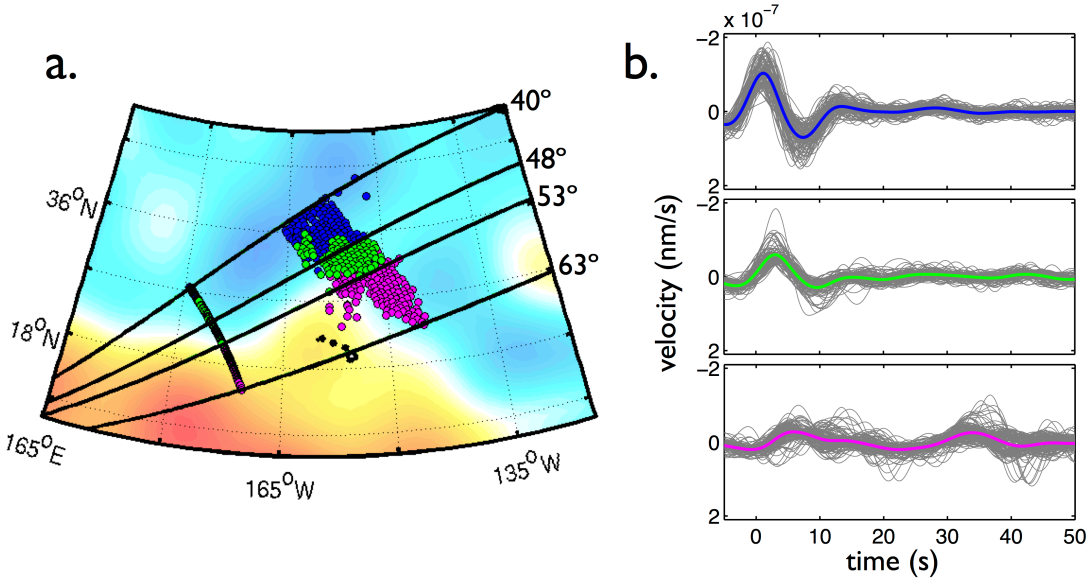

Figure 2.6: Waveform clustering for Event 1. a) Entry and exit points to the diffracted portion of SH are color coded according to the three distinctive waveform clusters. Background model is SAW24B16 on the same scale as Figure 1. b) Waveform stacks for the three clusters are ordered from north to south. Individual waveforms are plotted in the background to show variation in the waveforms within each cluster.

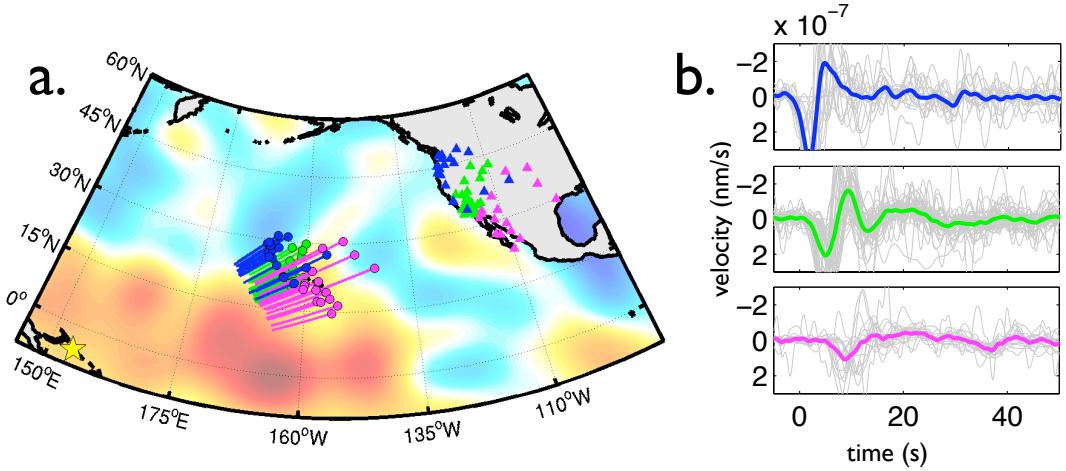

Figure 2.7: Waveform clustering for Event 2. a) Entry and exit points to the diffracted portion of SH are color coded according to the three distinctive waveform clusters. b) Waveform stacks for the three clusters are ordered from north to south. Individual waveforms are plotted in the background to show variation in the waveforms within each cluster.

transition as observed for the African plume boundary (Ni and Helmberger, 2003; To et al., 2005). Much of the scatter in the travel times is due to distance effects. The SKS phase shows a significant trend with azimuth, with a peak travel time around 54°. This trend is uncorrelated with the Sdiff phase, and we suspect it is caused by an anomalous high part of the LLSVP in the source side path of the SKS (He and Wen, 2009). This makes the SKS an unsuitable reference phase, but interesting in itself. The group of slightly more delayed phases around 45-46° correlates with the stations above the Yellowstone plume. As discussed in the main article, the trend with distance appears to correlate well with upper mantle structure, where the paths enter the craton (and are thus faster) at a distance of 104°. Only the SHdiff arrivals between 106 and 110° do not follow this trend with distance, as these arrive in Texas where the lithosphere is thinner (Yuan and Romanowicz, 2010). The move-out with distance is similar to that seen in SKS travel times, and seems to correlate with the upper mantle structure below the US: travel times for stations in the west are generally several seconds shorter than for stations above the craton in the central US. Even though the SKS phase shows the same trends in absolute travel times with distance, it cannot be used as a suitable reference phase, as it is in general delayed by more than 5 seconds with respect to the Sdiff phase. We explain this by the difference in paths of SKS and Sdiff on the source side, where the SKS phase samples a region where the Pacific LLSVP extends higher into the lower mantle (He and Wen, 2009). We avoid biases from this structure by not using SKS as a reference phase.

The travel times for postcursor I are measured manually with respect to the Sdiff waveforms in PREM synthetics. This synthetic reference phase does not match the postcursor waveforms closely at all stations, so we preferentially line up the first peak. Results are also shown in Figure 2.9a next to travel time measurements for the main Sdiff phase. For Event 1, the minimum delay for postcursor I is around $\sim 60°$ in azimuth and delays increase towards smaller azimuths. There is some indication that they also increase towards larger azimuths. Fitting the travel times with a degree 4 polynomial results in a best fitting minimum travel time delay of ~ 30 seconds with respect to Sdiff, at an azimuth of $\sim 60°$ (shown by the gray line in Figure 2.1).

For Event 2, which occurred to the southeast of Event 1, shifting observations in the US to smaller azimuths (e.g. Figure 2.1), the NARS-Baja California stations (Clayton et al., 2004) provide complementary coverage at larger azimuths, showing increasing delays towards the south. Here the minimum travel time delay of postcursor I with respect to Sdiff is $\sim$32 s at an azimuth of $\sim$57° (Figure 2.9b).

For Event 3, the ScS phase is delayed with respect to S (Figure 3c). Both phases show the same trend of arriving faster between 12 and 20° azimuth. This must be due to an upper mantle effect, as the same trend is seen in other phases including SKS. In general, these observations show many other delayed scatterers that are small in amplitude.

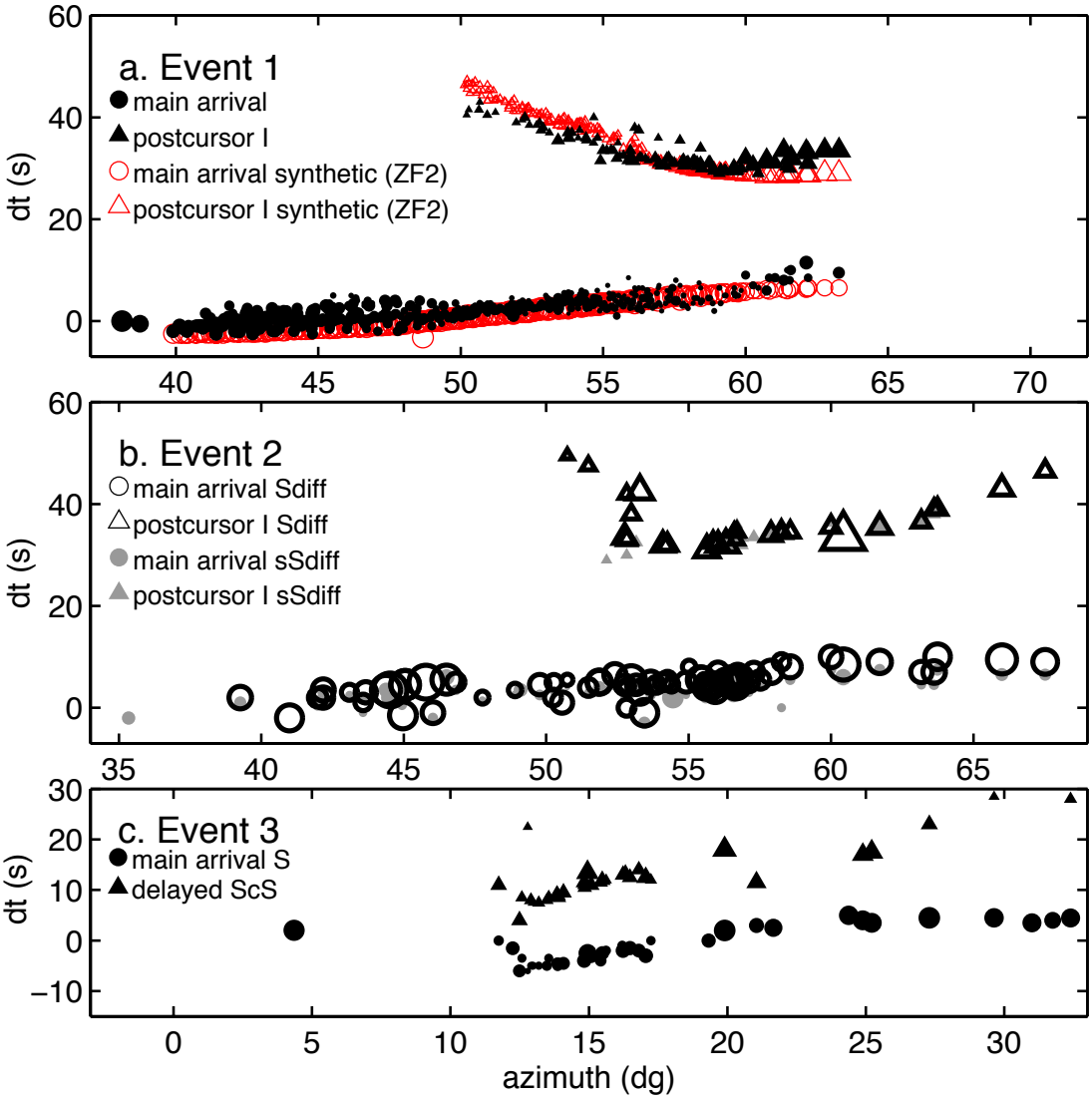

Figure 2.8: Travel time measurements for Sdiff (black), Pdiff (green) and SKS (red) as a function of azimuth (a) and as a function of distance (b)

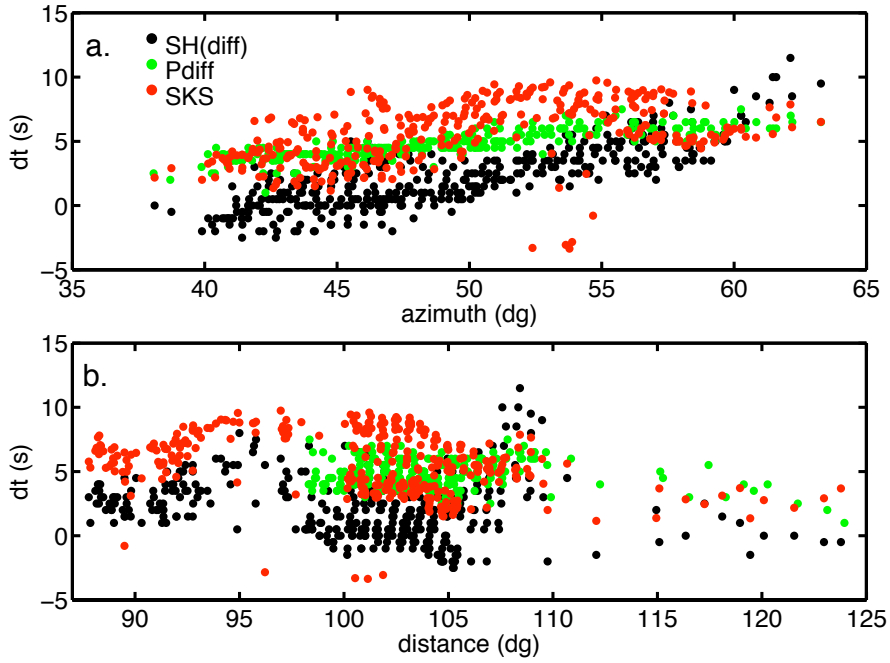

Figure 2.9: Differential travel times between data and PREM synthetics measured in the 10-20s band for main phase (circles) and postcursor (triangles). Panel a. is observed and synthetics (ZF2) for Event 1, panel b. for Event 2 and panel c. for Event 3 (note the azimuth range is very different for this last event). For Event 2 open symbols are for Sdiff, closed (gray) symbols for sSdiff. Symbol size indicates relative amplitude normalized by the amplitude of the PREM synthetic Sdiff phase.

2.3.3 Beamforming

The beamforming array technique (To and Capdeville, 2011) assumes the energy comes in as a plane wave. The Sdiff phase has the advantage of having a single horizontal slowness across the entire array. The results are insensitive to the precise choice of the reference slowness, but we use 8.5 s/deg . For each station we find the closest 20 stations. Then travel times are calculated between each station and the reference station for plane waves over a range of backazimuths. The Sdiff phase is windowed, filtered between 10-20s, and then stacked with the suitable travel time shifts for each of these stations. If the phases line up coherently for a specific backazimuth, the stacked waveform will be enhanced; otherwise the phases from different stations will destructively interfere. We find the backazimuth for which the stack has the largest amplitude.

The back azimuth of the main phase is on average shifted from the great circle path by 2-3° towards more northerly directions (Figure 2.10a). The shift is not due to a bias in the method, as synthetics for PREM (Dziewonski and Anderson, 1981) give the exact great circle backazimuths. It can be explained by 3D background velocity variations in the lowermost mantle, as shown by applying the same method on synthetics calculated in the model SAW24B16 (Mégnin and Romanowicz, 2000) in D″, which shows a similar shift. Presumably the northern boundary of the Pacific LLSVP is causing waves to refract by several degrees towards the south. A southerly shift at the LLSVP boundary will be viewed at the station as energy arriving more from the north. At the larger azimuths, where the main phase is reduced in amplitude, there is a larger scatter in the backazimuth measurement. Energy mainly comes further from the north.

The backazimuth of the postcursor can only be measured for azimuths larger than 50° where the amplitude of the postcursor is sufficiently large. Above this azimuth, we have measurements for every station in the distance range of 100-110°. The backazimuth deviation is around zero at an azimuth of 59-60° and this corresponds approximately to the azimuths where the delays of the postcursor are minimal. At larger azimuths, the backazimuth becomes more northerly, while it is progressively more southerly at smaller azimuths. In the center of the array, around azimuths of 50-54°, the backazimuth measurements return to zero, although we find the beamforming results to be very uncertain for these smaller amplitude postcursors.

2.3.4 Cause of postcursor: Initial modeling

Previous studies have interpreted postcursors in Sdiff phases as due to multipathing on the edge of one of the LLSVPs (To et al., 2005; Sun et al., 2009). In those studies, postcursors are less delayed and visible in a wide period band, as LLSVP boundaries extend to several hundreds of kilometers above the CMB. To produce postcursor delays of up to 47s and to limit postcursor occurrence to periods shorter than 30s, a causative structure with a stronger velocity reduction and smaller height is required, resembling previously modeled

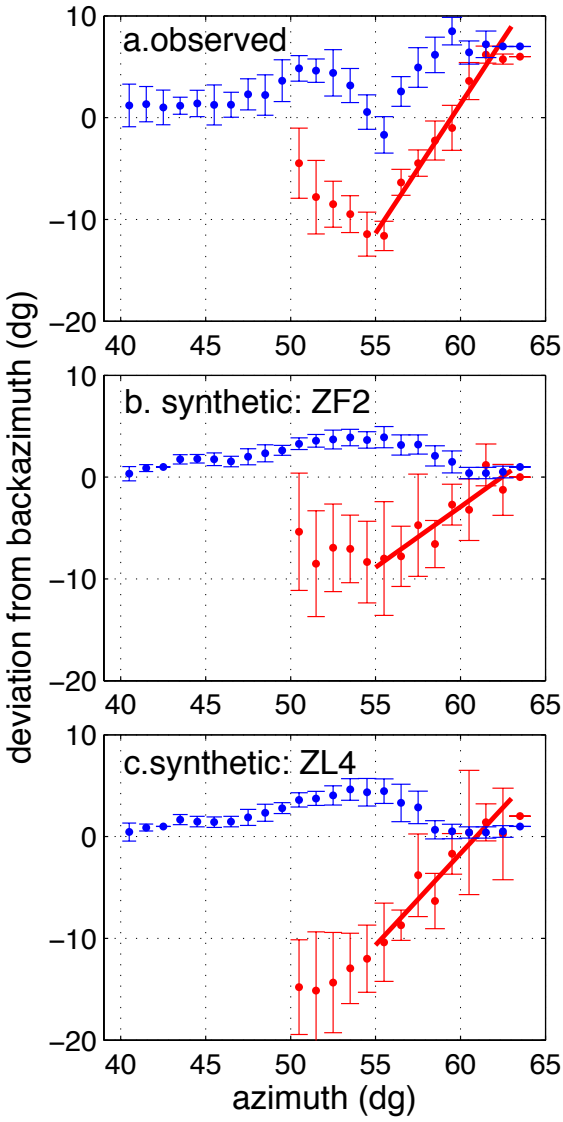

Figure 2.10: Beamforming results for Event 1 in observed data (a) and synthetic data for models ZF2(b) and ZL4(c). Backazimuths of the arriving energy of the main phase (blue) and postcursor (red). Mean and standard deviation of the backazimuth referenced to the great circle backazimuth for stations in each azimuth bin. Error bars indicate scatter within each bin. Positive means the phase comes from further to the north. Results for the postcursors at azimuths less than 50° aren't shown as they have very low amplitudes (and highly scattered results).

ULVZs.

By first considering the effects of the structure in the framework of ray theory, we show that, to first order, we can assume a circular base for this structure. In this case, we expect seismic waves to travel through the structure and be refracteded by its boundaries according to Snell's law (as illustrated in Figure 2.11). Travel time predictions for a perfectly circular low velocity structure predict maximum travel time delay for the ray that travels along the diameter of the ULVZ (fully transmitted, with no refraction). This phase will travel along its great circle path. However, compared to the reference main phase at the stations, this postcursor arrival has a minimal delay time, as other rays that are refracted by the ULVZ have shorter paths within the ULVZ, but are more delayed with respect to the reference Sdiff due to their longer, out-of-plane paths. For an elliptically shaped ULVZ (rotated from the great circle path), the minimum travel time path is offset from the great circle path arrival, and the travel time move-out is asymmetric at both ends. Here it seems that a structure with a close-to-circular shape explains the travel time observations. The main indication of this comes from the fact that the minimally delayed postcursors of Event 1 arrive along the great circle path (Figures 2.9 and 2.10). Furthermore, the minimal delay times of Events 1 and 2 lie within 10% of each other. On the other hand, there is some indication of slight asymmetry in the postcursor travel times on both sides of the minimum, especially in Event 2, so that the actual shape may be more elongated. However, the present data do not allow us to constrain the shape of the anomaly more precisely. Assuming a simplified 3D model also constrains the parameter space in which to search and illustrate trade-offs.

2.3.5 Forward modeling with CSEM

In order to interpret the full waveforms of the main phase and postcursors, we turn to an accurate but computationally heavy 3D numerical wave propagation method, the "sandwiched" version of CSEM (Coupled Spectral Element Method, Capdeville et al. (2002, 2003)). Compared to other SEM codes (e.g. SPECFEM3D, Komatitsch and Tromp (2002a,b); Tromp et al. (2008)) this method is computationally effective for the study of the D$''$ as it only solves for the full 3D spectral element solution in a layer of limited thickness (here 370 km) above the CMB. The spectral element method is especially useful to handle models with sharp, strong gradients in velocity as is the case here. When we model a specific ULVZ structure, we define the height of the structure as one element. This allows for a second order discontinuity at the top boundary, however the velocity jump will be smoothed over several kilometers to the first Gauss-Lobatto-Legendre integration point above. Maximum lateral smoothing at the boundaries of the structure is about 65 kilometers. However, any smoothing in the implementation of the model is negligible compared to the natural smoothing due to the wavelengths of the phases considered, which is on the order of 100 to 200 km. Not used here are the capabilities of the code for fully anisotropic models, as we only consider isotropic models. We consider SAW24B16 (Mégnin and Romanowicz, 2000) as the background model in the SEM region for SH and SV. P velocity variations are scaled to the 1/3, and no density variations are implemented. Since SAW24B16 is a pure

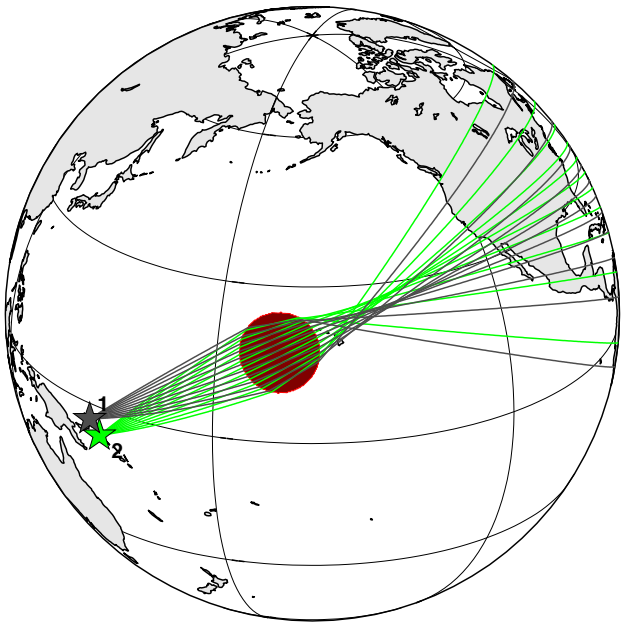

Figure 2.11: Predicted behavior of infinite frequency rays as they become scattered by a ULVZ near Hawaii. Velocity reduction in the ULVZ is 20%. The focal point of the lens-like structure lies just beyond the structure.

SH velocity model it agrees best with our SH observations modeled here. We did not test the possible effects of anisotropy in the D″ or upper mantle, but we expect the travel-time deviations of these complexities to be on the order of seconds. The only modifications made are that (1) the velocity model at 2800 km depth is extended down to the CMB and (2) in the top 70 km of the SEM region, SAW is smoothed towards PREM with a cosine taper. Additionally the background velocity is reduced by 0.5% to best match the observations. On 16 processors, 40 minutes of synthetic data down to 10 seconds presently requires 25 hours of computation time.

2.4 Results from forward modeling

2.4.1 Proposed preferred ULVZ

Our favorite model consists of a cylindrical ULVZ centered at 167.5°W and 17.5°N. It has a radius of 455 km, height of 20 km and velocity reduction of 20%. Therefore the width:height ratio is around 45:1. The synthetic waveforms for all three events are shown in Figure 2.12. As a quantitative illustration, mean waveform correlation between synthetics and observed traces for diffracted phases of Event 1 is 0.07 for PREM, 0.43 for modified SAW24B16 (NZ) and it improves to 0.64 for our 3D ULVZ model (ZF2). The preferred model reproduces postcursor I with a similar move-out and slightly stronger amplitudes, especially at the lower distances. The model reproduces an amplitude reduction for Event 1 at the largest azimuths. This amplitude reduction extends to smaller azimuths in the observations. Results for a broader period range for Event 1 are shown in Figure 2.13.

In the next sections we will show several tests that indicate the uncertainty in the parameters and some of the trade-offs between them. In the end we include Event 3 for additional azimuthal coverage. As our tests will illustrate, we are looking at rough uncertainties on the order of degrees in lateral location, ± 5 km in height, ±100km in lateral extension and several % in velocity reduction.

2.4.2 Trade-offs

2.4.2.1 Height

In the first test we investigate the influence of the height of the ULVZ by forward modeling with CSEM. The height is best constrained by the frequency dependence in the amplitudes of the observed main phase and postcursor I. We run tests for heights of 15, 25, 35 and 45 km for a model with 440 km radius, -20% shear velocity change and centered at 165°W and 19°N (models ZH1-ZH4, see Table 2.2). Figure 2.14 shows waveforms for USArray station 933A at an azimuth of 62° and a distance of 108° for models with different height. All traces in Figure 2.14 are normalized by the same value. Two different period

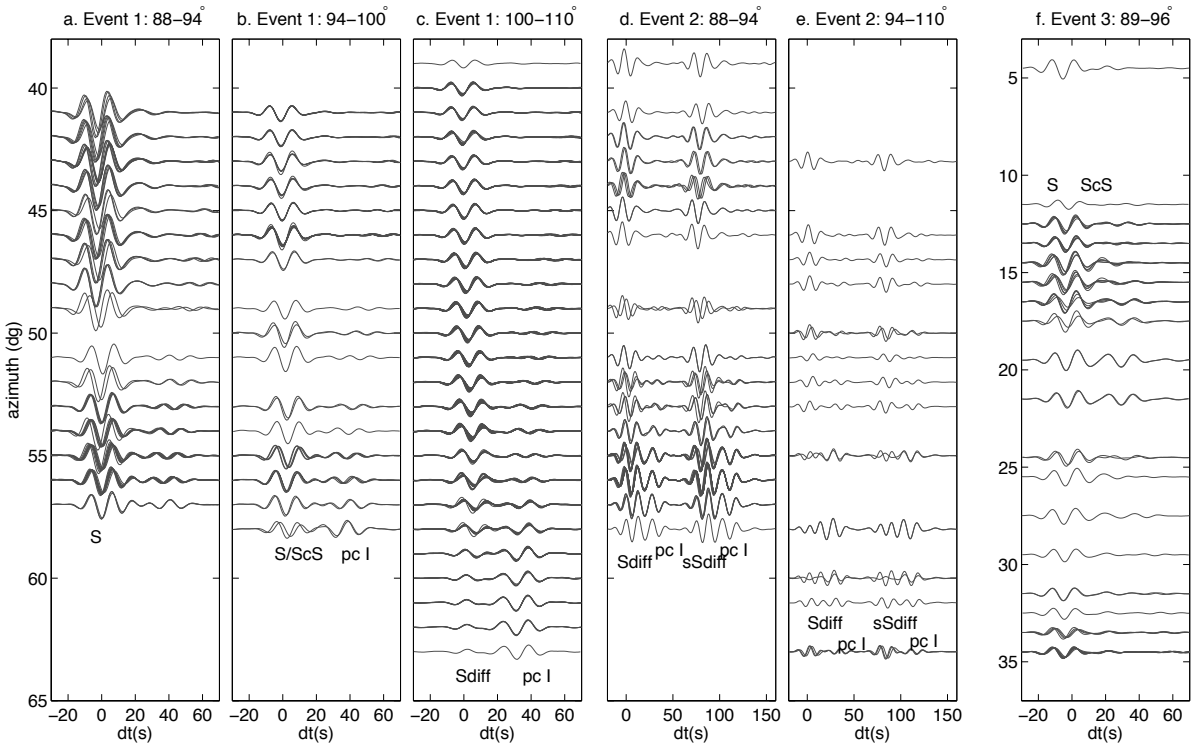

Figure 2.12: Synthetic tangential waveforms for Event 1 at distances between 88-94° (a), 94-100°(b), and 100-110° (c), for Event 2 between 88-94° (d) and 94-110° (e) and for Event 3 between 89-96° (f). Panels can be directly compared with observed data in Figure 4.6.

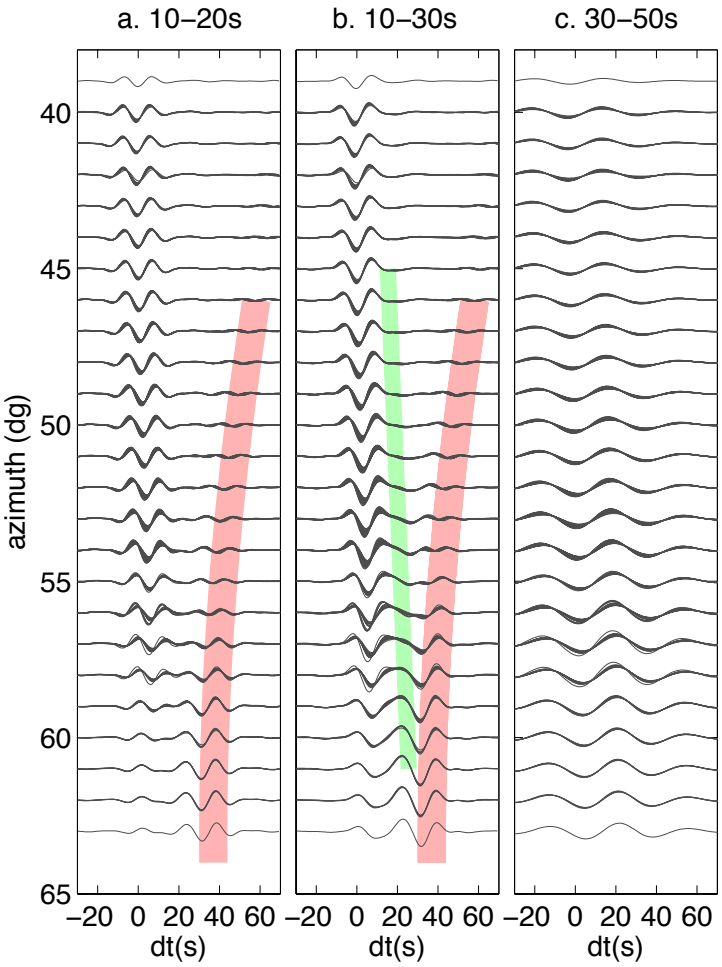

Figure 2.13: Synthetic tangential velocities for preferred ULVZ model (ZF2). Traces for March 20th 2010 between 10-20s (a), 10-30s (b) and 30-50s (c). Panels and normalization are identical to Figure 2.4 for comparison. Pink and green bands denote postcursor I and postcursor II respectively.

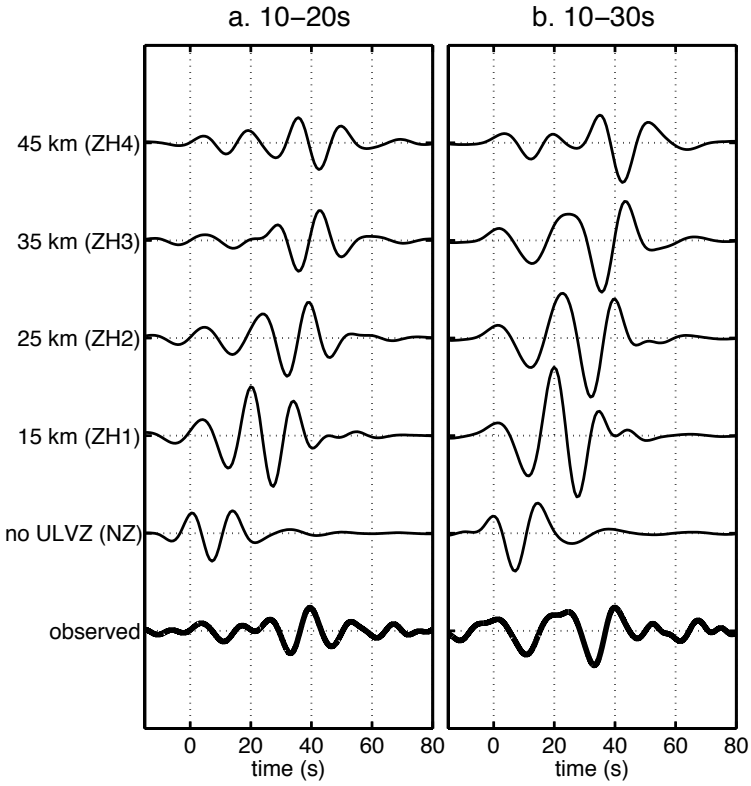

Figure 2.14: Real and synthetic waveforms for station 933A of the Transportable Array at an azimuth of 62° and 108° for two different frequency bands (a.10-20s, b.20-30s). All traces are normalized by the same constant. Synthetic models (ZH1-ZH4) include a cylindrical ULVZ with a 440 km radius, 20% velocity reduction, and centered at 165°W and 19°N.

bands, 10-20s and 10-30s, are shown. Both the amplitude of the main phase and the move-out and shape of the postcursor are sensitive to the height of the ULVZ. In order to fit the observations, the amplitude of the main phase needs to be more reduced in the 10-20s period band than in the 10-30s period band. In the 10 to 20 s band, the amplitude of the main phase becomes smaller relative to the postcursor for the thicker models. The move-out of the postcursor increases with thickness, implying trade-off between thickness and velocity reduction. There is a similar move-out of the postcursor with thickness in the 10-30s period band. In this period band, the amplitude of the main phase also decreases with thickness, but for thinner models, it is less affected than at shorter periods. In both period bands, the amplitudes and move-out agree best with a $\sim$ 25 km thick model.

In order to get a sense of lateral variations of the height, we find the minimum RMS error at each station between the observed waveforms and the SEM synthetics for various heights. Postcursors at most azimuths come from a different direction than the main phase, so both phases sample different parts of the ULVZ. We therefore apply this procedure

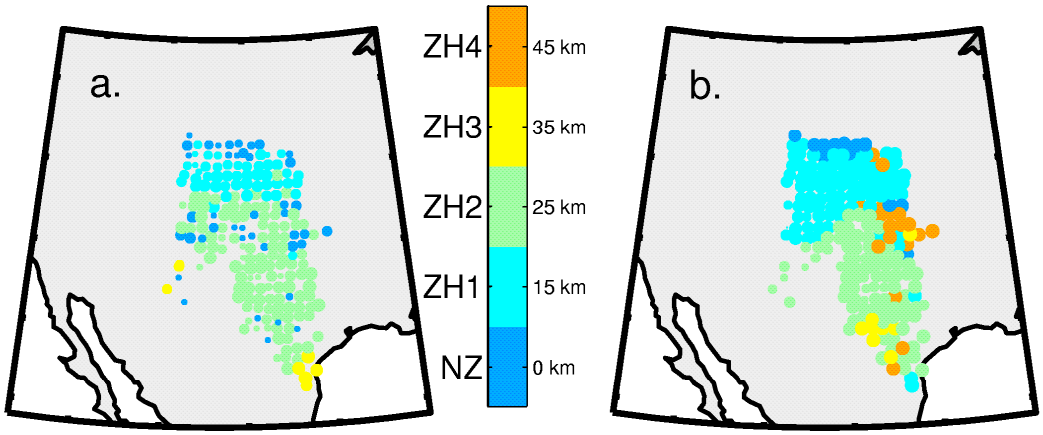

Figure 2.15: a. Station locations are color-coded by the best fitting height of the synthetic ULVZ model for postcursor I after windowing as indicated by the green shaded area in Figure 7a. Smaller azimuths are not shown and there is no significant energy in the postcursor window. b. Best fitting heights for the main phase in the 10-20s and 10-30s band and windowed as shaded blue in Figure 7. Smaller azimuths are ignored as differences between synthetics here are minimal.

separately to the main phase and postcursor I by windowing. The resulting best fitting heights are plotted on a map in Figure 2.15. For the postcursor, we find the best fits in the 10-20s period band, as the main phase and postcursor are best separated at these shorter periods. For the main energy, we fit both the 10-20s and 10-30s period bands, to take full advantage of the difference in amplitude between these two frequency bands. Overall the 25 km model fits best, although there is some scatter that is difficult to interpret. Some of the scatter might be due to irregularities in the shape of the ULVZ, while other discrepancies might result from unmodeled attenuation and near-receiver effects. The move-out of the postcursor entails trade-offs with the lateral extent and velocity reduction of the model. The same test with a slightly stronger model (410 km radius and 25% velocity reduction) results in more stations preferring a 15 km thick model.

We can roughly compare the case of diffracted phases in a ULVZ on the CMB to surface waves sensing a low-velocity basin in the crust. The rule of thumb for the period band (T) of and SH wave sensitive to slow shallow structure with a specific height (h) is given by $T = 4h/\beta$, where β is the shear velocity (Haskell, 1960). Applying this rule of thumb here, we note that the period band around 20s is most affected by the ULVZ. At 20s, a height of 27 km is predicted, very similar to what we find here by forward modeling.

2.4.2.2 Extent and velocity reduction of the ULVZ

Even within our simplified cylindrical model, a huge computational effort is required to grid search the range of possible sizes and velocity reductions or to apply a non-linear inversion algorithm. Here we gain our first estimate on these parameters from ray-theoretical predictions to reduce the search space. The estimated travel time delay for the path along the diameter of the ULVZ is given by $\frac{2r}{v}(\frac{1}{1-dv/v}-1)$, where r is the radius of the structure at the CMB, dv the velocity reduction, and v is the reference velocity inside the LLSVP. This delay time corresponds to the minimally delayed postcursor that travels along the great circle arc. The band between gray lines in Figure 2.16a contours the minimal delay times between 30s (minimal postcursor delay for Event 1, section 2.3.2) and 32s (for Event 2), illustrating the trade-off between the two parameters.

Next, we implement several models in CSEM and forward model waveforms for Event 1. Models ZS1-ZS4 are located at 165°W and 19°N and are 25 km in height (Table 2.2). The size and velocity reduction of these models are color-coded and plotted in Figure 2.16a and the resulting travel time delays for postcursor I (scaled by amplitude) are shown in the following panel (Figure 2.16b). The minimal delay times for the models in the gray band do not quite agree with the expected minimal delay times as predicted by ray theory. This is not surprising, as the finite-frequency sensitivity kernel of the wave is also sensitive to faster velocities above the ULVZ. In the previous section we also saw that increasing the height of the ULVZ, increases the sensitivity of the phase and thus increases the delay of the postcursor. For the largest model (ZS3) we see the postcursors merge towards the main phase. The strongest postcursor in this case is the intermediate postcursor, postcursor II (Figure 2.4. Waveforms for models ZS1-ZS3 are shown in Figure 2.17. As the model size increases we see an increasing amplitude of the postcursor. And for the largest model, the waveforms make very clear that postcursor II becomes stronger than postcursor I. ZS4 and ZS5 are models that fall above and below the line in Figure 2.16a, to illustrate the expected effect on the delay times.

Overall, to fit our observations (with this height), the model needs to be slightly above the gray band, while amplitudes of the postcursor are best fit for a radius around 400km (± 100km) at the CMB. To fit just Event 1 we could settle for a model with a radius of 455 km and a velocity reduction of 20%.

2.4.2.3 Location of the ULVZ

We investigate the possible locations by predicting ray-theoretically where the postcursor with minimum delay should arrive. When assuming a circular-base, the minimally delayed postcursor travels (non-refracted) through the center of the ULVZ along the great circle path.

Event 1 has a minimal travel time around 60° azimuth while Event 2 has a minimal

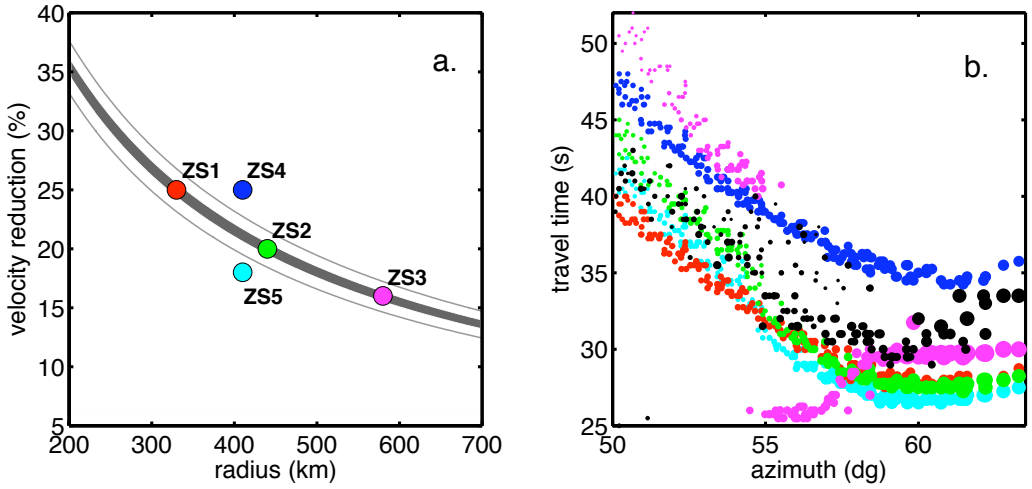

Figure 2.16: a. Trade-off between size and velocity reduction shown by the gray band, which represents ray-theoretical prediction times between 30 and 32 seconds. Colored dots show models implemented in CSEM. b. Travel times for models implemented in CSEM as a function of azimuth (color coordinates with panel a). Size of the markers indicates amplitudes. Observed travel times and amplitudes are shown in black.

travel time around 57° azimuth (section 2.3.2). We grid search over the area around the diffracted paths allowing for some uncertainty in these azimuth values. Figure 2.18 shows the bands of possible ULVZ centers for a two degree uncertainty (dark green) and a one degree uncertainty (green). The spread in possible locations is strongly anisotropic, being poorly constrained along the direction of propagation, and well constrained perpendicular to this direction. Next we model several models within this area. All models, ZL1-ZL5 have the same size (455 km in radius), velocity reduction (20%) and height (25 km). The circular bases for five locations are colored in Figure 2.18. Waveforms of these models for Event 1 are plotted in Figure 2.19for those traces where the postcursor is strong (azimuth$>$ 50°, 100° $<$dist$<$ 110°). As the model shifts further to the west, part of it lies outside of the diffracted path, and postcursor I becomes weaker. ZL3-ZL5, which are further to the east, correlate better with the observed data. It is difficult to distinguish between these three models on the basis of just one event.

Additional constraints come from Event 3. Even though Event 1 prefers a model more to the east, it strongly favors a ULVZ model located further to the west as this is where the phases are most strongly scattered. From the coverage of Event 3 (magenta in Figure 2.18), it already becomes clear that most of the traces of Event 3 will hardly be affected by the easternmost models. Synthetic waveforms for this event are computed with a ULVZ centered at (165°W , 19°N) and (170°W , 16.5°N) respectively ZL2 and ZL3, and one model (ZF1) in between at (167.5°W , 17.5°N). Waveforms are compared to the observations in Figure 2.20. The location further to the west better predicts the strongest scattering of the waveforms around azimuths of 12 to 20°. The intermediate model, ZF1, fits best without

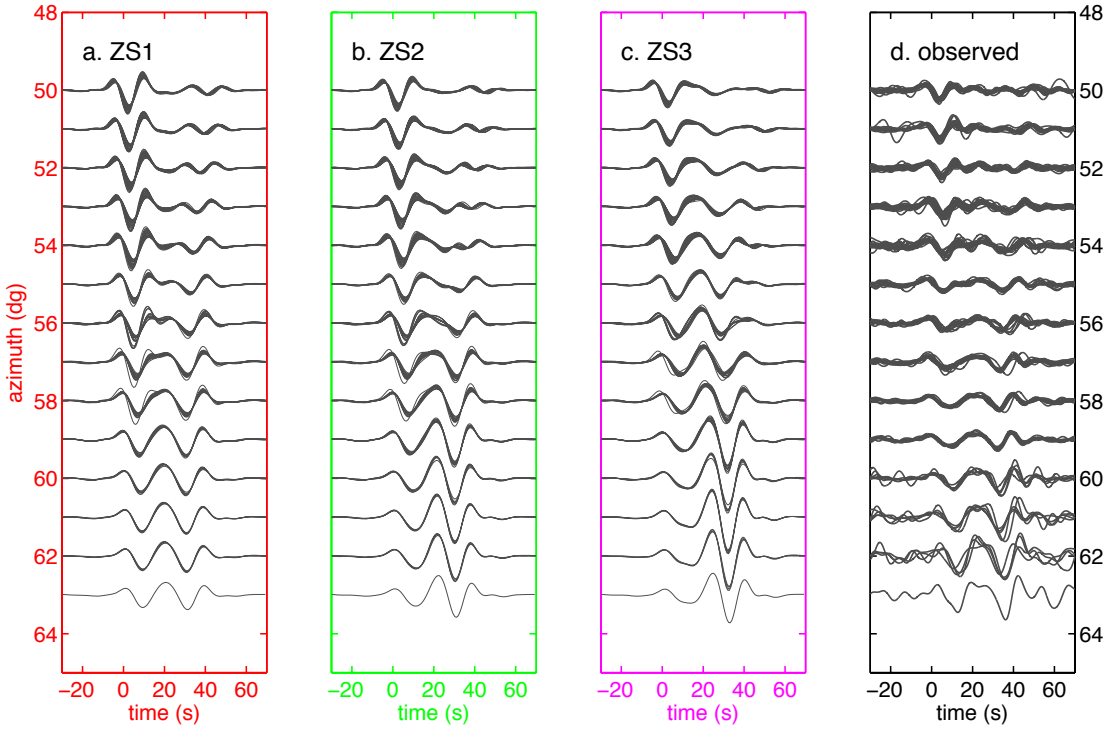

Figure 2.17: Synthetic waveforms in panels a-c are color-coordinated with Figure 8. Only the traces with strong postcursors in the 100-110° distance range, above an azimuth of 50° and filtered between 10 and 20 seconds, are shown. Panel d. shows the observations for comparison. From left to right, the ULVZ model broadens and weakens, resulting in more lateral energy entering the ULVZ and thus more energy in the postcursor. Also, from left to right we see the amplitude of postcursor II increasing. For the largest model, with a radius of 580 km (ZS3), the total delayed energy is strong, but postcursor II is stronger than postcursor I. A number of the measured travel times around 55-59° in Figure 8b are actually for the intermediate postcursor II.

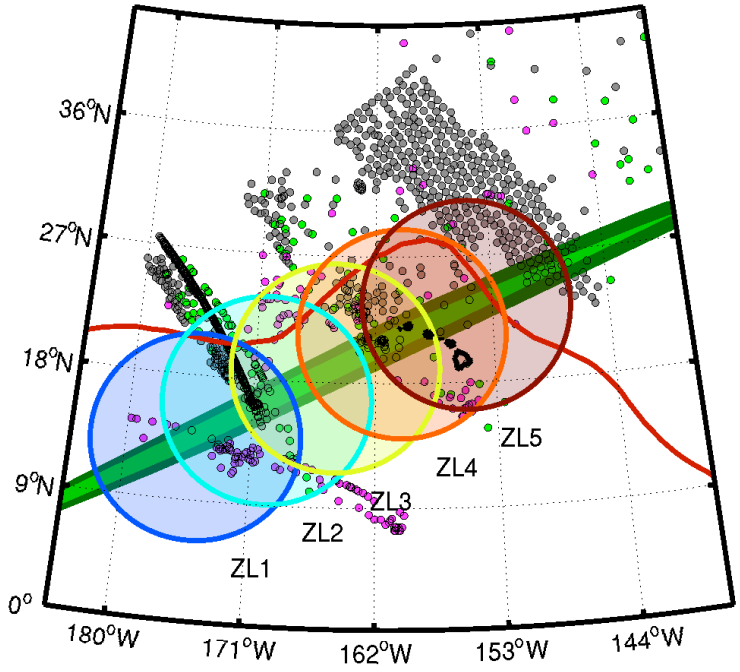

Figure 2.18: Grid search results for the center of a circular ULVZ that fit the minimal delay times of postcursor I in the ray-theoretical limit. Best locations are in the green band, while other reasonable locations are in dark green. Colored dots show coverage of Event 1 (gray), Event 2 (green) and Event 3 (magenta). Circular bases of the tested models ZL1-ZL5 are plotted and color-coded. Red line indicates LLSVP boundary in SAW24b16 at a depth of 2750 km.

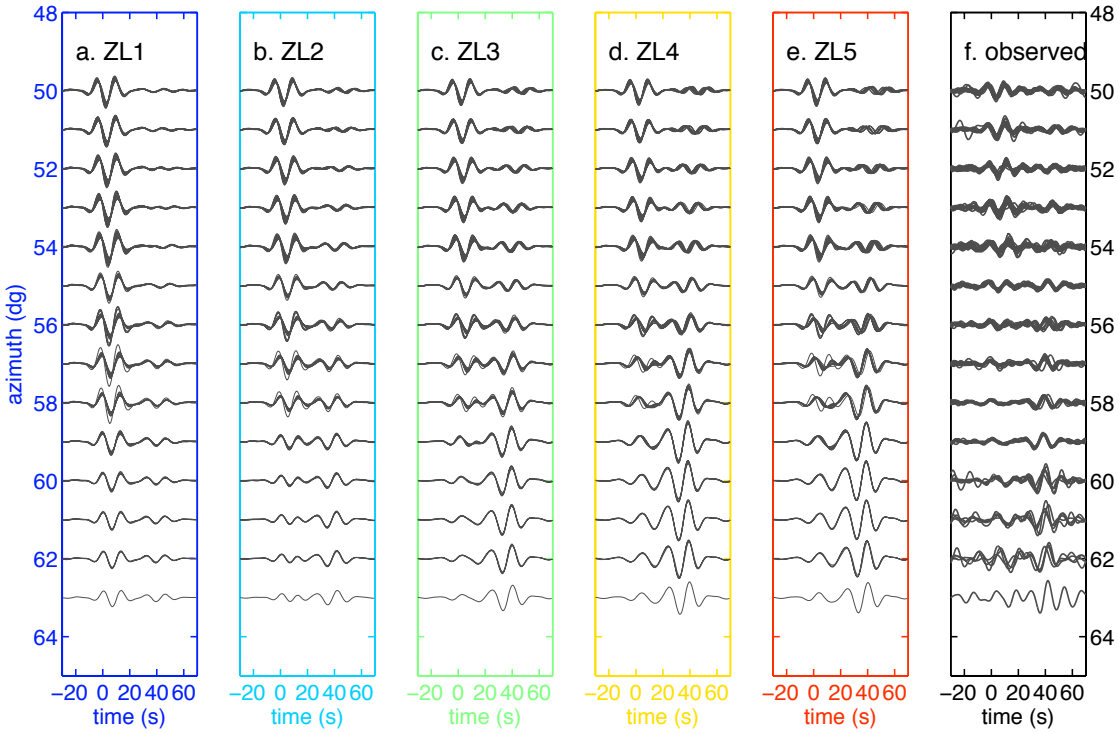

Figure 2.19: Synthetic velocity waveforms are shown in panels a-e correspond to the circular bases in Figure 9 from west to east (as color-coded). Only traces for azimuths above 50° and distances between 100 and 110° are shown. The waveforms are filtered between 10 and 20s. The last panel (f) shows the observed data for comparison. From left to right, or geographically from west to east, more of the ULVZ lies within the diffracted path and amplitude or the postcursor increases. Additionally there is some variation in amplitude of the main phase between the different models. Our final model sits between ZL2 and ZL3.

Model	Center lon	Center lat	Radius	Height	Vel. Red.	Corr.	Section
NZ	background model: modified SAW24B16					0.42	2.4.2.1
ZH1	165W	19 N	440 km	15 km	20%	0.38	Height 2.4.2.1
ZH2, ZS2	165W	19 N	440 km	25 km	20%	0.69	Height 2.4.2.1 Size 2.4.2.2
ZH3	165 W	19 N	440 km	35 km	20%	0.34	Height 2.4.2.1
ZH4	165 W	19 N	440 km	45 km	20%	0.09	Height 2.4.2.1
ZS1	165 W	19 N	330 km	25 km	25%	0.62	Size 2.4.2.2
ZS3	165 W	19 N	580 km	25 km	16%	0.41	Size 2.4.2.2
ZS4	165 W	19 N	410 km	25 km	25%	0.26	Size 2.4.2.2
ZS5	165 W	19 N	410 km	25 km	18%	0.51	Size 2.4.2.2
ZL1	175 W	13.5 N	455 km	25 km	20%	0.34	Location 2.4.2.3
ZL2	170 W	16.5 N	455 km	25 km	20%	0.47	Location 2.4.2.3
ZL3	165 W	19 N	455 km	25 km	20%	0.67	Location 2.4.2.3
ZL4	160 W	21.5 N	455 km	25 km	20%	0.69	Location 2.4.2.3
ZL5	155 W	23.5 N	455 km	25 km	20%	0.67	Location 2.4.2.3
ZF1	167.5 W	17.5 N	455 km	25 km	20 %	0.64	Event 3
ZF2	167.5 W	17.5 N	455 km	20 km	20 %	0.64	Event 3 l

Table 2.2: Selected CSEM models. Correlation shows mean correlation between synthetics and observed diffracted phases of Event 1 in the 10-20s bands.

strongly reducing the fit to Event 1. The finalized location at 167.5°W and 17.5°N is centered about 11° to the southwest of Hawaii. To improve travel time and amplitude fits of Event 3, the model is also reduced to 20 km in height (ZF2), without reducing the fits to Event 1. This results in the proposed model as presented in section 2.4.1 and Figure 2.12. Only around an azimuth of 20° does our model produce some postcursors that are not observed in the data.

Figure 2.9a shows the travel times of the proposed model on top of the observed ones. The model does well in fitting the travel time move-out in the main phase as it enters the LLSVP and ULVZ at higher azimuths. The move-out of the postcursor is slightly stronger in the synthetics. Above 60 degrees, both the main phase and the postcursor are more delaid in the oberservations, which can be due to the source or receiver side of the path. Figure 2.10 compares the beamforming results for synthetic models ZF2 and ZL4 to those observed. ZL4, located more to the northeast, does a better job explaining the backazimuth deviation of the postcursor between 55 and 63°. Model ZF2 performs better at azimuths between 50 and 55°. Additionally, the location of ZF2, as constrained by Event 3, cannot be ruled out, as additional focusing could be accounted for by a non-circular ULVZ boundary or other 3D heterogeneity on the Sdiff path beyond the ULVZ, possibly the LLSVP boundary. Additional focusing of the scattered rays, would also account for a more moderate move-out in the postcursor traveltimes (Figure 2.9a).

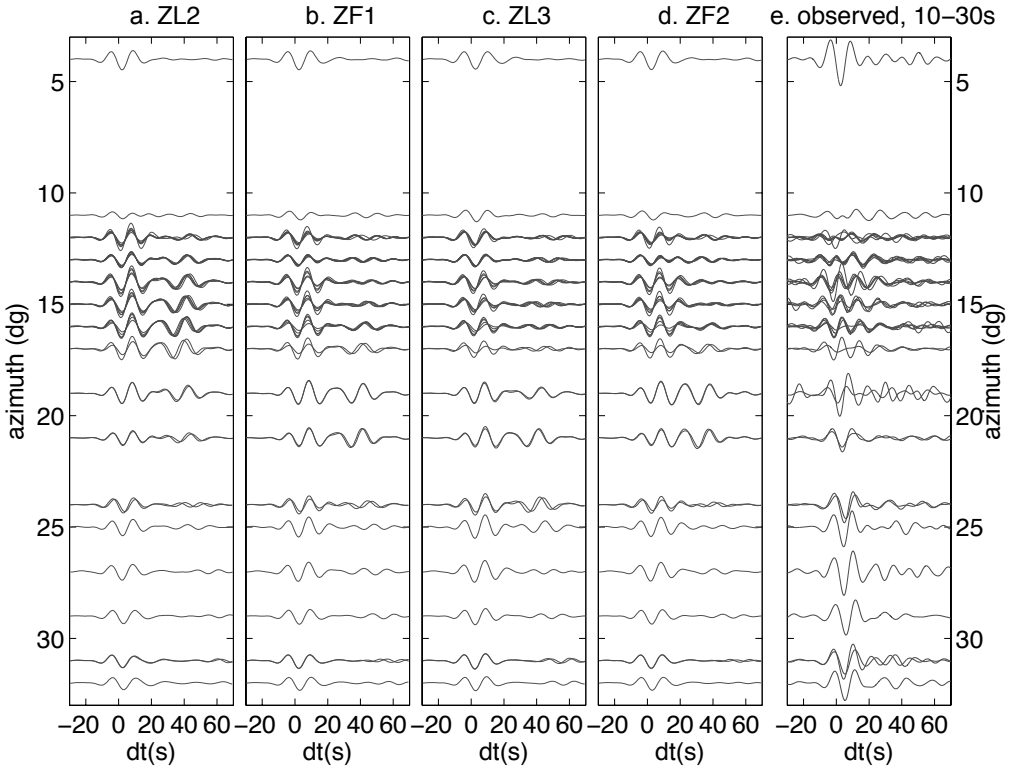

Figure 2.20: .

Panels a-c show a comparison of synthetic traces for Event 3 for models ZL2 (a) and ZL3(c) and one model (ZF1,b) located in between the two. The intermediate model (ZF1,b) fits best, although around 15-17° azimuth a secondary postcursor appears stronger than the first. This is further improved by decreasing the height to 20 km (ZF2), resulting in the waveforms presented in panel d. and Figure 6. Observations (shown in the panel e)around 20° do not exhibit the strong postcursors seen in the synthetics. All waveforms are filtered between 10 and 30s.

2.5 Discussion

The Sdiff phase is not commonly used to detect ULVZs, but as these events illustrate, Sdiff can be strongly affected by ULVZs. In the diffracted part of the phase, it is sensitive to wide structures, like the ULVZ modeled here. The strong effects on the amplitude reduction and strongly delayed postcursor are clearly visible by eye. On the downside, diffracted phases give an integrated sensitivity to the diffracted part, lacking along path resolution (similar to surface waves), and resulting in trade-offs. As shown here, the strongest uncertainty lies in the location, when azimuthal coverage is limited.

The postcursor delay is modeled in reference to the main phase. As the main phase and postcursor have different paths in the D″ there is uncertainty caused by smaller complexities in the ULVZ boundary, velocity gradients with the ULVZ, additional small, slow structures in other parts of the path, CMB topography, the details on the LLSVP boundary and anisotropic velocities. We expect these effects to be on the order of seconds causing the observed scatter in postcursor delay times. Some of these complexities, and unmodeled effects of attenuation, could also explain the stronger decrease in the observed main phase amplitude compared to the synthetics.

The southern boundary of a ULVZ was previously detected in the area studied here through scattering in PKP waves (Luo et al., 2001). Most of the area of our preferred model is located north of this boundary, but the southern end extends across their boundary. Our data coverage does not extend far enough south to see this boundary in the direct phases. However, postcursors from the southernmost part of the ULVZ do diffract northwards and arrive at shorter distances. As the amplitudes of the postcursors at these shorter distances are too strong in the synthetics, this boundary might be more irregular, or not extend as far south as presented here.

Our final model also differs from previous Sdiff postcursor modeling for this region. To et al. (2011) modeled Event 2 combined with an event in 1997. Both these events occurred before the deployment of the Transportable Array and thus coverage was limited. To et al. (2011) modeled the postcursors for a 2D case with a ULVZ embedded in a low velocity zone. Their modeling, however, was restricted to a 2D great circle plane. Their 2D ray-tracing proposed a main phase that travels above the ULVZ, while the postcursor diffracts within the ULVZ and is thus delayed. In contrast, we assume the two phases split due to different sensitivities in the vertical plane as a function of frequency. With the denser coverage of Event 1, it becomes apparent that the amplitude of the main phase at periods shorter than 30s is reduced, while longer periods are less affected. This leads us to propose a much thinner model ($\sim$20 km versus $\sim$80 km).

We note that the Pdiff phases in the 10-20s band for Event 1 show move-out towards the south (Figure 2.5) when entering the LLSVP, but show no further delay due to the ULVZ. This suggests a weaker P velocity reduction, reinforcing the suggestion of a distinct chemical nature or the occurrence of partial melt. However, modeling the exact P velocity reduction is complicated by the strong trade-off with the unknown velocity reduction in the

LLSVP in which the ULVZ is embedded. The present data do not provide any constraints on the density within the ULVZ. Synthetic waveforms for the model do not change when density is increased by 20% within the ULVZ. We also note that, although this ULVZ has a large lateral extent, it is not detected in tomographic models because of its small height.

The location of the ULVZ is close to the northern boundary of the Pacific LLSVP. One of the mechanisms proposed for a possible correlation of ULVZs with LLSVP boundaries is that dense chemically distinct material is dragged and accumulated along the edges of upwelling zones. It generally takes on ridge-like shapes in numerical simulations (McNamara et al., 2010). Here, our best model is cylindrical, but even though we tried some ridge-like features without much success, uncertainty on the precise shape remains. The discrepancy in preferred location between Events 1 and 3 argues for a more elongated shape parallel to the LLSVP boundary.

At the time of the study, this was the first ULVZ for which the lateral dimensions are mapped out with some accuracy. This ULVZ turns out to be more widespread than previous estimates of ULVZ widths (Rost et al., 2010, e.g.) [2]. More recently, an extensive ULVZ has been mapped with the use of SPdKS waveforms beneath the Southern Pacific Ocean (Thorne et al., 2013).

There are also possible correlations between both ULVZs and LLSVP boundaries with hotspots (Torsvik et al., 2006). So far seismological studies do not agree whether whole mantle plumes exist and if yes, whether a whole mantle plume lies directly below the Hawaiian hotspot or is offset somewhere within the mantle (Cao et al., 2011; Wolfe et al., 2011). It is tempting to speculate on the relationship of the unusually large ULVZ found here in close vertical proximity with the hotspot with the largest plume flux (Sleep, 1990; Jellinek and Manga, 2004). If this were the anchor of a long-lived whole-mantle plume, then the plume could be tilted upward to the ENE in the lower mantle. Alternatively, upwelling material could pond at the mantle transition zone and offset further to the east (Cao et al., 2011). Geochemical signature from Hawaiian islands show an enrichment in Fe (Humayun et al., 2004) and an Os isotope signature (Brandon et al., 1998) for which one possible explanation is the interaction with the outer core at the CMB. Entrainment from the ULVZ might be a source for the increased isotopic heterogeneity measured in lavas on the southwestern side compared to lavas on the northeastern side of the Hawaiian chain (Abouchami, 2005; Weis et al., 2011).

2.6 Conclusions

The move-out, amplitude decrease and postcursors observed in shear waves crossing the deep mantle beneath the Central Pacific can be well explained by a ULVZ embedded

[2] Throughout my PhD studies, I have seen quite a number of Sdiff waveforms, and although not the whole CMB region is covered by Sdiff, I have not seen any similar waveform features, suggesting such extensive ULVZs exist elsewhere.

within the LLSVP. The ULVZ width of our preferred model is ∼910 km at the CMB, with a velocity reduction of ∼20%, but some trade-off exists between these two parameters. This is the first time it is possible to provide a constraint on the lateral extent of a ULVZ with some precision. The cylindrical model is centered at 172.5°W and 17.5°N. Although its location is somewhat uncertain, the ULVZ sits close to the northern border of the Pacific LLSVP and to the southwest of the Hawaiian hotspot. The height of 20-25 km is the best constrained parameter due to the frequency dependence of the main phase and postcursor amplitude and separation. Whatever the relationship of the ULVZ to the Hawaian hotspot, the geometry of the mapped structure needs to be taken into account in geodynamics and mineral physics studies of the deep mantle.

2.7 Acknowledgements

We thank Akiko To for helpful discussions. This work was supported by NSF/CSEDI grant 067513 and ERC grant 'WAVETOMO'.

Bibliography

Abouchami, W., 2005. Lead isotopes reveal bilateral asymmetry and vertical continuity in the hawaiian mantle plume. Nature 434, 837–840.

Adelfio, G., Chiodi, M., D'Alessandro, A., Luzio, D., D'Anna, G., Mangano, G., 2012. Simultaneous seismic wave clustering and registration. Computers & Geosciences 44, 60–89.

Bower, D., Wicks, J., Gurnis, M., Jackson, J., 2011. A geodynamic and mineral physics model of a solid-state ultralow-velocity zone. Earth Plan. Sci. Lett. 303 (3-4), 193–202.

Brandon, A., Walker, R., Morgan, J., Norman, M., Prichard, H., 1998. Coupled 186os and 187os evidence for core-mantle interaction. Science 280 (5369), 1570–1573.

Cao, Q., van der Hilst, R., de Hoop, M., Shim, S., 2011. Seismic imaging of transition zone discontinuities suggests hot mantle west of hawaii. Science 332 (6033), 1068–1071.

Capdeville, Y., Larmat, C., Vilotte, J., Montagner, J., 2002. A new coupled spectral element and modal solution method for global seismology- a first application to the scattering induced by a plume-like anomaly. Geophys. Res. Lett. 29, 1318–1322.

Capdeville, Y., To, A., Romanowicz, B., 2003. Coupling spectral elements and modes in a spherical earth: an extension to the sandwichcase. Geophys. J. Int. 154 (1), 44–57.

Clayton, R., Trampert, J., Rebollar, C., Ritsema, J., Persaud, P., Paulssen, H., Prez-Campos, X., Van Wettum, A., Prez-Vertti, A., DiLuccio, F., 2004. The nars-baja seismic array in the gulf of california rift zone. MARGINS Newsletter 13, 1–4.

Davaille, A., 1999. Simultaneous generation of hotspots and superswells by convection in a heterogeneous planetary mantle. Nature 402, 756–760.

Deschamps, F., Kaminski, E., Tackley, P., 2011. A deep mantle origin for the primitive signature of ocean island basalt. Nature Geosc. 4, 879–882.

Dziewonski, A., Anderson, D., 1981. Preliminary reference earth model. Phys. Earth Plan. Int. 25 (4), 297–356.

Dziewonski, A., Lekic, V., Romanowicz, B., 2010. Mantle anchor structure: An argument for bottom up tectonics. Earth Plan. Sci. Lett. 299, 69–79.

Hartigan, J. A., Wong, M. A., 1979. Algorithm as 136: A k-means clustering algorithm. Journal of the Royal Statistical Society. Series C (Applied Statistics) 28 (1), pp. 100–108.

Haskell, N., 1960. Crustal reflection of plane SH waves. J. Geophys. Res. 65 (12), 4147–4150.

He, Y., Wen, L., 2009. Structural features and shear-velocity structure of the pacific anomaly. J. geophys. Res 114, B02309.

Hier-Majumder, S., 2008. Influence of contiguity on seismic velocities of partially molten aggregates. J. geophys. Res 113, B12205.

Houser, C., Masters, G., Shearer, P., Laske, G., 2008. Shear and compressional velocity models of the mantle from cluster analysis of long-period waveforms. Geoph. J. Int. 174 (1), 195–212.

Humayun, M., Qin, L., Norman, M., 2004. Geochemical evidence for excess iron in the mantle beneath hawaii. Science 306 (5693), 91–94.

Ishii, M., Tromp, J., 2004. Constraining large-scale mantle heterogeneity using mantle and inner-core sensitive normal modes. Phys. Earth. Plan. Int. 146 (1-2), 113–124.

Jellinek, A., Manga, M., 2004. Links between long-lived hot spots, mantle plumes, D", and plate tectonics. Rev. of Geoph. 42, RG3002.

Koelemeijer, P. J., Deuss, A., Trampert, J., 2012. Normal mode sensitivity to Earth's D" layer and topography on the core-mantle boundary: What we can and cannot see. Geophys. J. Int. 190 (1), 553–568.

Komatitsch, D., Tromp, J., 2002a. Spectral-element simulations of global seismic wave propagationI. Validation. Geophys. J. Int. 149 (2), 390–412.

Komatitsch, D., Tromp, J., 2002b. Spectral-element simulations of global seismic wave propagationII. Three-dimensional models, oceans, rotation and self-gravitation. Geophys. J. Int. 150 (1), 303–318.

Luo, S., Ni, S., Helmberger, D., 2001. Evidence for a sharp lateral variation of velocity at the core-mantle boundary from multipathed PKPab. Earth Plan. Sci. Lett. 189 (3-4), 155–164.

Mao, W., Mao, H., Sturhahn, W., Zhao, J., Prakapenka, V., Meng, Y., Shu, J., Fei, Y., Hemley, R., 2006. Iron-rich post-perovskite and the origin of ultralow-velocity zones. Science 312 (5773), 564–567.

Masters, G., Laske, G., Bolton, H., Dziewonski, A., 2000. The relative behavior of shear velocity, bulk sound speed, and compressional velocity in the mantle: implications for chemical and thermal structure. AGU Monograph 117, 63–88.

McNamara, A., Garnero, E., Rost, S., 2010. Tracking deep mantle reservoirs with ultra-low velocity zones. Earth Plan. Sci. Lett. 299, 1–9.

McNamara, A., Zhong, S., 2004. Thermochemical structures within a spherical mantle: Superplumes or piles. J. geophys. Res 109, B07402.

McNamara, A., Zhong, S., 2005. Thermochemical structures beneath Africa and the Pacific ocean. Nature 7062, 1136–1139.

Mégnin, C., Romanowicz, B., 2000. The three-dimensional shear velocity structure of the mantle from the inversion of body, surface and higher-mode waveforms. Geophys. J. Int. 143 (3), 709–728.

Ni, S., Helmberger, D., 2003. Seismological constraints on the South African superplume; could be the oldest distinct structure on earth. Earth Plan. Sci. Lett. 206 (1-2), 119–131.

Ni, S., Tan, E., Gurnis, M., Helmberger, D., 2002. Sharp sides to the African superplume. Science 296 (5574), 1850–1853.

Rondenay, S., Fischer, K., 2003. Constraints on localized CMB structure from multichannel, broadband SKS-coda analysis. J. Geophys. Res. 108, 2537–2553.

Rost, S., Garnero, E., Stefan, W., 2010. Thin and intermittent ultralow-velocity zones. J. Geophys. Res. 115, B06312.

Rost, S., Garnero, E., Williams, Q., 2006. Fine-scale ultralow-velocity zone structure from high-frequency seismic array data. J. Geophys. Res. 111, B09310.

Rost, S., Garnero, E., Williams, Q., Manga, M., 2005. Seismological constraints on a possible plume root at the coremantle boundary. Nature 435 (7042), 666–669.

Sleep, N., 1990. Hotspots and mantle plume: some phenomelogy. J. Geophys. Res. 95, 6715–6736.

Steinberger, B., Torsvik, T., 2012. A geodynamic model of plumes from the margins of large low shear velocity provinces. Geochem. Geophys. Geosyst. 13, Q01W09.

Sun, D., Helmberger, D., Ni, S., Bower, D., 2009. Direct measures of lateral velocity variation in the deep earth. J. Geophys. Res. 114 (B5), B05303.

Tan, E., Leng, W., Zhong, S., 2011. On the location of plumes and lateral movement of thermochemical structures with high bulk modulus in the 3-D compressible mantle. Geochem. Geophys. Geosyst. 12, Q07005,.

Thorne, M., Garnero, E., 2004. Inferences on ultralow-velocity zone structure from a global analysis of spdks waves. J. geophys. Res 109, B08301.

Thorne, M., Garnero, E., Jahnke, G., Igel, H., McNamara, A., 2013. Mega ultra low velocity zone and mantle flow. Earth and Planetary Science Letters 364, 59–67.

To, A., Capdeville, Y., 2011. Constraints on the 3d shape of the ultra low shear velocity zone at the base of the mantle beneath the central pacific. AGU 2011 Fall meeting San Francisco, Dec 5-9, DI43A–2082.

To, A., Fukao, Y., Tsuboi, S., 2011. Evidence for a thick and localized ultra low shear velocity zone at the base of the mantle beneath the central Pacific. Phys. Earth. Plan. Int. 184, 119–133.

To, A., Romanowicz, B., Capdeville, Y., Takeuchi, N., 2005. 3D effects of sharp boundaries at the borders of the African and Pacific superplumes: Observation and modeling. Earth Plan. Sci. Lett. 233 (1-2), 1447–1460.

Torsvik, T., Smethurst, M., Burke, K., Steinberger, B., 2006. Large igneous provinces generated from the margins of the large low-velocity provinces in the deep mantle. Geophys. J. Int. 167 (3), 1447–1460.

Trampert, J., Deschamps, F., Resovsky, J., Yuen, D., 2004. Probabilistic tomography maps chemical heterogeneities throughout the lower mantle. Science 306 (5697), 853–856.

Tromp, J., Komattisch, D., Liu, Q., 2008. Spectral-element and adjoint methods in seismology. Commun. Comput. Phys. 3 (1), 1–32.

Weis, D., Garcia, M., Rhodes, J., Jellinek, M., Scoates, J., 2011. Role of the deep mantle in generating the compositional asymmetry of the Hawaiian mantle plume. Nature Geosc. 4, 831–838.

Wicks, J., Jackson, J., Sturhahn, W., 2010. Very low sound velocities in iron-rich (mg, fe) o: Implications for the core-mantle boundary region. Geophys. Res. Lett. 37, Art. No. L15304.

Williams, Q., Garnero, E., 1996. Seismic evidence for partial melt at the base of earth's mantle. Science 273 (5281), 1528–1530.

Wolfe, C., Solomon, S., Laske, G., Collins, J., Detrick, R., Orcutt, J., Bercovici, D., Hauri, E., 2011. Mantle P-wave velocity structure beneath the Hawaiian hotspot. Earth Plan. Sci. Lett. 303 (3-4), 267–280.

Yuan, H., Romanowicz, B., 2010. Lithospheric layering in the North American craton. Nature 466, 1063–1068.

x

Chapter 3

Direct seismic observations of the Perm anomaly

3.1 Introduction

The lowermost mantle shear wave velocity structure is dominated by degree-two and three velocity anomalies in the form of the so-called African and Pacific Large Low Shear Velocity Provinces (LLSVPs, Dziewonski et al. (2010)). The question remains if these LLSVPs are also compositionally distinct from the rest of the lower mantle. In global waveform tomography these structures appear seismically smooth, but this could be solely due to the spatial smoothing of the inversion method. Regional seismic waveform studies have shown that the boundaries appear to be seismically sharp causing waveform complexities through the presence of multi-pathing around the boundary (Ni et al., 2002; To et al., 2005, e.g). In the previous chapter we saw evidence of smaller-scaled distinct composition in thin (10s of km), localized zones revealed by strong postcursors.

Ved Lekic (and collaborators) found a novel way to apply clustering to combine the results of several global tomography model and analyze the consistency in the way the LLSVP structures are mapped(Lekic et al., 2012). The suggested LLSVP boundary resulting from his method between LLSVP and non-LLSVP appears fairly consistent across models in most locations. This approach led to the discovery of an additional, isolated slow anomaly, dubbed 'the Perm Anomaly'. Their method and the results are described in the next chapter. My part on this project consisted in finding direct seismic evidence for the existence of this anomaly from observed seismic waveforms. The data are described in section 4.3, and forward modeling results for geometrically simple anomalies are shown in section 3.4. We find a structure with lateral dimensions that are comparable to the ULVZ in the previous chapter, but that extends higher (100s of km) above the CMB and has velocity reductions similar to the LLSVP structures.

3.2 Background on the clustering results

Ved Lekic and co-authors apply clustering analysis to a number of global tomographic models of seismic shear velocity in the lower mantle. Clustering analysis is an objective way to find groups with similarities from a large group of data. In this case the clustering analysis is done on radial shear wave velocity profiles from equally spaced locations on the Earth. The distance measure is defined as the squared Euclidean distance between two profile vectors. The method of 'k-means' clustering is applied, where k is a pre-defined integer that defines the number of resulting groups/clusters. K-means clustering starts with grouping the profiles randomly into k clusters. The mean of these clusters are then calculated, after which all the profiles are reassigned to the nearest mean. Calculating the mean, and reassigning the profiles is done iteratively until the clusters converge to the stage of minimum intra-cluster variance.

The method is applied separately to five recent tomographic models: SAW24B16: Mégnin and Romanowicz (2000); HMSL-S: Houser et al. (2008); S362ANI: Kustowski et al. (2008); GyPSuM: Simmons et al. (2010); S40RTS: Ritsema et al. (2011). All models are filtered up to spherical harmonic degree 12. Through the k-means clustering, each model subdivides into a fast cluster and slow cluster. The results are summarized in Figure 3.1 by counting at each location how many models are assigned to the slow cluster, i.e. a 'vote' map. It is remarkable how consistent the slow features are between the different models, given the fact that these models are based on inversions with different data sets, parameterizations, theoretical framework and regularizations.

The African LLSVP has an elongated structure, and many of its boundaries that come out of the clustering appear consistently across the models. Its southernmost boundary beneath the Indian Ocean appears sharp. There are a number of local waveform studies that confirm the sharpness of this boundary through seismic waveform complexities (Ni et al., 2002; To et al., 2005). The strongest uncertainty in this structure across models lies beneath central Africa, but this could be due to poor data coverage in this region.

The Pacific LLSVP appears as a more circular feature, situated around the equator. Many of its boundaries appear consistent especially on its Western side. At the northern boundary, close to Hawaii, there appears little consistency across the models, while there are numerous large events from the New Ireland Region to stations in North America with sensitivity to this region. The waveforms from the main event in Chapter 2 have sensitivity to this region, but show no evidence (i.e. postcursors) of a sharp boundary, although this boundary might be masked by the presence of the ULVZ. It also remains a question if this is merely a lack of a sharp near-vertical boundary, and the LLSVP is more gradual. The clustering beneath the Pacific gives suggestion of one, or possibly two piles that might be (partially) disconnected from the main pile in the South Pacific. However, so far, we have found no direct waveform evidence for this separation.

The one exception to these two large slow structures surrounded by the continuous fast region, is the Perm Anomaly, beneath the city of Perm and the Ural mountains (indicated

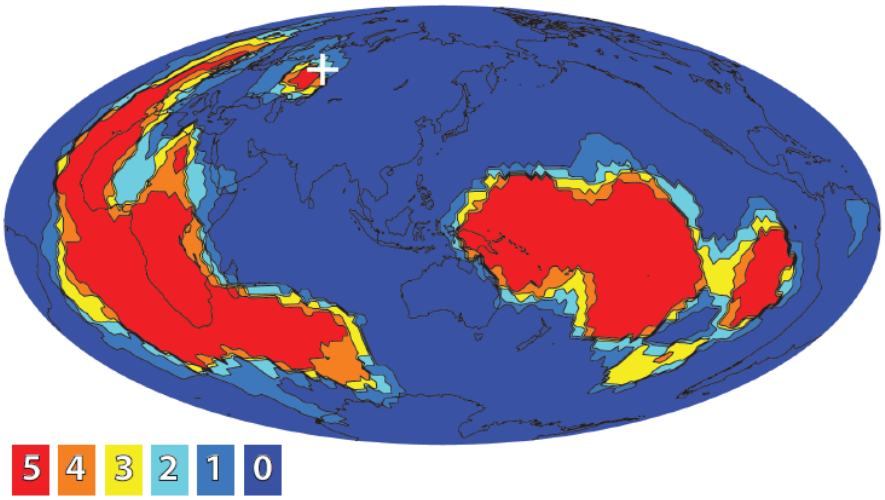

Figure 3.1: Clustering results for shear wave velocity profiles in the lower mantle from five different global models. For each location the number of profiles pertaining to one cluster are counted, resulting in two fairly constrained regions. One is the continuous faster-then-average region, and the other are the Pacific and African LLSVPs. One exception to this, is a small region beneath the Russian city, Perm, as indicated by the white cross. This region is 'counted' to be similar to LLSVPs, but is a lot smaller in its extent. The goal of this project is finding evidence of slow material in this region from seismic waveforms. (Figure courtesy of Ved Lekic.)

by the white cross in Figure 2.6.) All five models agree on the presence of slow material here. In the rest of this chapter, I will present direct evidence for the presence of slow material in this region from, delayed and focused, shear diffracted waveforms.

3.3 Data set

3.3.1 from West to East

A large, deep event occurred beneath southern Spain on April 11th 2010. The event occurred at 617 km, which is unique in this area as intermediate depth events are absent. This deep event appears to occur here roughly every 20 years, although not always at this magnitude (Buforn et al., 2011). The shear core-diffracted phases of this event are sensitive to the deepest mantle around the Perm Anomaly and then come up to stations in Japan and Taiwan. The configuration is shown in Figure 3.2 (panel a).

The raw waveforms are rotated to the transverse and radial components and filtered between 10 and 30 seconds. The transverse waveforms are windowed around the shear diffracted arrival and plotted in panel (a) of Figure 3.2. We measure cross-correlated dif-

ferential travel-times and amplitude ratios compared to reference normal mode synthetics for the 1D model PREM (Dziewonski and Anderson, 1981). These are plotted in panels (e) and (f). The amplitudes of the waveforms decrease from smaller to larger azimuths due to the radiation pattern of the source, but this is corrected for by referencing to synthetic waveforms in panel (e). The node of the radiation pattern occurs around an azimuth of 70°. These measurements show increased amplitudes ($\sim$ 2x) and delayed waveforms ($>$ 5 sec) around an azimuth of $\sim$ 50°. These delays and amplitude enhancements can also be directly observed from the waveforms. We will model these effects of delay and energy focusing in the following section. At the smallest azimuths we also see some larger amplitudes and delayed arrivals, which may be part of the African LLSVP beneath Scandinavia. Modeling this edge of the African LLSVP is beyond the scope of this project.

The delay and focusing in these shear phases are persistent over a broad period range. This implies that the structure causing these effects extends over a couple hundred kilometers above the CMB. In Chapter 2, we have seen that anomalies on the order of 10s of km thick only affect periods shorter than 30 seconds. In that case the frequency dependence of the observations could constrain the exact height of the structure. Here, we do not seem to have that sensitivity to the top of the structure, and thus it is probably several hundred kilometers high. Possibly, a more precise constraint on the height of the structure could be reached with data at shorter distances that bottom several hundreds of kilometers above the CMB (e.g. from the 2010 Spain event to stations in China).

3.3.2 from East to West

Events in Japan and Kuril Islands towards Europe and Africa also have sensitivity to the Perm Anomaly and its surroundings in the D″. Unfortunately, the coverage in central North Africa is suboptimal at the present time, with one valuable GEOSCOPE station in southern Algeria called TAM. The coverage and data are shown in Figure 3.3. The waveforms in Figure 3.3 are rotated and filtered between 10 and 30s. The waveforms are individually normalized to normal mode synthetics for the specific event-station pairs to take out any source effects. As the orientation of the anomaly towards each event is different, these waveforms are not organized by azimuth, but by the latitude with which they intersect with 57° longitude (the estimated center of the Perm Anomaly, shown by the black line on the map). The data set shows delayed phases around 50° latitude. Besides some strong phases in the far North (and one trace in the South), in general, the phases between 50-55° latitude have larger amplitudes. Some additional scatter is present and is probably due to unmodelled source effects.

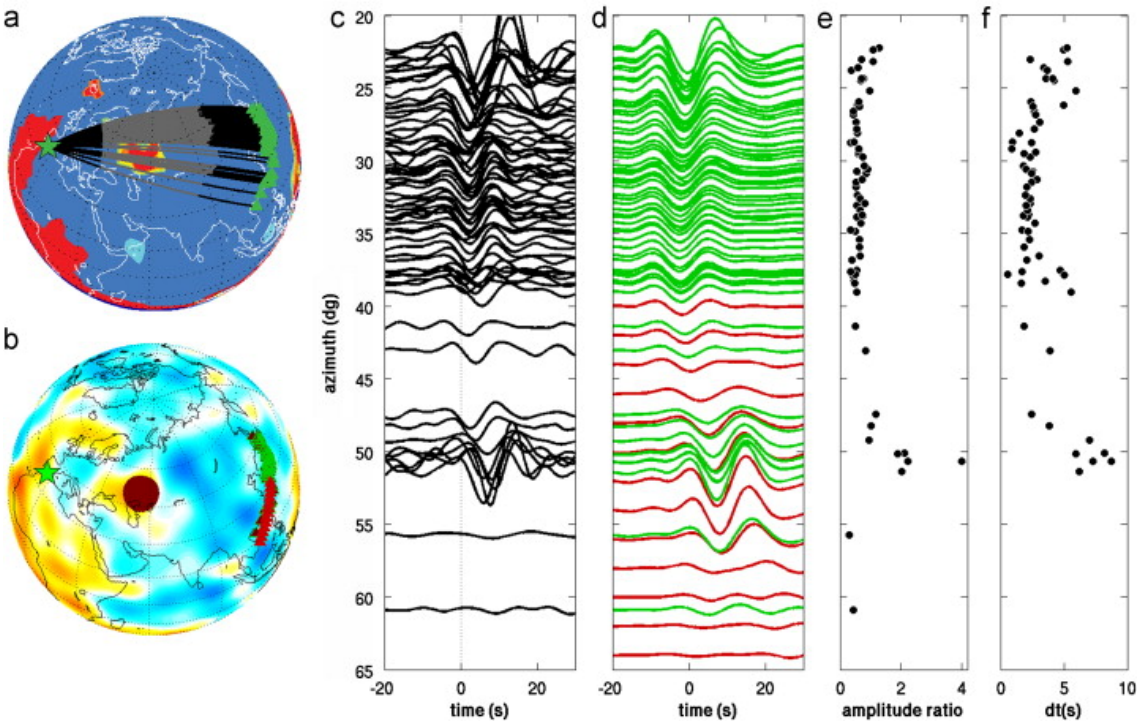

Figure 3.2: Seismic transverse-component velocity waveforms from the deep Spain event of April 11th 2010 (Buforn et al., 2011) observed at 66 stations in the 91-102 distance range show travel time delays and amplitude focusing due to the Perm Anomaly. (a) Great circle paths and their relation to the Perm Anomaly. Lighter shading indicates the portion of the path within the D″ region. Triangles indicate stations. (b) Simple cylindrical 3D model that best reproduces the first order features in the data. The model includes a 370 km high cylinder with a diameter of 900 km (at the CMB) and a velocity reduction of -6% centered at 54E, 50N. The background model is SAW24B16 (Mgnin and Romanowicz, 2000). Real stations (green) are augmented with a set of hypothetical stations (red) to complement available azimuthal coverage. (c) Observed and (d) synthetic S/Sdiff waveforms filtered between 10-30 sec and ordered as a function of azimuth. Strong travel time delays and amplitude focusing due to the Perm Anomaly appear around 50 in azimuth. No similar time delays are observed to the north, indicating that the Perm Anomaly is not connected to the Iceland region of the African LLSVP. The same color convention is used for synthetic traces as in (b). Observed Sdiff amplitude ratios (e) and differential travel times (f) as a function of azimuth, referred to 1D normal mode synthetics. Travel time measurements could not be made for the nodal traces at the largest azimuths.

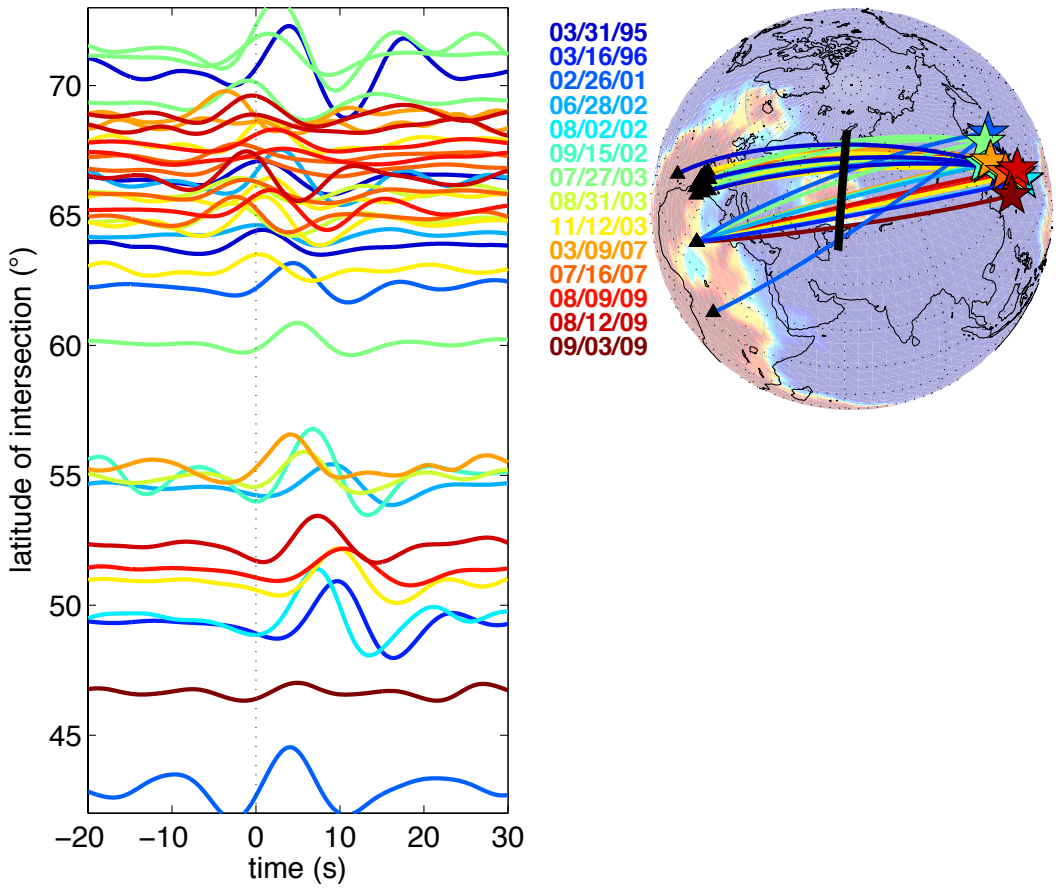

Figure 3.3: Seismic transverse-component velocity waveforms from the deep events in Japan to stations on Iberia and in Africa. The waveforms are filtered between 10 and 30s. The waveforms on the left and ray paths on the globe on the right are color-coded per event. As the azimuthal relationship between the event and anomaly differs per event, the waveforms are organized by the intersecting latitude between the ray path and 57° longitude (as indicated by the black line on the map.

3.4 Modeling Results

Due to computational costs of forward modeling several events, we focus on forward modeling the 2010 Spain event, which has the best station coverage.

To constrain that the observed delays and energy focusing are caused by the Perm Anomaly, we forward model Sdiff waveforms for several possible anomalies. Here we represent the Perm Anomaly with a simplified cylindrical shape. Initially we predict the effect of such a shape by ray-theoretical forward modeling. The ray-theoretical focusing of seismic energy through such an lens-like anomaly can be seen in Figure 3.4. This anomaly is 800 km wide (at its base at the CMB) with a 6% velocity reduction. The refraction at the boundaries are simply predicted by Snell's law. This method allows us to somewhat explore the space, without computational costs. We conclude that velocity reductions of -3-4% as typically seen in seismic inversions of LLSVP's and the Perm Anomaly are insufficient to cause significant energy focusing. However, it is not surprising that the amplitude of such anomalies is underestimated. This underestimation is due to spatial smoothing in the seismic inversion method, and wavefront healing effects, which is more effective in annihilating the distortion in the waveform for slow anomalies at large depths (Malcolm and Trampert, 2011).

We present full-waveform synthetics for three different models in Figure 3.5. The first is a broad anomaly (1100 km) with 3% velocity reduction. This one produces some, but not sufficient focusing. The next panel shows a more focused anomaly (800 km across, -6% shear wave velocity), resulting in more localized delayed and stronger waveforms. The last model has a 10% velocity reduction. Both panels (b) and (c) show the presence of postcursors. The postcursors for the last model are significant, and we don't see evidence for this in the waveforms. We therefore disregard the 10% velocity reduction as too strong. The weak postcursors in the second panel could be hard to see in the real data. There is some indication of a post cursor in the southernmost observed trace (at 61°), but unfortunately there is not a lot of coverage to better constrain this.

In Figure 3.2 panel (d), the waveforms for our best models are shown, next to the observed waveforms. The strength of the local focusing at 50° is still somewhat underestimated by the model. The travel time delay is more gradual in the synthetics and the data, which might be an indicator of a non-circular boundary in the north.

3.5 Discussion

Through the similarities in height and velocity reduction, it is not unlikely that the Perm anomaly has a similar composition as the LLSVPs. The thermo-chemical dynamics that have formed or are influenced by the Perm anomaly remain a question (just as for LLSVPs). Has this anomaly been at this location over geological times? Or has it recently

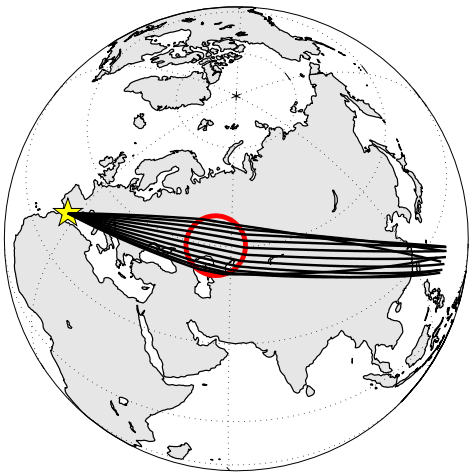

Figure 3.4: Ray-theoretical focusing of energy by the Perm Anomaly for the 2010 Spain event. The anomaly has a radius of 400 km and a velocity reduction of 6%.

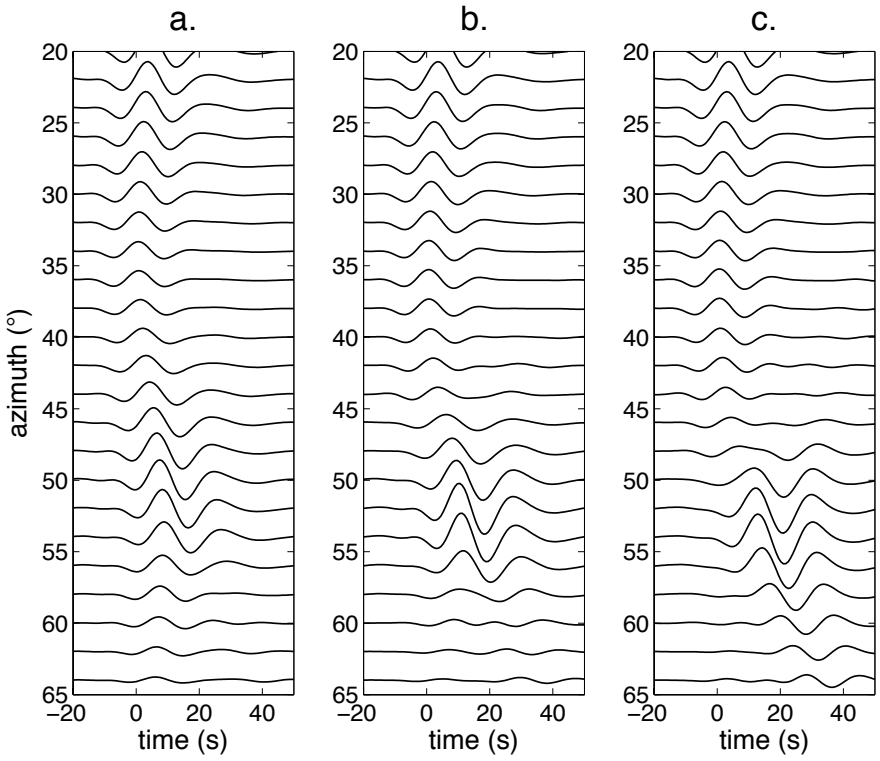

Figure 3.5: Synthetic transverse waveforms as a function of azimuth at a distance of 100° for three different models. All three cylindrical anomalies are centered at 57° longitude and 50° latitude and have a height of 370 km (the height of the SEM mesh in sandwiched-CSEM). a. a cylindrical anomaly with a radius of 550 km and velocity reduction of 3%. b. 400 km in radius and 6% velocity reduction. c. 400 km in radius and 10% velocity reduction.

been separated from the African or Pacific LLSVP, or is it doomed to eventually merge with the African LLSVP?

If the Perm anomaly has remained at $(57°E, 50°N)$ over ancient times, its location lines up nicely with a large igneous eruption that marked the end of the Permian. The Siberian Traps flood basalts are the resulting large igneous province of this eruption ($\sim 250Ma$). As the name suggest, the Siberian Traps are currently located in Siberia, but pale-reconstruction puts them exactly above the Perm anomaly at the time of eruption (Torsvik et al., 2008). Whether, in general, large eruptions like this one can be linked to mantle plumes and have a deep-mantle origin, remains a question.

It also remains a question if a compositional anomaly of the size of the Perm anomaly can remain stable in one place over large intervals of time? This appears hardly the case in thermo-chemical models in the lowermost mantle. In the thermo-chemical model by Steinberger and Torsvik (2012), a chemical anomaly is separated from the Pacific LLSVP by a subducting slab roughly 80 Ma ago. This material appears to be pushed to the West and lines up nicely with our modeled Perm location. At present, in their model, the material appears to start to be swept up by the African anomaly.

3.6 Conclusions

We found evidence for the delay and focusing of energy in diffracted waveforms by slow material present on the core-mantle boundary under the Ural mountains, named the Perm Anomaly. Suggestion of this slow pile came from a consistent slow anomaly across all global waveform tomography model. Evidence results from waveforms from a deep earthquake in Spain to stations in Japan and Taiwan, as well as Japanese earthquakes to stations in Europe and Africa. The delays and focusing can be modeled with a cylindrical anomaly of several 100s of kilometers in radius and 6% velocity reduction. The anomaly is very similar in size to the ULVZ modeled in the previous chapter, but is a lot taller and has less of a velocity reduction. Its composition is therefore more likely to be similar to that of the LLSVPs.

3.7 Acknowledgements

I would like to thank the main authors Ved Lekic, Barbara Romanowicz and Adam Dziewonski for the initial finding of the Perm Anomaly, and for entrusting me with the task of finding pure waveform evidence. This work was published in *Earth and Planetary Science Letters* in 2012.

Bibliography

Buforn, E., Pro, C., Cesca, S., 2011. The 2010 Granada, Spain, Deep Earthquake. BSSA 101 (5), 2418–2430.

Dziewonski, A., Anderson, D., 1981. Preliminary reference earth model. Phys. Earth Plan. Int. 25 (4), 297–356.

Dziewonski, A., Lekic, V., Romanowicz, B., 2010. Mantle anchor structure: An argument for bottom up tectonics. Earth Plan. Sci. Lett. 299, 69–79.

Houser, C., Masters, G., Shearer, P., Laske, G., 2008. Shear and compressional velocity models of the mantle from cluster analysis of long-period waveforms. Geoph. J. Int. 174 (1), 195–212.

Kustowski, B., Ekström, G., Dziewoski, A., 2008. Anisotropic shear-wave velocity structure of the Earth's mantle: a global model. J. Geophys. Res 113 (B6), B06306.

Lekic, V., Cottaar, S., Dziewonski, A. M., Romanowicz, B., 2012. Cluster analysis of global lower mantle tomography: A new class of structure and implications for chemical heterogeneity. Earth Plan. Sci. Lett 357-358, 68–77.

Malcolm, A. E., Trampert, J., Apr. 2011. Tomographic errors from wave front healing: more than just a fast bias. Geophys. J. Int. 185 (1), 385–402.

Mégnin, C., Romanowicz, B., 2000. The three-dimensional shear velocity structure of the mantle from the inversion of body, surface and higher-mode waveforms. Geophys. J. Int. 143 (3), 709–728.

Ni, S., Tan, E., Gurnis, M., Helmberger, D., 2002. Sharp sides to the African superplume. Science 296 (5574), 1850–1853.

Ritsema, J., Deuss, A., van Heijst, H. J., Woodhouse, J., 2011. S40RTS: a degree-40 shear-velocity model for the mantle from new Rayleigh wave dispersion, teleseismic traveltime and normal-mode splitting function. Geophys. J. Int. 184 (3), 1223–1236.

Simmons, N., Forte, A., Boschi, L., Grand, S., 2010. GyPSuM: A joint tomographic model of mantle density and seismic wave speeds. J. Geophys. Res.

Steinberger, B., Torsvik, T. H., 2012. A geodynamic model of plumes from the margins of Large Low Shear Velocity Provinces. Geochem. Geophys. Geosyst. 13, Q01W09.

To, A., Romanowicz, B., Capdeville, Y., Takeuchi, N., 2005. 3D effects of sharp boundaries at the borders of the African and Pacific superplumes: Observation and modeling. Earth Plan. Sci. Lett. 233 (1-2), 1447–1460.

Torsvik, T. H., Steinberger, B., Cocks, L. R. M., Burke, K., 2008. Longitude: linking Earth's ancient surface to its deep interior. Earth Plan. Sci. Lett. 276 (3-4), 273–282.

Chapter 4

Observations of changing anisotropy across the southern margin of the African LLSVP

4.1 Introduction

Much of our knowledge on the distribution and characteristics of heterogeneity in the interior of our planet comes from the study of seismic wave velocities. Specifically, the study of seismic anisotropy (i.e. the variation of seismic wave speeds with direction of propagation and polarization) provides information about the direction of material flow and therefore constrains the dynamics in the interior (Karato, 1998b). In the Earth, seismic anisotropy appears strong in the upper mantle and the lowermost lower mantle (D″); i.e. in boundary layers where strains caused by horizontal flow tend to be large (e.g. Montagner, 1998). Some seismic anisotropy may also be present in the mantle transition zone (Trampert and van Heijst, 2002) and in the inner core (Woodhouse et al., 1986; Morelli et al., 1986).

Anisotropy in the upper mantle has been linked to flow in the asthenosphere and the subsequent deformation and preferred orientation of intrinsically anisotropic minerals (Karato, 1998a, e.g.). For the olivine-dominated upper mantle, an olivine single crystal is seismically fast along its c-axis (Mainprice et al., 2000). Dislocation creep along preferred slip planes in the olivine crystals accommodates the flow. The subsequent preferred alignment along these slip planes produces seismic anisotropy at the polycrystal scale. The resulting signature of anisotropy, however, ultimately depends on which slip plane is preferred, which for olivine might depend on its water content (Karato et al., 2008). This makes interpretation of observed seismic anisotropy under different tectonic environments somewhat ambiguous.

Even less is known about interpreting seismic anisotropy in terms of flow in D″, al-

though there have been recent advances (see overview in Nowacki et al. (2011)). Firstly, it is unclear if the lowermost mantle is composed of perovskite (Pv) or postperovskite (pPv), or if the composition varies laterally (e.g. Mosca et al., 2012). These two mineral phases have intrinsically different single crystal anisotropy (Wentzcovitch et al., 2006; Stackhouse et al., 2005). Secondly, interpretation will depend on the dominant lattice plane along which deformation by dislocation creep occurs. The same preferred plane of deformation is consistently measured for Pv (e.g. Wenk et al., 2011), but remains ambigious for pPv (e.g. Miyagi et al., 2011). Different dominant slip planes for pPv result in opposite signatures in radial anisotropy (Wenk et al., 2011; Walker et al., 2011). Lastly, it is uncertain if dislocation creep is present in the lowermost mantle, or if deformation is dominated by diffusion creep (McNamara et al., 2001). The latter would not result in seismic anisotropy.

Ultimately, observations of seismic anisotropy need to be linked to numerical geodynamical models to confirm the conditions under which mapped flow occurs. There are a number of factors that can largely influence the models proposed for the lowermost mantle. One is the role of possibly chemically distinct LLSVPs (large low shear velocity provinces, Garnero and McNamara (2008); Lekic et al. (2012)), which can largely change the pattern of flow (McNamara and Zhong, 2005; Steinberger and Torsvik, 2012). Also little is known about the strength, and the subsequent bending, squishing, or buckling, of the slabs as they reach the core-mantle boundary (CMB) (Loubet et al., 2009). Constraining seismic anisotropy can provide clarifications on the assumptions made in these models.

Besides mineralogical and geodynamical uncertainties, seismological observations have certain limitations, as the full 3D anisotropic signature is never resolved. One can only constrain those components of the elastic tensor that the seismic data set is sensitive to, and the resolution is limited to the wavelengths of the observed waves. The signature and resolution of a heterogeneous medium that can be mapped by seismic waves is called the effective medium. Intrinsically isotropic material can result in anisotropy in the effective medium, for example when layering or other heterogeneity is present (Crampin, 1984). This non-uniqueness adds a degree of complexity to the interpretation of observations of anisotropy. Different seismic phases can constrain different modes of anisotropy. Most accessible are radial and azimuthal anisotropy. Radial anisotropy is commonly observed in D″, from forward waveform modeling (e.g. Vinnik et al., 1995; Garnero and Lay, 1997) or by tomographic inversion (Panning and Romanowicz, 2006; Kustowski et al., 2008; Kawai and Geller, 2010), while azimuthal anisotropy remains difficult to constrain in D″ due to limited azimuthal coverage. Local studies constrain the azimuthal component of the elastic tensor from SKS-$SKKS$ differential splitting measurements (Niu and Perez, 2004; Restivo and Helffrich, 2006; Wang and Wen, 2007; Long, 2009; Lynner and Long, 2012) and with ScS waves (Garnero et al., 2004; Maupin, 2005; Thomas et al., 2007; Nowacki et al., 2010). The latter gives improved azimuthal constrains when crossing rays are available (Wookey and Kendall, 2008), otherwise only the tilted anisotropy component orthogonal to the direction of propagation can be constrained. Here we apply shear wave splitting analysis to shear diffracted waveforms at large distances.

In Section 4.2.1, we describe the methodological approach using shear wave splitting

and forward modeling. In Section 4.3 we introduce the anomalous observations of S_{diff} from a Fiji event towards the Kaapvaal array in Africa. From the analysis of the data in Section 5.3, we argue that the strong arrival of S_{diff} on the radial component is caused by the presence of tilted anisotropy in D″. Through shear wave splitting, we constrain the average fast axis direction. Additional confirmation comes from the computation of synthetic waveforms for anisotropic models using a numerical spectral element method. The forward modeling also allows us to constrain the lateral and radial extent of the anisotropy.

4.2 Methods

4.2.1 Shear wave splitting measurements in S_{diff}

Shear diffracted waves (S_{diff}) at large distances become polarized along the SH component. The SV component attenuates along the diffracted path due to P-SV coupling with the outer core (Teng and Richards, 1976; Doornbos and Mondt, 1980; Komatitsch et al., 2010). This effect, which gets stronger as a function of distance, is illustrated by synthetics in Figure 4.1 for three different velocity models. The SV component is negligibly small beyond 110°. The polarization along one component gives the use of the S_{diff} phase at large distances the same advantage as the use of SKS when measuring shear wave splitting in upper mantle studies; while the SKS phase has a known initial polarization on the radial component, the S_{diff} phase is polarized on the transverse component at large distances. Additionally, in the case of S_{diff}, any interaction between the SH and SV components due to source-side upper mantle or D″ anisotropy can be ignored. Indeed, any resulting energy on the SV component from coupling on the source side will attenuate out along the diffracted part of the path. The only effect of anisotropy on S_{diff} on the source side is a decrease in the amplitude of the final SH component through coupling with SV and loss of energy to the outer core.

In SKS studies, the incident angle of the SKS phase is often assumed to be vertical, subsequently interpreting the anisotropy to be in the horizontal plane, orthogonal to the direction of propagation. For an S_{diff} phase turning upwards in the D″, the incidence angle will vary as a function of position along the path. The shear wave splitting in the phase will only be sensitive to anisotropy in the plane orthogonal (R, T) to its direction of propagation (k). In Figure 4.2, we define the fast axis ϕ in the reference frame of the phase.

Given that the initial polarization is known, one can apply any of the single-station methods that are applied to measure splitting in the case of SKS. Here we have applied the *rotation-correlation* or *cross-correlation* method (Bowman and Ando, 1987) as implemented in SplitLab (Wüstefeld et al., 2008). This method rotates the horizontal components and calculates the cross-correlation values between the two rotated components for all possible angles. The maximum cross-correlation coefficient corresponds to the rotation angle at which the fast and slow waveforms are most orthogonal. This rotation angle is the fast axis direction ϕ. The splitting time dt is the shift between the fast and slow waveforms

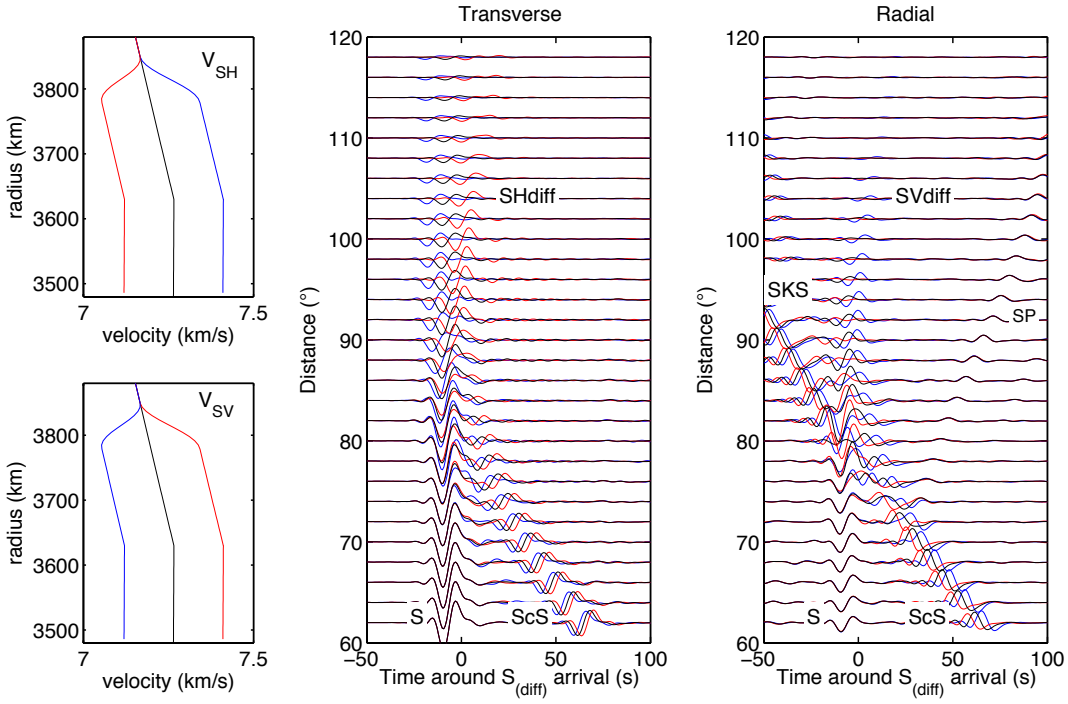

Figure 4.1: Velocity models (left) and synthetic waveforms (right) for transverse isotropic models. Black models and seismograms are for PREM. The blue (respectively red) velocity model has V_{SH} 2% faster (resp. slower) and V_{SV} 2% slower (resp. faster) than PREM in the lowermost 300 km of the mantle. Both models are smoothed towards PREM over 70 km. This synthetic test illustrates the fast decay of SV_{diff}, even when V_{SV} is slow, in the shadow of the core. Additionally the integrated travel time difference between $SH-$ and SV_{diff} increases strongly at these distances. Transverse isotropy causes no coupling between the SV and SH component as the lack of an SKS arrival on the SH components illustrates.

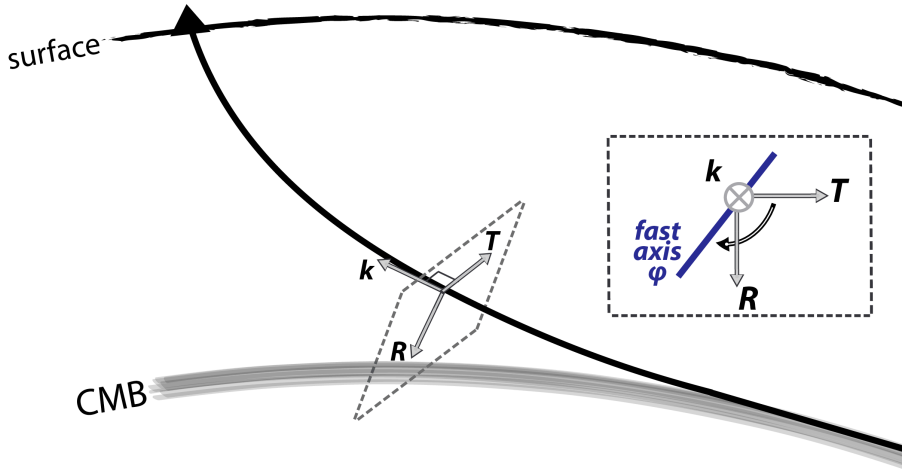

Figure 4.2: Definition of (R, T, k) reference frame and the fast axis ϕ within it.

after rotation. We compare the results of this method with methods that grid search to attempt to minimize the energy on the radial component (Silver and Chan, 1991; Vinnik et al., 1989). For stations with strong splitting the two methods gave similar results; we prefer the rotation-correlation method as it is easier to recognize the null measurements.

4.2.2 Full waveform modeling with CSEM

Forward modeling of full waveforms in various anisotropic models is performed using the 'sandwiched' version of the coupled spectral element method CSEM (Capdeville et al., 2002, 2003). CSEM solves the wave equation using the spectral element method in the mantle, while it solves a normal mode solution for a 1D velocity model in the core. The two are connected at the core-mantle boundary through a Dirichlet-to-Neumann operator. The sandwiched version of CSEM applies the 1D normal mode solution both in the core and in most of the mantle, and only solves the fully 3D case in one layer: in our case the lowermost 370 km of the mantle. For our application of repeated simulations for the same event for different 3D models in D″, this method is computationally advantageous, as the normal mode computation is fast and only needs to be done once per event. We have extended the sandwiched CSEM code to include fully anisotropic tensors in the velocity model.

We describe our models in terms of the fast direction ϕ, and the ratio of the fast and slow velocities, in the plane orthogonal to the estimated direction of propagation (Figure 4.2). We compute the perturbations to the elastic tensor in the reference frame of the propagating wavefront $(\boldsymbol{R}, \boldsymbol{T}, \boldsymbol{k})$ (Figure 4.3(b)). These perturbations are rotated to $(\boldsymbol{r}, \boldsymbol{\theta}, \boldsymbol{\phi})$-space in which CSEM is defined (Figure 4.3(c). The perturbations are applied to the elastic tensor in specific locations. We ignore small variations in the propagation direction and consider an estimated mean propagation direction. We have tested models in which maximum splitting

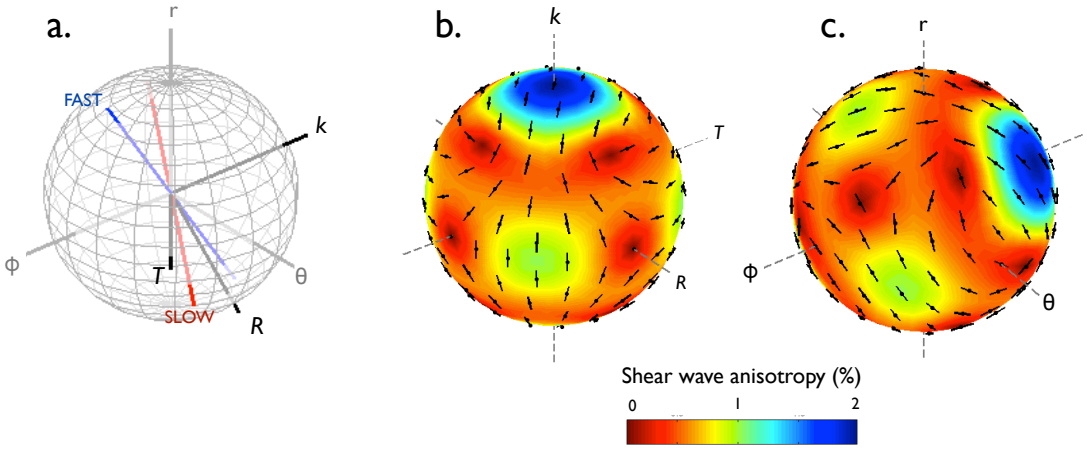

Figure 4.3: Panel a: Coordinate system for (R, T, k), in which the fast and slow axis are defined, and (r, ϕ, θ) in which CSEM is defined. Panels b and c: Percentage of splitting (in color) and fast axis direction (black bars) are shown as a function of propagation direction. These are the anisotropic perturbations represented in Model D; 2% splitting and $-45°$ fast axis. Panel b is in the (R, T, k) coordinate system, while panel c is rotated to the (r, ϕ, θ) coordinate system. [figure made with MSAT (Walker and Wookey, 2012)]

occurrs in the propagation direction and in the horizontal plane of the diffracted part of the ray path; however our preferred model results in maximum splitting for the slightly upward portion of the path in the last part of D″ sampled by S_{diff} on the station side.

4.3 Data

4.3.1 September 4th 1997, Fiji event

The data for this study come from a deep ($\sim$ 621 km, Mw 6.3, 09/04/97) event near the Fiji islands. The S_{diff} phases from this event are observed at the stations of the Kaapvaal array in Southern Africa (see map in Figure 4.4). The distance between the event and stations is $\sim 120°$, which is well within the shadow of the core. The radiation pattern and azimuthal range covered are shown in Figure 4.5; the azimuth range is non-nodal and the SH and SV components are expected to be of opposite polarity in all of our data.

This deep event was previously studied for its sensitivity of the SH_{diff} to the LLSVP boundary (Wen, 2001; To et al., 2005). To et al. (2005) pointed out the anomalous elliptical particle motions in S_{diff} outside the LLSVP and linear ones inside the LLSVP. This observation is the focus of this study. Unfortunately, while the Kaapvaal array was deployed, no other suitable nearby events occurred to confirm the observations made here.

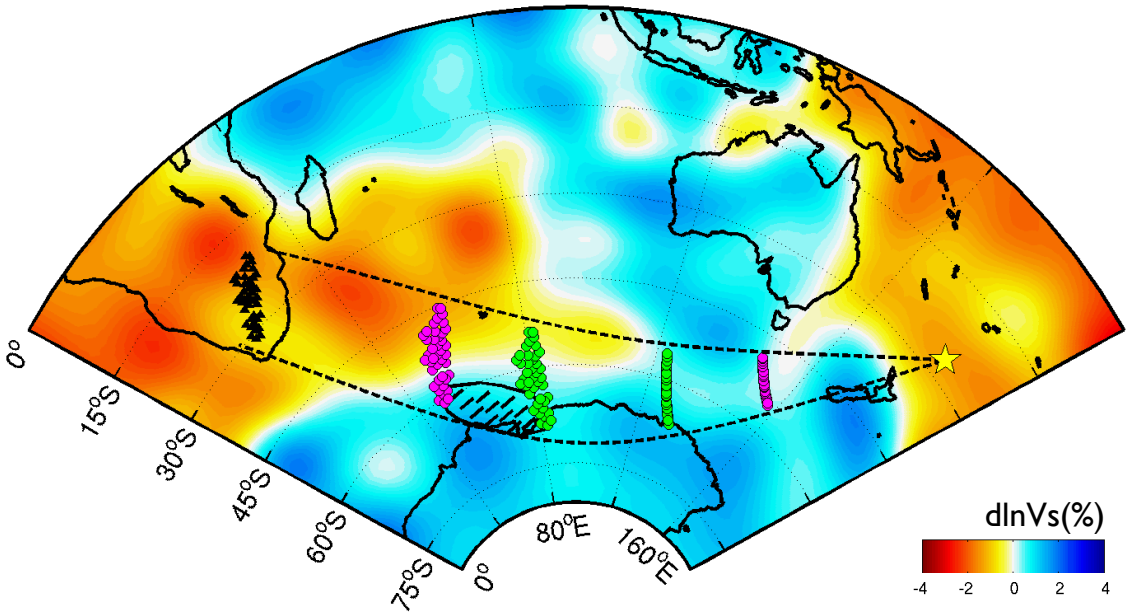

Figure 4.4: Ray path coverage for diffracted waves for the September 4th 1997 Fiji islands events (Mw 6.3, 621 km depth) observed at the Kaapvaal array in southern Africa. Piercing points for S_{diff} are plotted 90 km above (magenta) and at the core-mantle boundary (green). Background model is SAW24B16 (Mégnin and Romanowicz, 2000) at 2750 km depth.

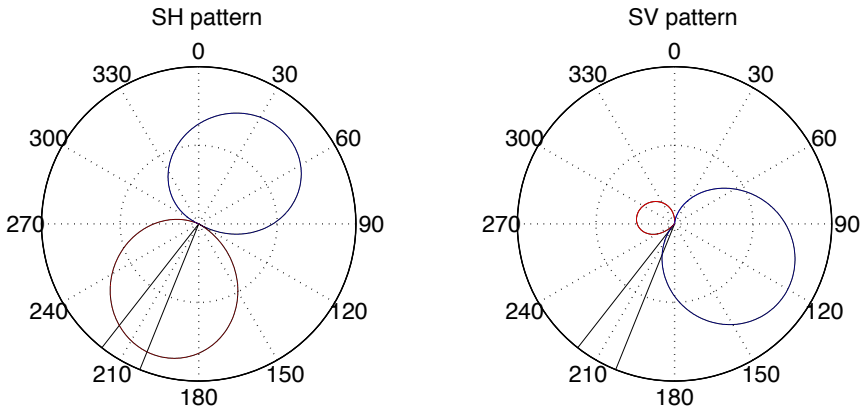

Figure 4.5: Source radiation pattern of S_{diff} waves for September 4th 1997 Fiji Islands event. Source polarity is indicated in blue (positive) and red (negative). Azimuths covered in this study are shown by the black solid lines.

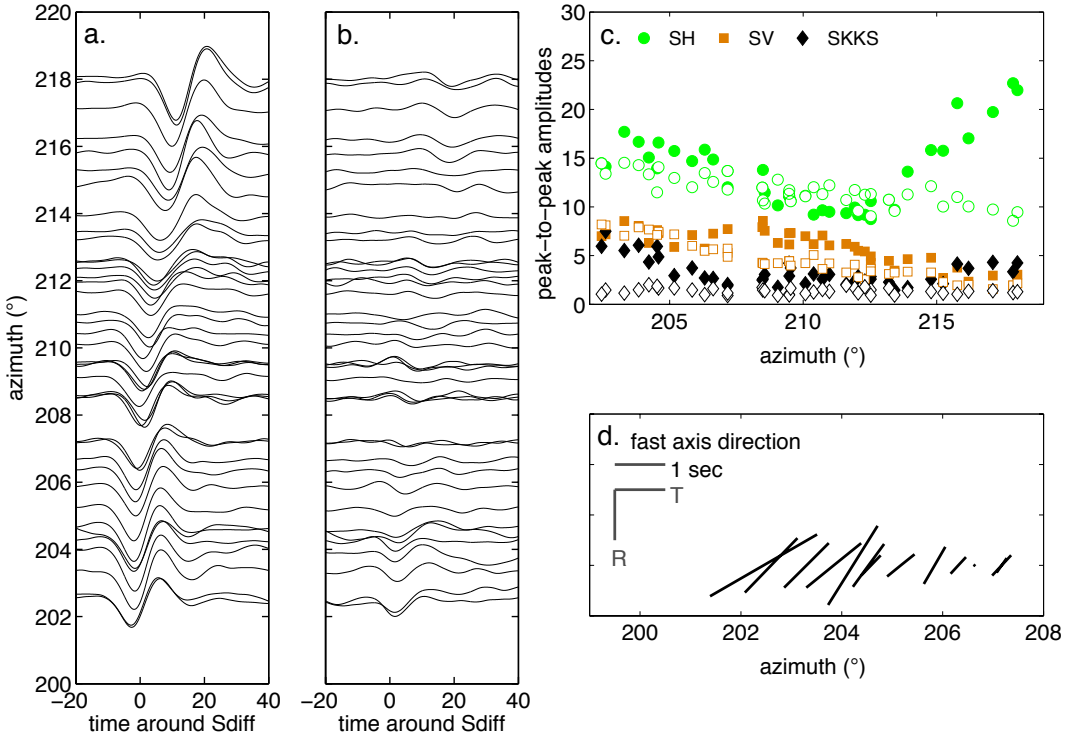

Figure 4.6: Data analysis for the September 4th 1997 Fiji Islands event. Panel a: Transverse component velocity waveforms around the S_{diff} arrival. Waveforms are filtered between 15 and 100s. Panel b: Same as panel a, but for the radial component. Panel c: Peak-to-peak amplitude measurements of observed phases (filled symbols) and PREM synthetics (open symbols) for SH_{diff} (green), SV_{diff} (black), and $SKKS$ (brown). Panel d: Fast axis direction for S_{diff} phases at smaller azimuths. The length of the lines is scaled to the amount of splitting. Splitting magnitude decreases strongly with azimuth.

4.3.2 Waveforms

S_{diff} waveforms for the transverse (SH) and radial (SV) waveforms are shown in the first two panels of Figure 4.6. These velocity waveforms are filtered between 15 and 100s. The isotropic velocity jump at the LLSVP boundary is visible in the strong delay occurring in the SH phase around an azimuth of 213° (Wen, 2001; To et al., 2005). At the same time, the waveforms show no evidence for smaller-scale ultra-low-velocity-zones at this boundary, as observations of S_{diff} have found elsewhere (Cottaar and Romanowicz, 2012).

The SV_{diff} component is a much smaller amplitude phase, but appears stronger at azimuths smaller than 206° and greater than 216°. The radiation patterns of SH and SV have opposite polarities in the direction of interest, which is clear in the waveforms at the larger azimuths; the SH and SV arrivals at stations located at small azimuths have the same

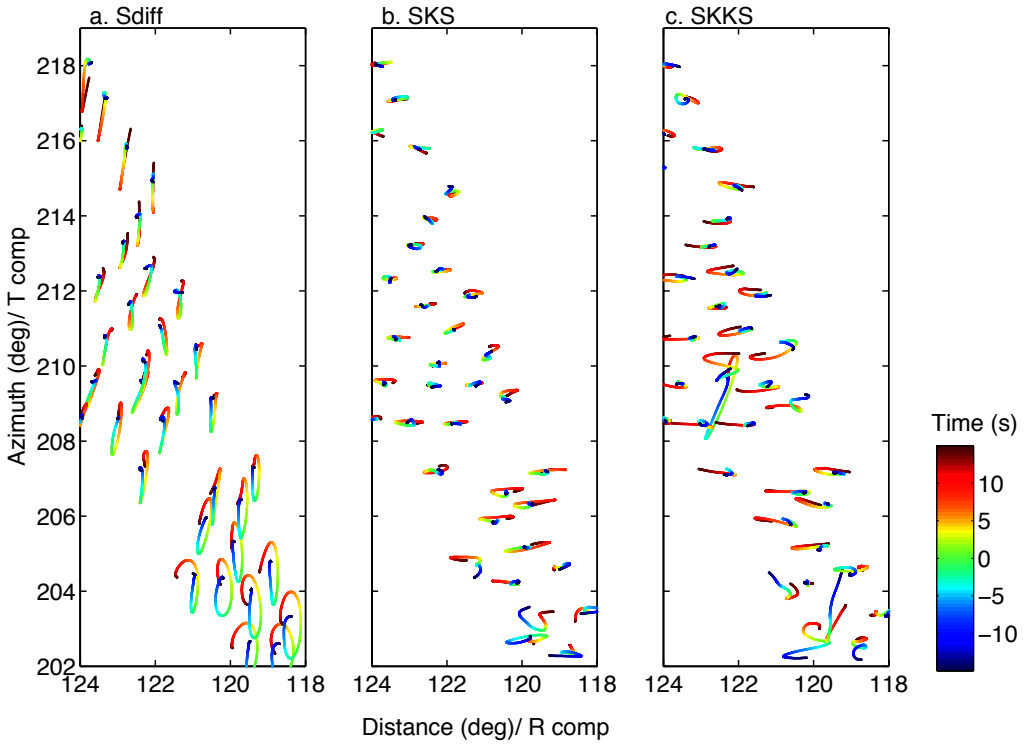

Figure 4.7: Particle motion for S_{diff} (a), SKS (b), and $SKKS$ (c). Data are filtered between 15-100s and windowed 30 seconds around the predicted arrival time for the phase. The particle motions are organized by distance and azimuth and the SH component deviations are plotted along the vertical axis and the SV component along the horizontal axis. Time runs from red to blue on a rainbow scale (see online color version). There is no correlation between the ellipticity seen in S_{diff} and in the other two phases.

polarity, suggesting that the SV energy is not the direct SV arrival from the source.

Particle motions are shown as a function of azimuth and distance in Figure 4.7(a). The data shows elliptical clockwise particle motions at smaller azimuths and more linear particle motions towards the boundary and inside the LLSVP. Note that the data coverage includes a trend of increasing distance with increasing azimuth.

Figure 4.7(b) and (c) show the particle motions of core phases SKS and $SKKS$ for the same event. These phases have similar paths as S_{diff} in the upper mantle, but short, near-vertical paths in D$''$ within the African LLSVP. The amount of ellipticity in these phases appears scattered, and is different from the trend with azimuth observed for the S_{diff}. Silver et al. (2001) and Adam and Lebedev (2012) report SKS splitting and surface wave azimuthal anisotropy, respectively, across the Kaapvaal array. The measured fast axis trends NNE-SSW in the south, towards ENE-WSW in the center and then back to NNE-SSW in the north and the splitting time delay is roughly constant, with little variation in

the amount of splitting. This trend is different from what we see in the diffracted data. We therefore conclude that the cause of the elliptical particle motions in S_{diff} lies primarily in the lowermost mantle.

4.3.3 Amplitudes

The relative peak-to-peak amplitudes for S_{diff} and the transverse and radial component and $SKKS$ on the radial component are measured in the observed waveforms and synthetics for PREM (Dziewonski and Anderson, 1981). Results are shown in Figure 4.6(c). SH_{diff} (green circles) is the strongest phase. According to the radiation pattern and PREM synthetics, its amplitude should gradually decrease towards larger azimuths. In the observed data, however, strong amplitudes are seen at larger azimuths (and larger distances) due to the lower velocities in the LLSVP.

SV_{diff} (black diamonds) is the weakest phase overall, both in the observed and synthetic waveforms; the observed amplitudes appear to increase towards the smallest azimuths and again slightly at the largest azimuths. The increased amplitude at both ends of the azimuth range differs from the amplitude predictions for PREM. For comparison, $SKKS$ amplitudes (magenta squares) are plotted. $SKKS$ originates as SV energy at the source, and its take-off angle is close to that of SV_{diff}. The $SKKS$ phase, however, does not show the same trend as SV_{diff} compared to the PREM predictions, as was already observed in the particle motions, which is an additional argument in favor of a D$''$ source for the observed S_{diff} anomalies.

The strong energy on the SV component, at large azimuths, is associated with linear particle motions (Figure 4.7(a)) in contrast to the elliptical particle motions at small azimuths. We will argue that this energy is not an SV_{diff} phase, but an SH_{diff} arriving out of plane, due to refraction at the LLSVP boundary.

4.3.4 Shear wave splitting results

We quantify the type of anisotropy by measuring the fast axis ϕ and splitting time dt with the rotation-correlation method of (Bowman and Ando, 1987) (see Section 4.2.1). We define the fast axis in the R-T plane , as opposed to N-E; the latter would assume the anisotropy to be in the horizontal plane (purely azimuthal anisotropy). The fast axis ϕ is defined as 0° in the transverse direction and positive in the clockwise direction towards the radial direction (looking towards the station, Figure 4.2). The orientation of the anisotropy detected here will depend on where along the path the anisotropy occurs. The shear waveforms are sensitive to any anisotropy in the plane orthogonal to the direction of propagation. For the shear wave splitting measurements, the data are filtered between 10 and 30s.

Remarkably, as reported in (To et al., 2005), significant splitting only occurs at sta-

tions for azimuths less than 208°. The fast axis directions observed here are plotted in Figure 4.6(d). The average fast axis direction of these splitting results, weighted by their splitting times, is -46° from the T component. Although the quadrant of the fast axis is well constrained, we will later see from the synthetics that there is a great uncertainty in determining the exact fast axis. The length of the bars is scaled to the amount of splitting that occurs. There is a strong decrease in the amount of splitting as well as a slight rotation in the fast axis direction with increasing azimuths.

We do not attempt to correct the splitting in S_{diff} for upper mantle effects using the splitting in SKS and $SKKS$ as a reference. One reason is that the S_{diff} and SKS paths are different in the upper mantle, and their polarizations are orthogonal; a number of assumptions on a simplified anisotropy model would be required to make these corrections, with the risk of introducing artificial splitting. Most importantly, the measured splitting of SKS and $SKKS$ for this event is negligibly small and corrections should not change the main trends observed in the data.

4.4 Results

4.4.1 Excluding isotropic and transverse isotropic models

Initially, we implemented only isotropic velocity variations. Figure 4.8 shows a comparison of the observed particle motions versus synthetics for PREM, and synthetics for a saturated version of SAW24B16 (To et al., 2005). Neither isotropic model reproduces the elliptical particle motions at the smaller azimuths. In contrast to those for the 1D model PREM, the particle motions for the saturated model capture the travel time variations due to the LLSVP (seen by the change in color of the particle motions with azimuth). It also shows some interesting behavior for the phases that sense the LLSVP boundary around azimuths of 212-216°. It reproduces the decrease in amplitude and the production of strong postcursors (To et al., 2005). At azimuths around 215°, the co-arrival of the main phases and postcursors results in an apparent elliptical particle motion. This interference is not present in the real data where the postcursor appears as a separate phase with a larger travel time delay at slightly smaller azimuths (see Figure 4.6). These postcursors fall outside the time window for the determination of the particle motions. We will, however, find them in the synthetic waveforms for our best model in Figure 4.11. The difference in behavior of the postcursors between the observations and synthetics could be due to the lateral sharpness of the isotropic velocity jump, or to the exact shape of the LLSVP boundary. We refrain from modeling the postcursors more precisely here (see also To et al. (2005)).

All the stations are located at distances larger than 118°. These are far within the core shadow of direct shear wave arrivals, and SV_{diff} energy is not expected to propagate that far along the CMB (see Figure 4.1). As expected, synthetic particle motions in Figure 4.7 show no SV_{diff} arrival for PREM (panel b) or for a saturated isotropic model (panel c).

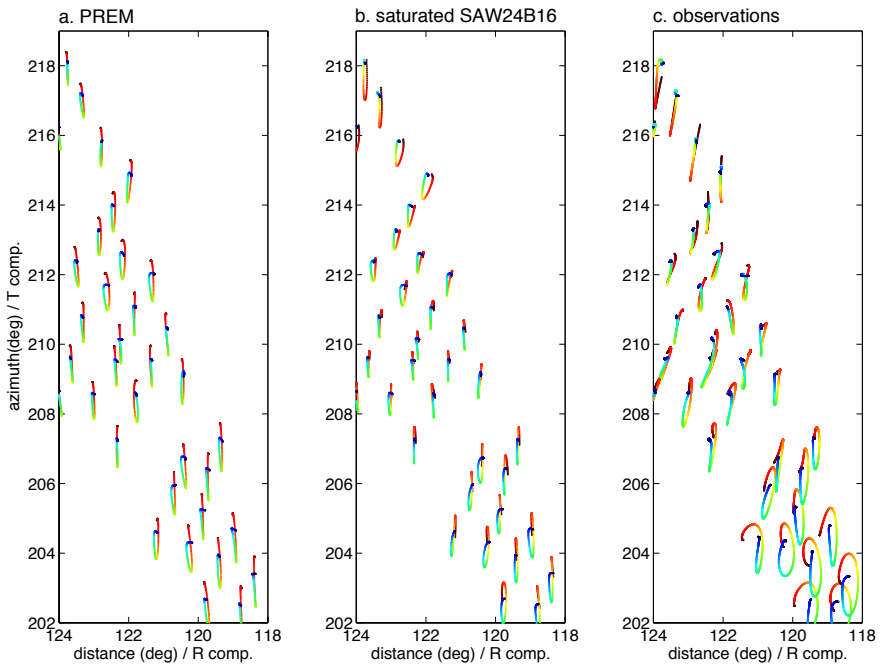

Figure 4.8: Particle motion plots. Both synthetic (a,b) and observed data (c) represented here are filtered between 15 and 100s. Panel a. shows the particle motions for PREM and panel b. for SAW24B16, where the slow LLSVP is saturated at -2.75% and the fast region at +1.00% (comparable to the model found by To et al. 2005). Panel c shows the observed data. The time range runs from 15 s before to 15 s after the predicted time arrival (from blue to red in the colored version, color bar is shown in Figure 4.7). Both isotropic models result in nearly linear particle motions.

To propagate SV diffracted energy over larger distances along the CMB, the velocity model needs to be slower than PREM. The strong SV_{diff} arrivals observed are, however, for paths outside the African LLSVP, where the shear velocity is faster than average in D″. We attempted to model the strong SV_{diff} arrivals at large distances by introducing radial anisotropy with SV velocity slower than SH velocity. The blue synthetics in Figure 4.1 are for such a model. They show that the integrated travel time difference between the SH and SV become significant; at larger distances the two phases become more than a wavelength apart. As there is no overlap between the two phases, they do not result in an elliptical particle motion.

More complex anisotropy in the lowermost mantle can cause splitting of SH_{diff} and elliptical particle motions at large distances in the core shadow. In the following sections, we model the constraints on the nature of the anisotropy, insofar as our data can constrain this.

4.4.2 Anisotropic models

We first note that we constrain the anisotropy to the part of D″ where the phase turns up towards the station. We attempted to introduce anisotropy in the diffracted part of the path, but the coupling between the SH and SV component, and the subsequent loss of amplitude due to the coupling between the SH and SV components and the SV component with the outer core, leads to overall smaller amplitudes in the synthetics. We do not observe decreased amplitudes in the observations. The opposite is true: for the smaller azimuths, both the SH and SV components have stronger amplitudes than predicted for PREM (see Figure 4.6(b)).

We present several models with anisotropy added to the saturated isotropic model. The anisotropy is confined to the faster-than-average region outside the African LLSVP. The resulting particle motions are plotted in Figure 4.9. The model parameters are summarized in Table 4.1.

Model A performs well with anisotropy defined as purely azimuthal anisotropy in the horizontal plane. For purely azimuthal anisotropy, the strongest splitting occurs for a vertically propagating S wave. The fast axis is N-S and the slow axis E-W; the two differ in S velocity by 10%. This model of anisotropy produces particle motions that are comparable to those observed. If the fast axis is rotated by $\sim 45^\circ$ in either direction in the horizontal plane, the polarity of the particle motion switches sign. This model illustrates that a fitting solution can be found with anisotropy defined in any plane. In this case, where anisotropy defined in the horizontal plane, correct splitting along the direction of propagation is obtained for our dataset. We call this the apparent splitting of the anisotropy model. The maximum splitting will always occur for S waves propagating orthogonal to the plane in which the azimuthal anisotropy is defined (as long as its polarization is not parallel to the fast or slow axis). The apparent anisotropic splitting for S waves propagating in other directions will always be less.

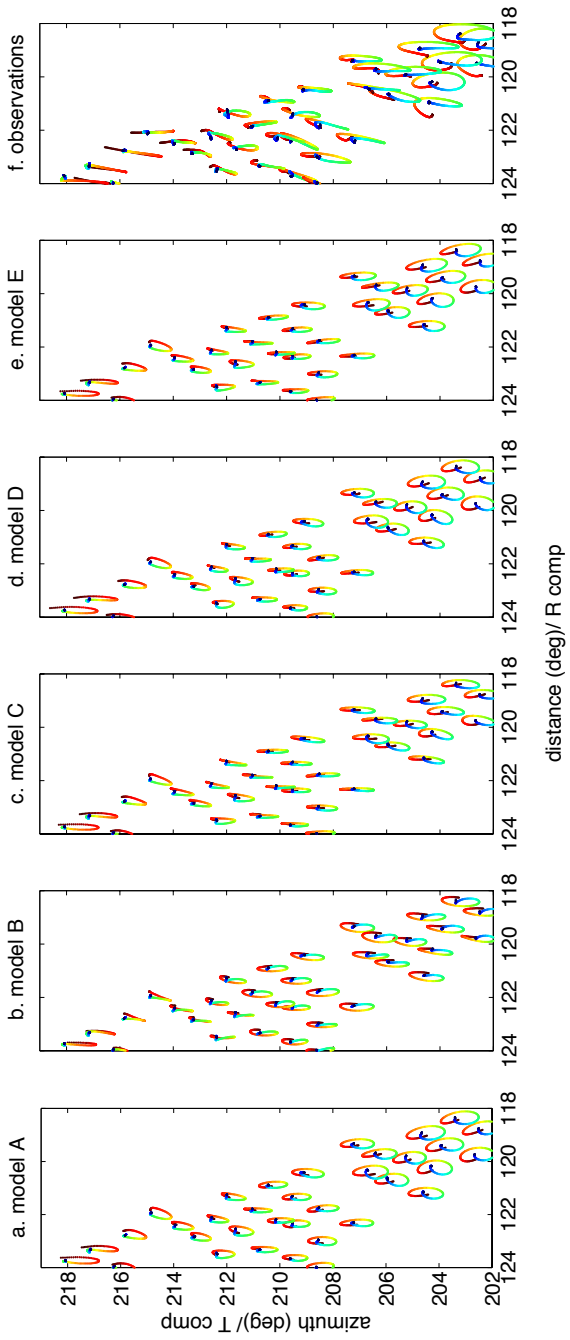

Figure 4.9: Particle motion plots for synthetic models including anisotropy. Model A includes purely azimuthal anisotropy with a fast N-S axis. Models B-E include anisotropy orthogonal to the direction of propagation, with fast axis directions of +45, -65, -45 an -25°, respectively. Observed particle motions are shown in panel f. Time increases from blue to red (see color bar in Figure 4.7)

Model	fast axis	perc. of splitting	radial extent	lateral constraint	measured ϕ	measured dt
A	0° (azimuth)	10%	370 km	$dlnV > 0\%$	$-35°$	2.3 s
B	45°	4%	370 km	$dlnV > 0\%$	48°	1.3 s
C	$-65°$	4%	370 km	$dlnV > 0\%$	$-43°$	1.28 s
D	$-45°$	4%	370 km	$dlnV > 0\%$	$-37°$	2.3 s
E	$-25°$	4%	370 km	$dlnV > 0\%$	$-44°$	1.6 s
D1	$-45°$	8%	100 km	$dlnV > 0\%$	$-46°$	1.4 s
D2	$-45°$	8%	150 km	$dlnV > 0\%$	$-36°$	1.7 s
D3	$-45°$	8%	200 km	$dlnV > 0\%$	$-29°$	2.6 s
D4	$-45°$	8%	150 km	$dlnV > 1.0\%$	$-45°$	0.65 s
D5	$-45°$	8%	150 km	$dlnV > 0.5\%$	$-44°$	1.0 s

Table 4.1: Selected anisotropy models. Fast axis, strength of anisotropy and their radial and lateral extent are listed. Model A is an exception as its fast and slow axis are defined in the horizontal plane as opposed to the plane orthogonal to the direction of propagation in the data. The shear wave splitting results are for stations at azimuths smaller than 208°. ϕ is the measured fast axis weighted by its splitting time dt.

We continue with models that have anisotropy variations defined in the plane orthogonal to the direction of propagation (panel a and b in Figure 4.3). In this case the maximum anisotropy in the tensor and the apparent anisotropy along the direction of propagation will be the same and we do not assume anything about the rest of the elastic tensor. This captures the part of the anisotropic tensor that is constrained by our data set; it is unlikely to be the true, complete anisotropic tensor. The perturbations in the elastic tensor are then rotated to the coordinate system in CSEM (Figure 4.3(c)) before applying them on top of the saturated isotropic model.

We estimate a suitable propagation direction from the azimuth and incidence angle of the diffracted waveforms at 100 km above the CMB, as they turn up towards the stations. This results in an azimuth of 310° and an upward angle of 30°. Models B through E all have a fast and slow axis defined in the plane orthogonal to this direction. The four models have fast axis directions of +45, -65, -45 and -25°, respectively. All models have 4% velocity difference between the fast and the slow axis. Our shear wave splitting measurements suggest a mean fast axis direction of -46° in the plane considered.

Model B has a fast axis of +45°. This model, as can be expected, produces particle motions that are opposite from those observed. Models C and E are presented to illustrate the change in waveforms with a shift of 20° in fast axis direction. Model D, with a fast axis at -45° is the best model in terms of the orientation of the particle motions. This result is consistent with the shear wave splitting measurements. The particle motions only differ slightly. From the shear wave splitting measurements, listed in Table 4.1, we find that it is hard to distinguish between models with slight differences in fast axis. This shows the limitations of the methods. When comparing the particle motions, Model D performs best.

4.4.3 Lateral and Radial Constraints

So far we have constrained the anisotropy to the lowermost 370 km and to the fast region outside the LLSVP. Here we investigate further constraints on the lateral and radial extent of the anisotropy. We keep the fast axis fixed at -45°.

So far the models had 4% velocity difference between the fast and slow axis over the entire 370 km thickness of the layer. In Models D1–D3 (Figure 4.10), we vary the extent of the anisotropic layer in the radial direction above the core-mantle-boundary. These models extend over 100 (D1), 150 (D2) and 200 km (D3) with 8% anisotropic strength. From the ellipticity of the particle motions and the mean measured splitting times (in Table 4.1), one can see an increase of splitting time with thickness of the anisotropic layer. These examples illustrate the trade-off between thickness and the strength of anisotropy, and the difficulty to constrain both.

In models D1-D3, the splitting extends to larger azimuths than in the data. This suggests that the anisotropy does not extend with the same strength as far towards the LLSVP boundary as implemented in the model. Models D4 and D5 constrain the anisotropy laterally to the region in which the isotropic shear wave deviation from PREM is >1.0% and 0.5%, respectively. Model D5 does the best job in capturing the azimuthal extent of the splitting in the observations.

4.4.4 Preferred Model

Our preferred model, D5, captures many of the features seen in the data. Figure 4.11 shows the waveforms, amplitudes, and measured fast axis direction and magnitude. These can be directly compared to the same analysis on the observed data shown in Figure 4.6.

The fast axis direction, as well as the decrease in splitting time with azimuth, are well reproduced by this model. This can also be seen in the strength and polarity of the SV component at smaller azimuths. Postcursors are also generated on the SH component at intermediate azimuths. This feature is stronger in synthetics than in the observations.

There are two aspects of the observations that our model does not capture. One is that the SH component at smaller azimuths is stronger in the observations than predicted by this synthetic model or by PREM (Figure 4.8(a)). This could be a source effect. A stronger SH component would also lead to a stronger SV component after splitting. The other is that the polarity of the energy on the SV component at large azimuths is opposite to that in the observations. This means the rotation or the backazimuth of the SH_{diff} arrival is opposite in the synthetics as compared to the observations. As these rotations are caused by refraction at the LLSVP boundary, fixing the polarity would require more detailed modeling of the specific shape of the LLSVP boundary, which is beyond the scope of this study.

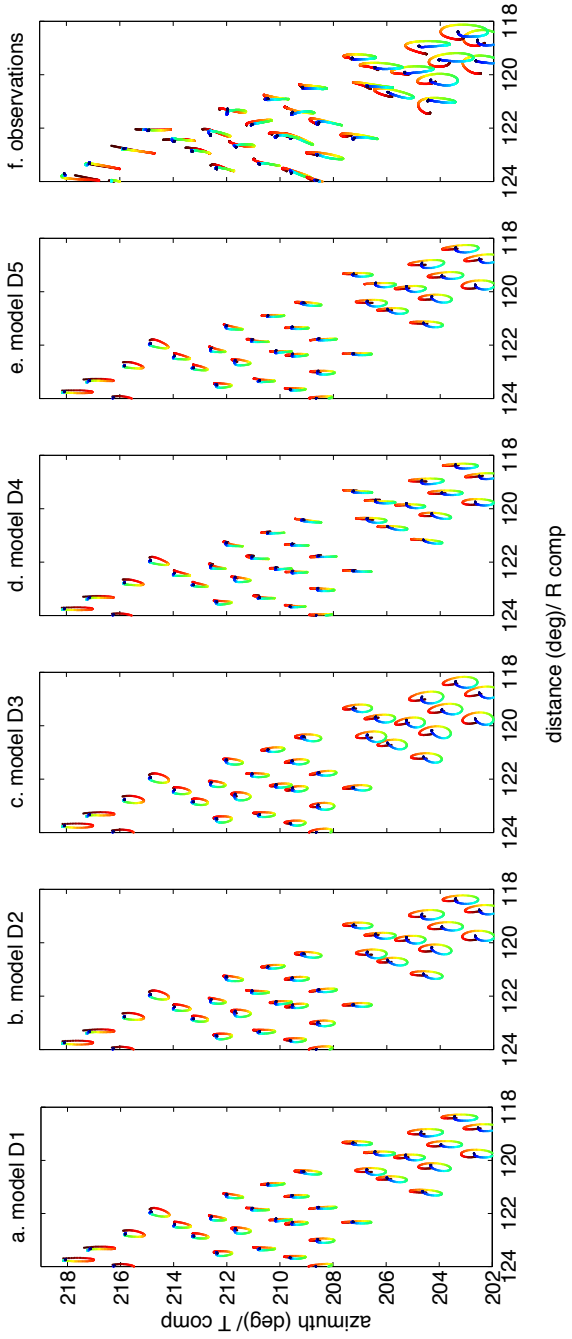

Figure 4.10: Particle motion plots for models with anisotropy confined in the lateral and radial direction. All models have a fast axis direction of -45°. Model D1-3 include 8% of anisotropy over 100, 150 and 200 km, respectively, above the core-mantle boundary. Models D4-5 have fixed anisotropy of 8% over 150 km, but confine the anisotropy laterally to the region where $dlnV$ is greater than 1.0% (D4) and greater than 0.5% (D5). Observed particle motions are shown in panel f. Time increases from blue to red (see color bar in Figure 4.7)

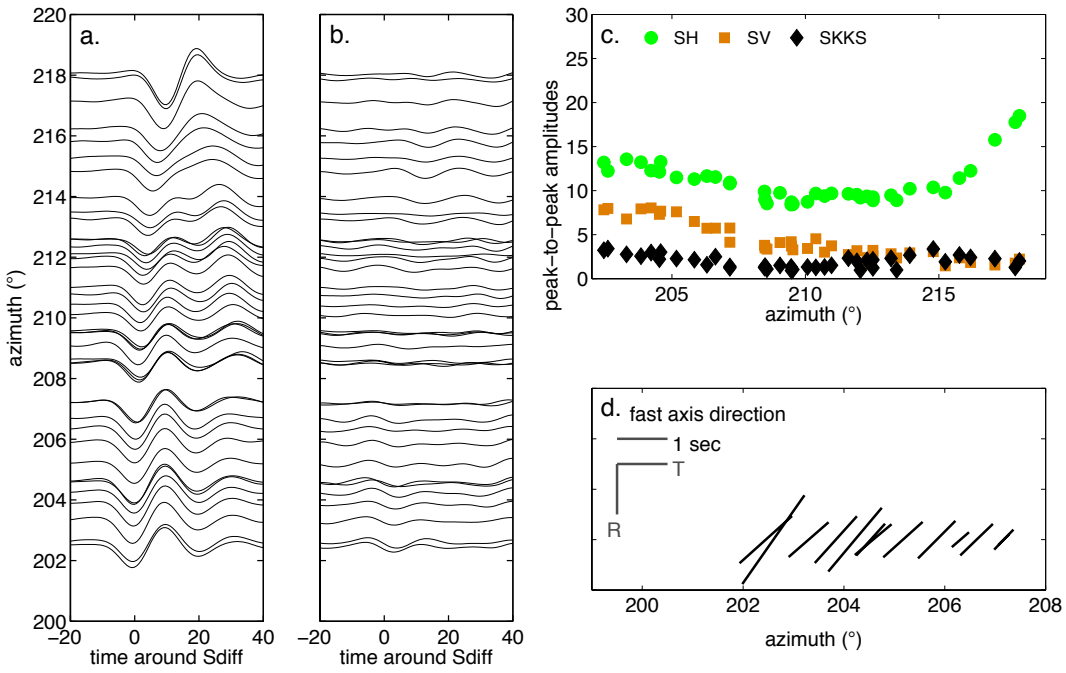

Figure 4.11: Synthetic data analysis for our preferred model– D5. Panel a: Transverse component velocity waveforms around the S_{diff} arrival. Synthetic waveforms are filtered between 15 and 100s. Panel b: Same as panel a, but for the radial component. Panel c: Peak-to-peak amplitude measurements of synthetic phases for SH_{diff} (green), SV_{diff} (black), and $SKKS$ (magenta). Panel d: Fast axis direction in the synthetic data at smaller azimuths. The length of the lines is scaled to the amount of splitting.

4.5 Discussion and Conclusions

One possible cause of azimuthal anisotropy in the lowermost mantle is shape-preferred orientation (SPO) due to layering or aligned inclusions (Kendall and Silver, 1998). Hall et al. (2004) measure anisotropic strength in various scenarios, to explain observed SK(K)S splitting. They find that low-velocity inclusions such as melt, are more effective at creating azimuthal anisotropy than solid, fast inclusions. Melt inclusions, however, are more likely within the LLSVP than in the fast region, where we observe anisotropy, as such inclusions should lower the overall average shear wave velocity.

A second option is the alignment of intrinsically anisotropic minerals i.e. lattice preferred orientation (LPO), the common explanation for azimuthal anisotropy in the upper mantle. LPO becomes more likely in regions where strong deformation is currently occurring or previously deformed material is present, i.e. fossilized anisotropy. Azimuthal anisotropy has generally been observed within the ring of fast velocities at the base of the mantle; i.e. locations that are more likely to include slab remnants (e.g. Rokosky et al., 2006; Long, 2009; Nowacki et al., 2011). Geodynamical modeling constrained by past plate tectonics shows that there could be slab remnants in the region studied beneath the Indian/Antarctic Ocean, resulting from subduction that ceased 80 Ma ago (Steinberger and Torsvik, 2012). Either fossil LPO anisotropy within the slab or dislocation creep deformation from the large strains generated as the slab material rotates onto the CMB could cause preferred orientation within the slab material.

What mineral assemblages within the slab would cause the significant azimuthal anisotropy documented here? The single crystal shear wave azimuthal anisotropy is roughly twice as strong in postperovskite (pPv) as in perovskite (Pv) (Iitaka et al., 2004; Tsuchiya et al., 2004). In the next chapter we will see that pPv with slip along the (001) plane creates the strongest azimuthal anisotropy. We will also see that the fast direction in pPv is somewhat rotated from the direction of flow, while pv's fast axis is parallel to flow. The occurrence of pPv in D″ would also be more likely in faster than average, colder regions. Both Pv and pPv would also cause strong, and opposite signatures in radial anisotropy (Wenk et al., 2011; Walker et al., 2011).

Global models of radial anisotropy (Panning and Romanowicz, 2006; Kustowski et al., 2008) do not indicate a strong signature in our area of study, although the data coverage in this region is far from ideal. The decrease in strength of anisotropy towards the LLSVP boundary could mean that the slab material— and with that the fast direction— is rotating to a plane to which our data has no sensitivity (Figure 4.12). Our dataset would also lose its sensitivity to azimuthal anisotropy, if the fast axis rotates upward to a purely transverse isotropic model; as the fast axis will be orthogonal to the polarization of the SH phase. Rotation by material flow could happen if the boundary is a mechanical boundary, possibly due to compositionally distinct LLSVPs. Wang and Wen (2007) find patterns of complex azimuthal anisotropy near the African LLSVP from differential SK(K)S splitting, showing further evidence for complex flow patterns outside this structure.

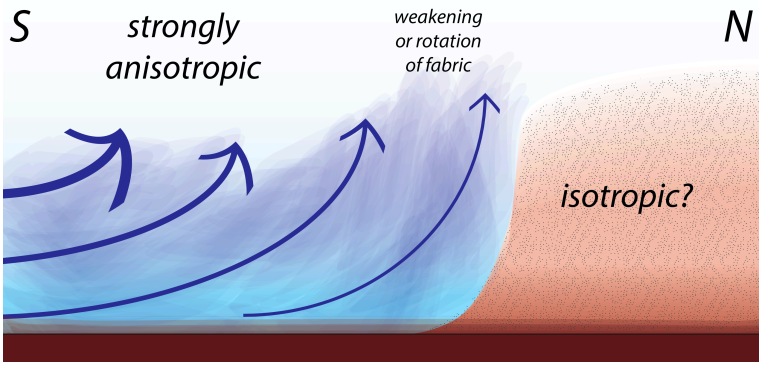

Figure 4.12: Cartoon cross-section from south to north through the edge of the African LLSVP. Possible flow outside the LLSVP as suggested by the observed anisotropy.

In our dataset there is no apparent anisotropy within the LLSVP. Either our dataset has no resolution to the anisotropy present, or the convection in the LLSVP is too weak, too small-scaled, or the material's intrinsic anisotropy is too weak.

We have constrained a patch of strong tilted anisotropy south of the African LLSVP from observations of shear-diffracted phases at large distances. The fast axis of the anisotropy is tilted to the north away from the direction of propagation to the northwest. The azimuthal anisotropy decreases in strength or rotates towards the boundary of the LLSVP. No anisotropy is observed within the LLSVP. The occurrence of pPv in slab remnants is consistent with the fast velocities and strong azimuthal anisotropy, while a compositionally distinct LLSVP is likely to affect flow patterns near its border.

4.6 Acknowledgements

The data for this project came from IRIS (www.iris.edu). We thank Yann Capdeville for providing the CSEM code which produced the synthetic data in this study. Shear wave measurements are done with help of the SplitLab Matlab package (www.gm.univ-montp2.fr/splitting/). Figure 4.3 is produced with the MSAT Matlab package (www1.gly.bris.ac.uk/MSAT/ This work was supported by NSF/CSEDI grant 1067513 and ERC grant 'WAVETOMO'.

4.7 Appendices

Bibliography

Adam, J., Lebedev, S., 2012. Azimuthal anisotropy beneath southern Africa from very broad-band surface-wave dispersion measurements. Geophys. J. Int. 191 (1), 155–174.

Bowman, J. R., Ando, M., Jan. 1987. Shear-wave splitting in the upper-mantle wedge above the Tonga subduction zone. Geophys. J. Int. 88 (1), 25–41.

Capdeville, Y., Larmat, C., Vilotte, J. P., Montagner, J. P., 2002. A new coupled spectral element and modal solution method for global seismology- A first application to the scattering induced by a plume-like anomaly. Geophys. Res. Lett. 29, 1318–1322.

Capdeville, Y., To, A., Romanowicz, B., 2003. Coupling spectral elements and modes in a spherical Earth: an extension to the 'sandwich' case. Geophys. J. Int. 154 (1), 44–57.

Cottaar, S., Romanowicz, B., 2012. An unsually large ULVZ at the base of the mantle near Hawaii. Earth Plan. Sci. Lett. 355, 213–222.

Crampin, S., 1984. Effective anisotropic elastic constants for wave propagation through cracked solids. Geophys. J. Int. 76 (1), 135–145.

Doornbos, D., Mondt, J., 1980. The interaction of elastic waves with a solid-liquid interface, with applications to the core-mantle boundary. Pure Appl. Geophys. 118 (2), 1293–1309.

Dziewonski, A. M., Anderson, D. L., 1981. Preliminary reference Earth model. Phys. Earth Plan. Int. 25 (4), 297–356.

Garnero, E., Lay, T., 1997. Lateral variations in lowermost mantle shear wave anisotropy. J. Geophys. Res 102, 8121–8135.

Garnero, E., Maupin, V., Lay, T., Fouch, M., 2004. Variable azimuthal anisotropy in Earth's lowermost mantle. Science 306 (5694), 259–261.

Garnero, E. J., McNamara, A. K., 2008. Structure and dynamics of Earth's lower mantle. Science 320 (5876), 626.

Hall, S., Kendall, J., van der Baan, M., 2004. Some comments on the effects of lower-mantle anisotropy on SKS and SKKS phases. Phys. Earth Plan. Int. 146 (3-4), 469–481.

Iitaka, T., Hirose, K., Kawamura, K., Murakami, M., 2004. The elasticity of the MgSiO3 post-perovskite phase in the Earth's lowermost mantle. Nature 430 (6998), 442–445.

Karato, S., 1998a. Seismic anisotropy in the deep mantle, boundary layers and the geometry of mantle convection. Pure Appl. Geophys. 151 (2-4), 565–587.

Karato, S., 1998b. Some remarks on the origin of seismic anisotropy in the D" layer. Earth Planets and Space 50, 1019–1028.

Karato, S., Jung, H., Katayama, I., Skemer, P., 2008. Geodynamic significance of seismic anisotropy of the upper mantle: new insights from laboratory studies. Annu. Rev. Earth Planet. Sci. 36, 59–95.

Kawai, K., Geller, R. R. J., Aug. 2010. The vertical flow in the lowermost mantle beneath the Pacific from inversion of seismic waveforms for anisotropic structure. Earth Plan. Sci. Lett. 297 (1-2), 190–198.

Kendall, J., Silver, P., 1998. Investigating causes of D" anistropy. Geodynamics Series 28, 97–118.

Komatitsch, D., Vinnik, L. P., Chevrot, S., Jul. 2010. SHdiff-SVdiff splitting in an isotropic Earth. J. Geophys. Res. 115 (B7), 1–13.

Kustowski, B., Ekström, G., Dziewoski, A., 2008. Anisotropic shear-wave velocity structure of the Earth's mantle: a global model. J. Geophys. Res. 113 (B6), B06306.

Lekic, V., Cottaar, S., Dziewonski, A. M., Romanowicz, B., 2012. Cluster analysis of global lower mantle tomography: A new class of structure and implications for chemical heterogeneity. Earth Plan. Sci. Lett. 357-358, 68–77.

Long, M. D., Jun. 2009. Complex anisotropy in D" beneath the eastern Pacific from SKS-SKKS splitting discrepancies. Earth Plan. Sci. Lett. 283 (1-4), 181–189.

Loubet, N., Ribe, N., Gamblin, Y., 2009. Deformation modes of subducted lithosphere at the core-mantle boundary: An experimental investigation. Geochem. Geophys. Geosyst 10 (10), Q10004.

Lynner, C., Long, M., 2012. Evaluating Contributions to SK(K)S Splitting from Lower Mantle Anisotropy: A Case Study from Station DBIC, Côte D'Ivoire. B Seismol. Soc. Am.

Mainprice, D., Barruol, G., Ismail, W., 2000. The seismic anisotropy of the Earth's mantle: from single crystal to polycrystal. In: Geophysical Monograph Series. Vol. 117. AGU, pp. 237–264.

Maupin, V., 2005. Azimuthal anisotropy in the D" layer beneath the Caribbean. J. Geophys. Res. 110 (B8), 1–20.

McNamara, A. A. K., Karato, S. S.-I., van Keken, P., van Keken, P. E., Aug. 2001. Localization of dislocation creep in the lower mantle: implications for the origin of seismic anisotropy. Earth Plan. Sci. Lett. 191 (1-2), 85–99.

McNamara, A. K., Zhong, S., 2005. Thermochemical structures beneath Africa and the Pacific Ocean. Nature 7062, 1136–1139.

Mégnin, C., Romanowicz, B., 2000. The three-dimensional shear velocity structure of the mantle from the inversion of body, surface and higher-mode waveforms. Geophys. J. Int. 143 (3), 709–728.

Miyagi, L., Kanitpanyacharoen, W., Stackhouse, S., Militzer, B., Wenk, H.-R., 2011. The enigma of post-perovskite anisotropy: deformation versus transformation textures. Physics and Chemistry 38 (9), 665–678.

Montagner, J., 1998. Where can seismic anisotropy be detected in the Earth's mantle? In boundary layers. Pure Appl. Geophys. 151 (2-4), 223–256.

Morelli, A., Dziewonski, A. M., Woodhouse, J. H., 1986. Anisotropy of the inner core inferred from PKIKP travel times. Geophys. Res. Lett. 13 (13), 1545–1548.

Mosca, I., Cobden, L., Deuss, A., Ritsema, J., Trampert, J., 2012. Seismic and mineralogical structures of the lower mantle from probabilistic tomography. J. Geophys. Res. 117, B06304.

Niu, F., Perez, A., 2004. Seismic anisotropy in the lower mantle: a comparison of waveform splitting of SKS and SKKS. Geophys. Res. Lett. 31, L24612.

Nowacki, A., Wookey, J., Kendall, J., 2010. Deformation of the lowermost mantle from seismic anisotropy. Nature 467 (7319), 1091–1094.

Nowacki, A., Wookey, J., Kendall, J.-M. J., Oct. 2011. New advances in using seismic anisotropy, mineral physics and geodynamics to understand deformation in the lowermost mantle. J. Geodyn. 52 (3-4), 205–228.

Panning, M., Romanowicz, B., 2006. A three-dimensional radially anisotropic model of shear velocity in the whole mantle. Geophys. J. Int. 167 (1), 361–379.

Restivo, A., Helffrich, G., 2006. Coremantle boundary structure investigated using SKS and SKKS polarization anomalies. Geophys. J. Int.

Rokosky, J. M., Lay, T., Garnero, E. J., Aug. 2006. Small-scale lateral variations in azimuthally anisotropic D" structure beneath the Cocos Plate. Earth Plan. Sci. Lett. 248 (1-2), 411–425.

Silver, P., Chan, W., 1991. Shear wave splitting and subcontinental mantle deformation. J. Geophys. Res 96 (16), 429–16.

Silver, P., Gao, S., Liu, K., 2001. Mantle deformation beneath southern Africa. Geophys. Res. Lett. 28 (13), 2493–2496.

Stackhouse, S., Brodholt, J. P., Wookey, J., Kendall, J.-M., Price, G. D., Jan. 2005. The effect of temperature on the seismic anisotropy of the perovskite and post-perovskite polymorphs of MgSiO3. Earth Plan. Sci. Lett. 230 (1-2), 1–10.

Steinberger, B., Torsvik, T. H., 2012. A geodynamic model of plumes from the margins of Large Low Shear Velocity Provinces. Geochem. Geophys. Geosyst. 13, Q01W09.

Teng, T.-L., Richards, P., 1976. Diffracted P, SV and SH waves and their shadow boundary shifts. J. Geophys. Res. 74 (6), 1537–1555.

Thomas, C., Wookey, J., Simpson, M., 2007. D" anisotropy beneath Southeast Asia. Geophys. Res. Lett 34 (4), L04301.

To, A., Romanowicz, B., Capdeville, Y., Takeuchi, N., 2005. 3D effects of sharp boundaries at the borders of the African and Pacific Superplumes: Observation and modeling. Earth Plan. Sci. Lett. 233 (1-2), 1447–1460.

Trampert, J., van Heijst, H., 2002. Global azimuthal anisotropy in the transition zone. Science 296 (5571), 1297–1299.

Tsuchiya, T., Tsuchiya, J., Umernote, K., Wentzcovitch, R., 2004. Phase transition in MgSiO 3 perovskite in the Earth's lower mantle. Earth Plan. Sci. Lett. 224 (3), 241–248.

Vinnik, L., Farra, V., Romanowicz, B., 1989. Observational evidence for diffracted SV in the shadow of the Earth's core. Geophys. Res. Lett. 16 (6), 519–522.

Vinnik, L., Romanowicz, B., Le Stunff, Y., Makeyeva, L., 1995. Seismic anisotropy in the D "layer. Geophys. Res. Lett. 22 (13), 16571660.

Walker, A., Wookey, J., 2012. MSAT-A new toolkit for the analysis of elastic and seismic anisotropy. Comput. Geosci. 49, 81–90.

Walker, a. M., Forte, a. M., Wookey, J., Nowacki, a., Kendall, J.-M., Oct. 2011. Elastic anisotropy of D" predicted from global models of mantle flow. Geochem. Geophys. Geosyst 12 (10), 1–22.

Wang, Y., Wen, L., Sep. 2007. Complex seismic anisotropy at the border of a very low velocity province at the base of the Earth's mantle. J. Geophys. Res. 112 (B9), 1–11.

Wen, L., 2001. Seismic evidence for a rapidly varying compositional anomaly at the base of the Earth's mantle beneath the Indian Ocean. Earth Plan. Sci. Lett. 194 (1-2), 83–95.

Wenk, H.-R., Cottaar, S., Tomé, C. N., McNamara, A., Romanowicz, B., Jun. 2011. Deformation in the lowermost mantle: From polycrystal plasticity to seismic anisotropy. Earth Plan. Sci. Lett. 306 (1-2), 33–45.

Wentzcovitch, R. M., Tsuchiya, T., Tsuchiya, J., Jan. 2006. MgSiO3 postperovskite at D" conditions. PNAS 103 (3), 543–6.

Woodhouse, J. H., Giardini, D., Li, X. D., 1986. Evidence for inner core anisotropy from free oscillations. Geophys. Res. Lett. 13 (13), 1549–1552.

Wookey, J., Kendall, J., 2008. Constraints on lowermost mantle mineralogy and fabric beneath Siberia from seismic anisotropy. Phys. Earth Plan. Int. 275 (1), 32–42.

Wüstefeld, A., Bokelmann, G., Zaroli, C., Barruol, G., May 2008. SplitLab: A shear-wave splitting environment in Matlab. Comput. Geosci. 34 (5), 515–528.

Chapter 5

Deformational induced seismic anisotropy in the lowermost mantle

5.1 Introduction

While the bulk of the lower mantle appears to be mostly isotropic, the presence of strong and laterally varying anisotropy in D is now well established (e.g. Lay et al., 1998; Kendall and Silver, 1998; Lay and Garnero, 2007). Evidence for the presence of anisotropy in D″ comes from different shear wave phases: direct S, core-diffracted S_{diff}, core-reflected ScS, and core phases SK(K)S. The first observation of differential SH-SV velocities in S_{diff} was made by Vinnik et al. (1989), where the SV component was delayed with respect to SH by several seconds for a deep earthquake and a path through the Pacific ocean. The rays were oriented in such a way that contribution from upper mantle anisotropy, as known from independent studies, was minimal (no splitting of SKS or SKKS), indicating that origin of the travel time difference between SH and SV is in the diffracted portion of the path in the deep mantle. The initial interpretation of the observed splitting was complicated by the presence of a low velocity layer in D″ that allowed the observation of SV_{diff} with significant amplitudes at distances larger than 110°, also delaying the arrival of SH_{diff} by more than 10 s (e.g. Vinnik et al., 1995). However, other observations of S_{diff} splitting followed, including at shorter distances (Lay and Young, 1991), and in regions where the velocity in D″ is faster than average (e.g. Kendall and Silver, 1996; Matzel et al., 1996; Garnero and Lay, 1997). Splitting was also observed in ScS (e.g. Russell et al., 1998; Rokosky et al., 2006; Nowacki et al., 2011) and in direct S (e.g. Ford et al., 2006). Evidence for very large splitting has also been shown, implying the presence of strong anisotropy, on the order of 10% (e.g. Garnero and Lay, 1997; Vinnik et al., 1998). SKS and SKKS phases have been used to show strong lateral variations in azimuthal anisotropy (Long, 2009; Lynner and Long, 2012). In the previous chapter we discussed the presence of strongly laterally varying anisotropy across the margin of the African LLSVP observed via shear diffracted phases at large distances.

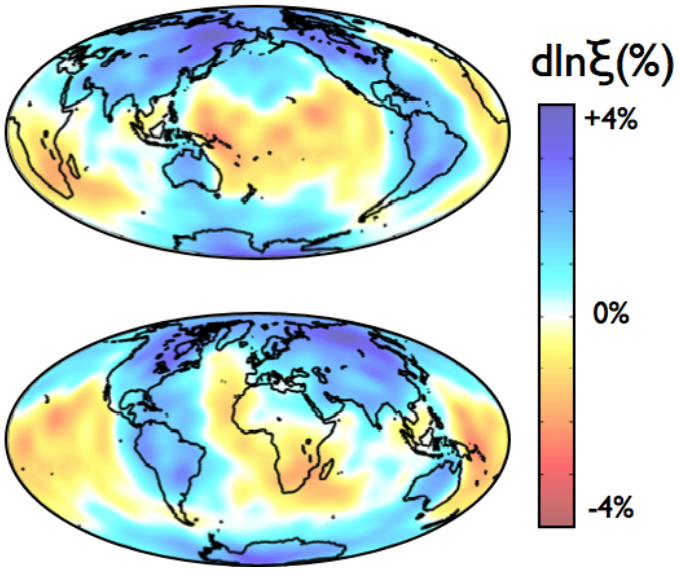

Figure 5.1: Radial anisotropy in the global model of Panning and Romanowicz (2006) at a depth of 2800 km. For values greater than 1.0, the shear wave polarized parallel to the CMB is faster than those polarized vertically, while for the values smaller than 1.0 the opposite is true.

The regional observations have been confirmed with the results of global tomographic inversions, which solve for radial anisotropy throughout the mantle. Figure 5.1 shows a depth slice through such a tomographic model (Panning and Romanowicz, 2006). In these models, D″ stands out as a region where, on average $V_{SH} > V_{SV}$, whereas the lateral variations appear to be correlated with the isotropic velocity structure in D″, with $V_{SH} > V_{SV}$ in fast regions, and patches of $V_{SV} > V_{SH}$ near the LLSVPs (Panning and Romanowicz, 2006; Kustowski et al., 2008; Kawai and Geller, 2010).

Seismologists are restricted in their characterization of anisotropy in the lowermost mantle, because for most areas the azimuthal coverage is insufficient to distinguish between radial anisotropy and other types of anisotropy. Azimuthal anisotropy requires full waveform modeling (e.g. Maupin, 1994, 2005; Garnero et al., 2004). Another challenge is to correct for contamination by near-source and nearreceiver anisotropy. One approach to eliminating source effects from the upper mantle is to study deep earthquakes. However, large and deep earthquakes are few and their global distribution is limited to mainly South America and the western Pacific. Recently, the use of ScS phases and correction of the source- and receiver side anisotropy using S-waves has improved, providing more crossing rays and making it possible to measure tilted radial anisotropy (Wookey and Helffrich, 2008; Nowacki et al., 2010, 2011).

The cause of seismic anisotropy at the base of the mantle is a source of much specula-

tion, and although there is general consensus that it could be related to mantle deformation, many important questions remain. If mantle deformation is accommodated by dislocation creep, it is expected to produce seismic anisotropy due to the alignment of anisotropic minerals, i.e. lattice-preferred orientation (LPO) (e.g. Karato, 1998a,b; Lay et al., 1998; Kendall, 2000) as is generally assumed to occur in the upper mantle (e.g. Becker et al., 2008; Long and Becker, 2010). Another possible cause for anisotropy is shape-preferred orientation (SPO) caused by alignment of melt inclusions or laminated solid materials. Both have been proposed for the D″ (e.g. Kendall and Silver, 1996). Additionally, the possible presence and role of postperovskite (pPv) must be added to the equation (Lay et al., 2006; Hirose and Karato, 2006; Ammann et al., 2010). It has been suggested that, in relatively cold regions, perovskite (Pv) could transform to pPv at D″ depths and account for the observed D″ discontinuity (e.g. Murakami et al., 2004; Iitaka et al., 2004) as well as for the faster velocities in D″ (Tsuchiya et al., 2004; Stackhouse et al., 2005; Merkel et al., 2007). In the warmer regions, the D″ transition of Pv to pPv would be pushed to pressures below the core-mantle boundary, explaining the absence of significant anisotropy in some areas, and its different character in others. Recently, experiments have shown that the depth and sharpness of the post-perovskite transition, depends not only on temperature, and not only on composition (Catalli et al., 2009; Grocholski et al., 2012).

In this study we perform forward modeling of LPO anisotropy in D″ with the goal of combining tools and observations developed by geodynamicists, seismologists and mineral physicists, in order to gain better understanding of the origin of seismic anisotropy in D″ and to determine which microscopic and macroscopic processes may or may not be at play. The ultimate goal is to interpret global anisotropy models and local observations (as the ones made in the previous chapter) in terms of material flow. We have developed a step-by-step approach: (1) Geodynamical models can provide characteristic information on the macroscopic strain accommodated by deformation of mantle minerals. (2) This strain deformation information is input as boundary conditions in numerical models that calculate mineralogical texture development within a polyphase aggregate. (3) Seismic elastic constants, determined from mineral physics, are calculated for numerous locations throughout the region of interest, (4) followed by forward seismic modeling through the 3D elastic anisotropic model acquired from steps 1-3. (5) Resulting models and seismic waveforms are compared to available seismic observations. These steps are described in more detail in Section 5.2.

Initially we created a two-dimensional model of a subducting slab that reaches the core-mantle boundary (CMB) and subsequently migrates along the CMB toward upwelling centers. Our model incorporates results from a range of deformation experiments and single crystal elastic properties calculated from first principles. Initial results show that macroscopic observations can constrain plausible constituents and deformation mechanisms. More specifically we conclude that an assemblage of post-perovskite with a dominant (001) slip and MgO with {110} and {111} slip explains seismic observations best. Additionally, our results suggest a possible link between seismic observations of anti-correlated velocities and seismic anisotropy in the deep mantle.

Next, we extend our model to three dimensions. We confirm that the results based on radial anisotropy from the 2D case are the same at the center of the slab, implying that there is little deformation parallel to the slab, and the slab can be treated as a 2D feature. The 3D model allows us to evaluate azimuthal anisotropy at the center and on the edges of the slab. Additionally, the 3D geodynamical model will include the effects of geometrical compression of a subducting slab in a spherical geometry.

In the following sections we first explore the set-up to combine multiple disciplines and the assumptions required in each field. In Section 5.3, we discuss the results for the 2D and 3D models. In the end we compare our results to other recent studies following a similar procedure (Section 5.4)

5.2 Methods

5.2.1 Geodynamical Model

Geodynamical models provide predictions of strain for the lowermost mantle. We concentrate on subducting lithosphere and the subsequent impinging on the core-mantle boundary. Regions where subducting slabs are expected show higher-than-average seismic velocity and stronger and more consistent patterns in radial anisotropy (Panning and Romanowicz, 2006; Kustowski et al., 2008). These also appear to correlate with regions where local studies observe strong tilted or azimuthal anisotropy (Rokosky et al., 2006; Long, 2009; Nowacki et al., 2011), as we have also seen in Chapter 4.

Our collaborators Allen McNamara and Mingming Li (at Arizona State University) provide data from their high resolution geodynamical models. The models are run with a modified version of Citcom (Moresi et al., 1996) for the 2D model and CitcomCU (Zhong et al., 2000; Tan et al., 2006) for the 3D model. These finite element codes solve for the conservation of mass, momentum and energy using the Boussinesq approximation. The thermal boundary conditions are isothermal at the top and bottom and insulating on the sides. The velocity boundary conditions are free-slip on all boundaries.

The internal deformation in these models are tracked by Lagragian tracers (McNamara and Zhong, 2004; Wenk et al., 2006; Merkel et al., 2007). These are entered into the model after the model has run for some time and thermal equilibrium has been reached.

5.2.1.1 2D

Viscosity profiles were used as a function of temperature and depth:

$$\eta(T, z) = \eta_z(z) exp[A(0.5 - T)] \tag{5.1}$$

where η_z is the non-dimensional viscosity; it has a value of 1 for the upper mantle and 50 for the lower mantle. A is the activation parameter (9.2103) and T the non-dimensional temperature (T=1 is the temperature at the CMB). The model has a Rayleigh number of 10^7 (reference for a upper mantle viscosity at a non-dimensional temperature of T=0.5).

Figure 5.2 shows the temperature snap-shot in the high-resolution 2D model. We investigate LPO development within a subducting slab from where it enters the D″ (and potentially goes through a phase transition) to where it is ultimately swept into a region of upwelling. The top panel is the entire-mantle temperature field, in which two downwellings are shown near the horizontal center. We focus on the downwelling toward the right, in the zoomed-in area denoted with a black box. The lower panel shows this zoomed-in region, which illustrates the long-axis of strain deformation in this region. Downwelling material is horizontally strained via pure shear as it approaches the CMB, and it is subsequently rotated and sheared as it moves laterally toward an upwelling plume. This time-dependent strain information (stored as numerous Lagrangian tracers) is used as input in our polycrystal plasticity code to predict LPO formation in this region.

Note that this model includes descending slabs that hit the CMB and rotate along it. Other types of slab behaviors, depending on the internal strength of the slab, might include intense buckling in the lower mantle, or ponding into a blob on the core-mantle boundary (e.g. Nakagawa and Tackley, 2005; Loubet et al., 2009), but are not represented in the model here. The deformation in this model is slightly complicated by the start of a hot, dynamic instability beneath the cold slab material (as can be seen in the snapshot).

We choose eight tracers to represent the deformation in this region within a period during which downwelling in the model is fairly stable and the dynamic instability beneath the slab has not 'broken' through. The eight tracers travel through this region at around the same time. A tricky aspect of our method is that we we work towards one 'snap shot' model of seismic anisotropy, even though different regions of the model will represent different times in the geodynamical model. The deformation at any given location can change with time. However, the Lagragian approach is crucial to have the seismic anisotropy at a given location represent the deformational history of that material.

One example of deformation for the lowermost tracer is represented by the different components of the velocity gradient tensor in Figure 5.3. As required by the conservation of volume, the two values along the principal components — dV_X/dx and dV_Z/dz components in the upper panel— balance each other out. As for simple shear deformation —dV_X/dz and dV_Z/dx components in the lower panel—, the gradient in horizontal velocity in the vertical direction (dV_X/dz) is strong in the horizontal flow above the CMB. dV_Z/dx is only strong in the region where an upwelling is developing beneath the slab and switches sign before and after this part. This deformation pattern rotates within the upwelling at the end of the tracer. As the tracer speeds up in the upwelling, this part of the path only represents very few time steps.

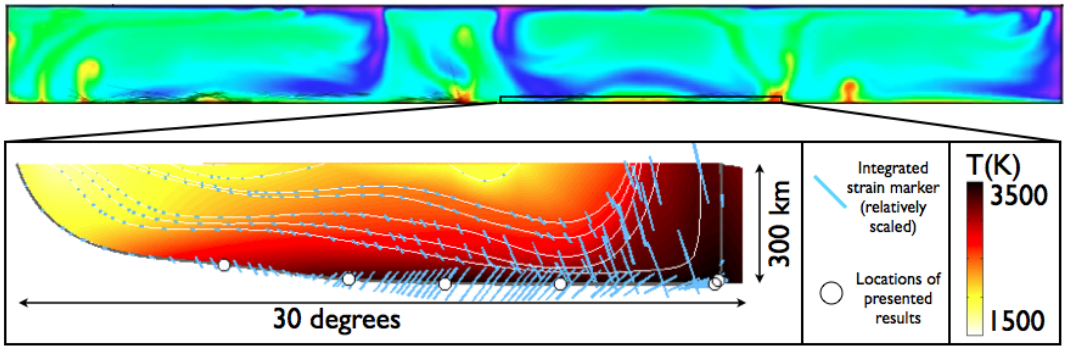

Figure 5.2: 2D convection pattern in D zone with subducting slabs and upwelling plumes. Colors indicate temperature (purple/blue: cold, red/yellow: hot). Lower plot shows interpolated temperature and strain markers along the used tracers in the black box in the top figure. Strains become very large in the upwelling. Exemplifying plots in this chapter will show results for the lowermost tracer in this plot (tracer 189, also referred to here as tracer I). Time steps are denoted along this tracer.

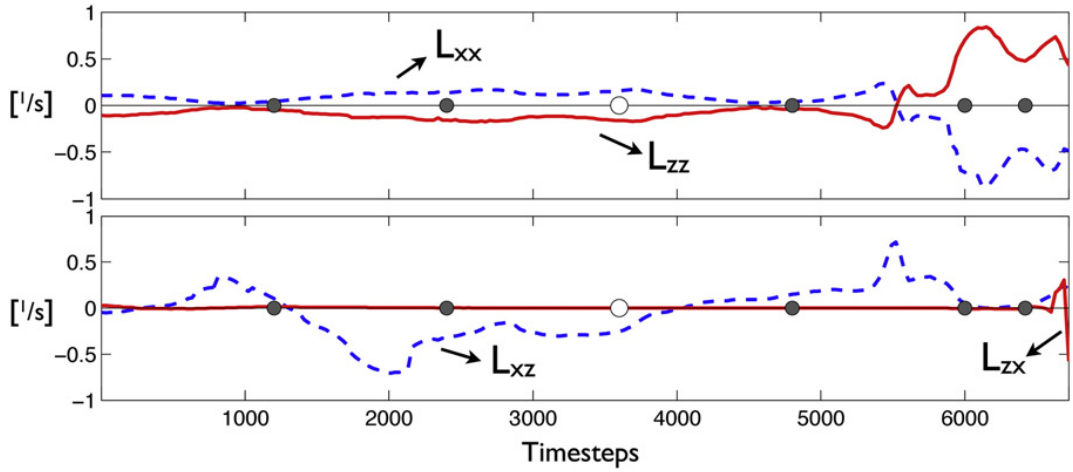

Figure 5.3: Evolution of velocity gradient tensor components along tracer I. Top figure: dashed line is dV_X/dx, solid line is dV_Z/dz. Bottom figure: dashed line is dV_X/dz, solid line is dV_Z/dx.

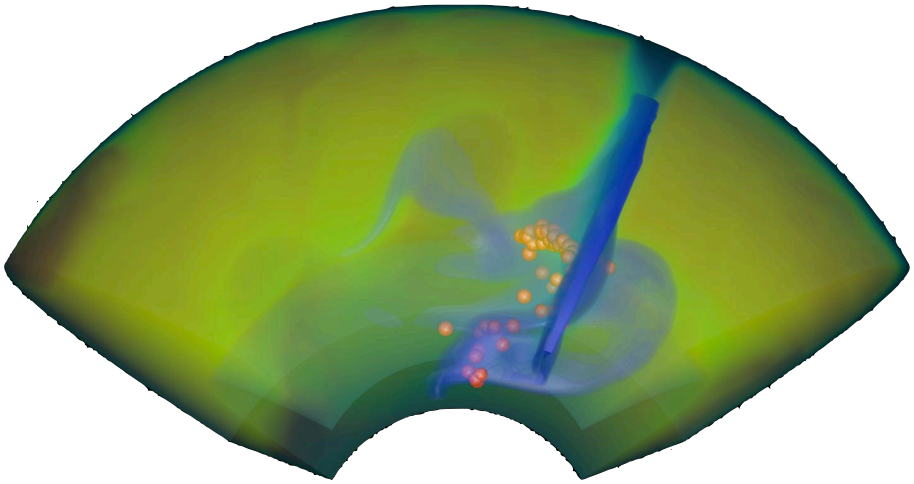

Figure 5.4: Snapshot of the temperature in the 3D geodynamical model looking from the south. Subduction occurs around a longitude of 80°. Orange dots represent example tracers which are inserted at the top and then travel along the slab. [Figure courtesy of Mingming Li]

5.2.1.2 3D

The 3D geodynamical model uses the version CitcomCU. The Rayleigh number is 10^8, the viscosity again scales with temperature and depth, creating four orders of magnitudes difference in velocity between the highest and the lowest temperatures and including a factor of 30 increase in the non-dimensional viscosity between the upper and the lower mantle.

The domain of the 3D model covers 1/6 of the spherical shell: longitude ranges from 0 to 120° and colatitude from 30 to 150°. In this model the downwellings are controlled by 'plate tectonics' at the surface, implemented as a fixed velocity boundary condition. Between 0 and 80° longitude the boundary condition is a westward velocity, and velocities are zero ('fixed plate') between 80 and 120°. This results in a stable downwelling in the system (see Figure 5.4). Figure 5.5 shows a cross section of temperature and viscosity at 96 Ma into the model run.

10^4 Langragian tracers are entered in the slab at the top and subsequently subduct with the slab. The tracers that exit the slab at shallow depths are reentered at the top.

One complication that has arisen with this model is the geometrical compression the slab undergoes as it subducts. As the slab extends over the full latitudinal range, it becomes squished and bends inwards at it edges. Although it is interesting to look at the change of anisotropy patterns here, it is not necessarily a realistic effect in the earth. In a future

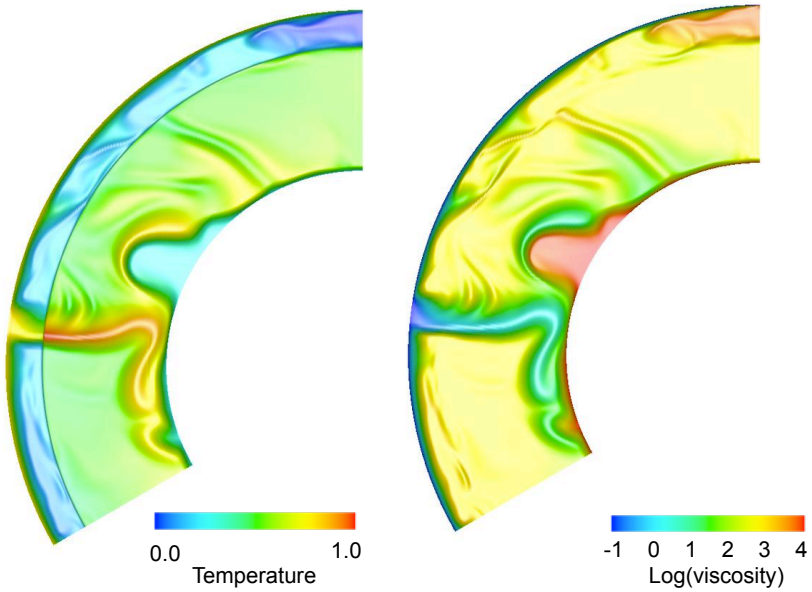

Figure 5.5: Two cross-sections through the slab at 96 Ma in the 3D geodynamical model. Besides the slab, the cross-section shows the development of an upwelling. The non-dimensional temperature on the left and the non-dimensional logarithm of viscosity on the right. [Figure courtesy of Mingming LI]

model, the slab will be half the current width, to represent more natural slab edges.

5.2.2 Mineral Physics

5.2.2.1 Visco-Plastic Self-Consistent Modeling

For LPO to form, we assume the main deformation mechanism is slip, i.e. the propagation of dislocations through the crystallographic planes. The direction of LPO or texture will depend on which lattice planes dislocations move. Other deformation mechanisms, like diffusion creep (the propagation of vacancies through a lattice), do not result in LPO and may even reduce LPO.

The relative activity of different slip systems (combination of crystallographic plane and propagation direction) which lead to a particular LPO are computed with the Visco-Plastic Self-Consistent (VPSC) method (Lebensohn and Tomé, 1993; Lebensohn, 2007; Molinari et al., 1987). A starting texture of the sample is defined by individual crystal orientations. Here we start with 500 grains which have no preferred orientation. All crystals are then visco-plastically deformed to a degree dependent on their orientation relative to the direction of stress. Each crystal is treated as a finite inclusion within and interacting with a so-called

infinite 'effective medium' that has the average properties of the polycrystal material. The inclusion is assumed to be under constant strain. This formalism is also known as an 'Eshelby inclusion' (Eshelby, 1957). The crystal reorientation within this medium is a result of deformation by slip along specific lattice plains and resulting rotation. The properties of the effective medium are not known in advance, but are required to fit the constitutive equations between stress and strain when averaged. After an educated initial guess, one iterates between fitting the weighted behavior of the individual grains, and a consistent mean response of the effective medium on the polycrystal level. Following this approach is referred to as the self-consistent part of the method.

In our model, we assume 50% of the deformation to be accommodated by dislocation creep. The rest of the deformation is accounted for by other mechanisms, such as diffusion creep, although these are not modeled (but could potentially reduce the texturing). The choice of this number is arbitrary so as to lower the amount of anisotropy in the end (pure dislocation creep results in unrealistically high anisotropy).

The grain inclusions are initialized with a spheroidal shape, but become ellipsoidal under deformation. We stop further deformation when an ellipsoidal ratio of 3:1 is reached, but still allow for rotation of crystallographic planes.

To model deformation of the different phases, the VPSC method requires input on the prefential slip planes of each phase and the single crystal elastic properties. These are described in the following two sections for MgO, perovskite and postperovksite. We model the deformation for a nearly pyrolitic composition, 75% (post)perovskite and 25% MgO.

5.2.2.2 Deformation Mechanisms

Our knowledge of slip systems for lower mantle minerals comes from experiments at high pressures and temperatures. For lower mantle conditions, experiments are done by pressing a polycrystal sample in a diamond anvil cell (DAC) and heating the sample with a laser. The texture is recorded in-situ by x-ray diffraction. These types of experiments have been applied to MgO (Merkel et al., 2002; Stretton et al., 2001; Yamazaki and Karato, 2002; Lin et al., 2009), perovksite (Karato et al., 1995; Wenk et al., 2004) and pPv (Merkel et al., 2006, 2007; Miyagi et al., 2009, 2010; Miyajima and Walte, 2009; Okada et al., 2010; Walte et al., 2009). The texture results are often numerically replicated with VPSC simulations in order to determine the slip system activity (i.e. the critical resolved shear stress (crss)) of the various slip planes.

Active slip planes for (Mg,Fe)O are 111, 110 and 100 planes with 110¡110¿ being most active. For orthorhombic perovskite, slip dominates on the (001), but also occurs along (100) and (010) planes.

Post-perovskite deformation is more ambiguous; (Merkel et al., 2006) found that a combination of planes near (100) and (110) dominate— (Miyagi et al., 2009) find (010)— while

periclase								
	111<10$\bar{1}$>	110<$\bar{1}$10>	100<011>					
	0.75	0.5	1					
perovskite								
	(100)[010]	(100)<011>	(010)[100]	(010)<101>	(001)[100]	(001)[010]	(001)<110>	
	3	4	3	4	1	1	1	
postperovskite								
	(100)[010]	(100)[001]	(010)[100]	(010)[001]	(001)[100]	(001)[010]	(110)<$\bar{1}$10>	(110)[001]
A	1	1.5	3	3	3	3	2	2
B	3	3	1	1.5	3	3	3	4
C	2	2	4	4	1	1.5	3	4

Table 5.1: Slip planes $\{hkl\} < uvw >$ and critical resolved shear stress values applied for the different phases in this study. We assume the crss values remain constant with pressure and temperature.

Miyagi et al. (2010) Miyagi et al. (2010) find that (001)¡100¿ and (001)¡010¿ dominate. The latest experiment, finding (001), is the most supported result now. The earlier experiments might have been obscured by the occurring phase transformation, and by working on analog materials (Miyagi et al., 2011). In this study, however, we consider all three possibilities and characterize the resulting LPO. We name the different cases by their most dominant plane; pPv^A (100), pPv^B (010) and pPv^C (001). The slip planes and their critical resolved shear stress values used in this study are listed in Table 5.1.

In our models, we combine 75% Pv or pPv with 25% MgO. As can be seen from the relative critical resolved shear stress coefficients, MgO is a weaker phase and is therefore predicted to take up more of the deformation. In Figure 5.6 the activities of the various planes along tracer I are shown. The sum of all the activities adds up to 1.0, but we have plotted only the more active planes. Along most of the tracer, the main active slip plane is in MgO, namely {111}. Interestingly, {111} slip is more active than the slip with the lowest crss, {110}. This is because {111} represents a slip plane group with more symmetry planes than {110}. In total, MgO accommodates about half of the deformation even though it makes up only 25% of the assemblage. If that is actually the case for a polyphase mixture remains unknown. If the lower mantle is very perovskitic, as recently suggested (Murakami et al., 2012); the MgO might only be present as inclusions surrounded by Pv. As the stronger Pv grains are connected, they might end up taking up the majority of the deformation. The exact behavior will likely change with the amount of MgO present. We will see later, however, that even though the MgO becomes more textured, it is less elastically anisotropic and does not dominate the resulting anisotropy.

An example of the texture development is shown in Figure 5.7. This example shows texturing of the (001) pole along tracer I for pPv^C (001) at various time steps along the tracer (indicated in Figure 5.2). We see that the (001) plane (orthogonal to the (001) pole plotted here) becomes parallel to the main compression axis, dVx/dx. The slight rotation from this axis comes from the simple shear component in the deformation. In the final time step plotted, the tracer enters a region of upwelling and the preferred orientation rotates.

Figure 5.8 shows the densities of the three poles for the different phases at one location

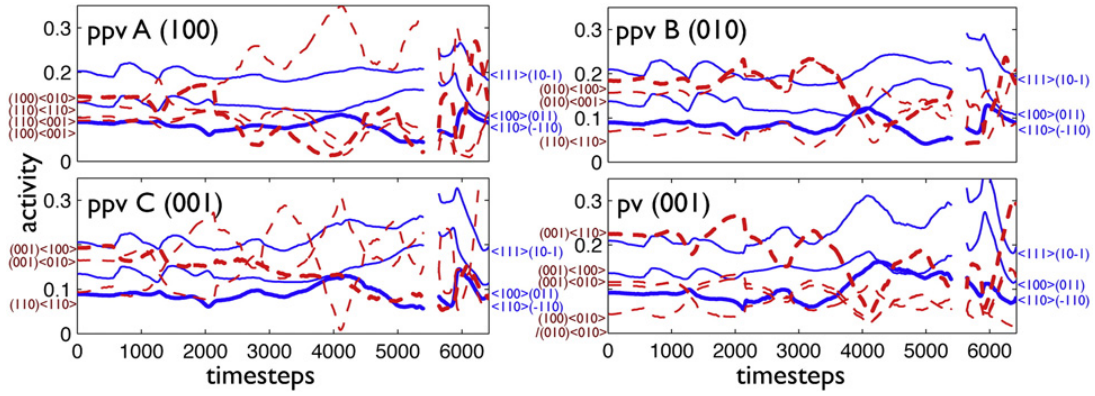

Figure 5.6: Activities of the various slip planes along tracer I for four different polyphase assemblages. Solid blue lines are slip systems in the MgO, dashed red lines are for Pv/pPv. The activities around #5600 are not plotted due to numerical instabilities occurring here; the anomalous behavior here does not have a significant effect on the overall texture.

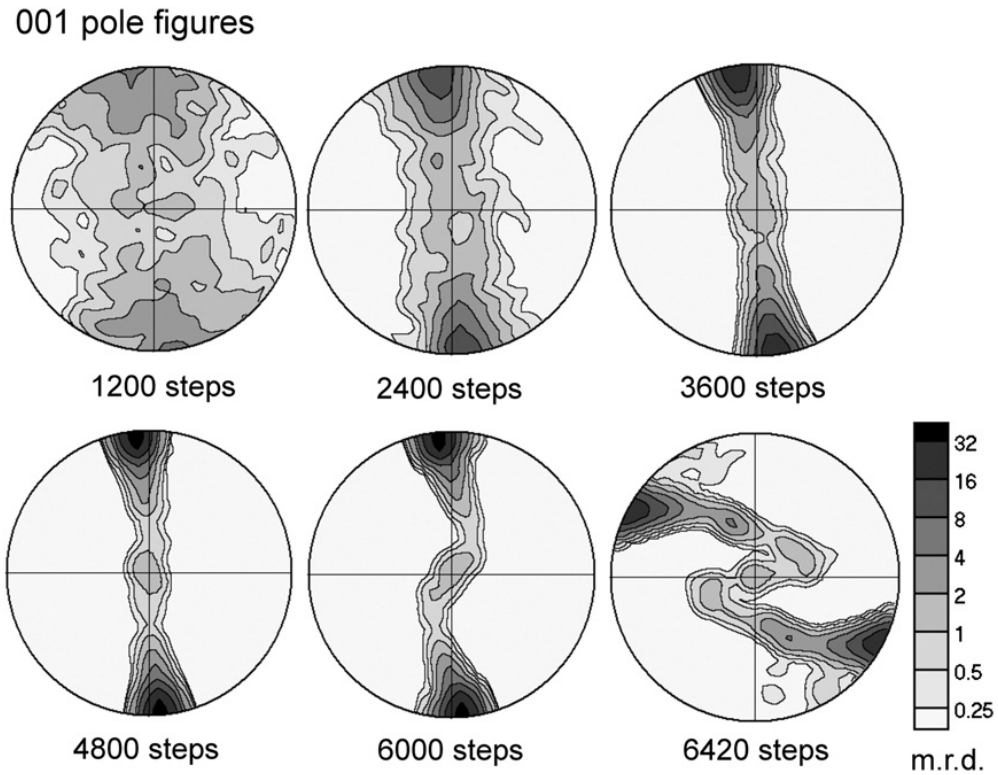

Figure 5.7: Resulting textures or preferred orientation showing the density of (001) poles as a equal area contour plot (scale is quadratic). This texture development is along the lowermost tracer for pPv^C (001). A rotation of the final texture occurs at the final time step plotted (where the tracer enters an upwelling). Figure courtesy of Rudy Wenk.

ρ (kg/m^3)	C11 (GPa)	C12 (GPa)	C13 (GPa)	C22 (GPa)	C23 (GPa)	C33 (GPa)	C44 (GPa)	C55 (GPa)	C66 (GPa)	
periclase	5.07	1154.0	265.5	265.5	1154.0	265.5	1154.0	198.0	198.0	198.0
perovskite	5.25	860.0	535.5	437.0	1067.5	467.5	1053.0	294.0	249.5	284.5
pPv_1	5.35	1220.0	474.0	359.0	899.0	493.0	1176.0	273.0	245.0	376.0
pPv_2	5.29	1104.5	454.6	429.0	869.5	504.3	1104.5	305.5	224.0	329.5

Table 5.2: Density (g/cm^3) and elastic stiffness coefficients CIJ (GPa) at 125 GPa and 3000 K for MgO (Karki et al., 2000), Pv (Wentzcovitch et al., 2004), pPv 1 (Stackhouse et al., 2005), and pPv 2 (Wentzcovitch et al., 2006)

along the lowermost tracer close to the core-mantle boundary. We see that one slip plane, namely (100), (010) and (001), is dominating (seen from the strongly oriented poles) for pPv^A, pPv^C and pPv^C, respectively. Periclase has more symmetry planes, and therefore deformation is distributed along various slip planes; resulting in a more complex and diffuse texture.

So far, we have discussed the behavior of the purely Mg end-member phases. The deformational behavior with the inclusion of other major elements — Fe being the main candidate— remains uncertain. Recent studies have been done for Fe in MgO, a mineral known as magenesiowuestite (Lin et al., 2009), but not for Pv and pPv, the dominant phase from the point of view of the resulting elastic anisotropy.

5.2.2.3 Elastic Constants

The other main input for VPSC concerns single crystal elastic constants for the different phases. Once the orientation distributions are calculated, the elastic constants are averaged over their orientations to obtain the overall polycrystal elastic properties. At the moment, the mineral physical experiments are not capable of measuring single crystal elastic properties under lower mantle conditions of pressure and temperature. These values are determined by large computational codes solving for atomic and molecular structure using basic laws of quantum mechanics, a.k.a. *ab initio* calculations.

For MgO we apply results from Karki et al. (2000) and for perovksite from Wentzcovitch et al. (2004). For postperoskite we apply elastic constants from both Stackhouse et al. (2005) and Wentzcovitch et al. (2006), and will name them ,respectively, pPv_1 and pPv_2. A comparison in methods and results between these two studies is given in Stackhouse and Brodholt (2007) and Wentzcovitch (2010). An overview of all the applied constants is given in Table 5.2; the single crystal fast shear wave velocity and polarization direction is plotted in Figure 5.9. pPv has intrinsically higher anisotropy than Pv, and pPv_1 (from Stackhouse et al. (2005)) slightly stronger than pPv_2 (from Wentzcovitch et al. (2006)).

For all models we apply the elastic constants at 125 GPa and 3000 K. The elastic constants vary with pressure and temperature. We have run a test when including these variations, but concluded it had little effect on the anisotropic results, but strongly affected the isotropic velocity variations (discussed in Section 5.3.1.1).

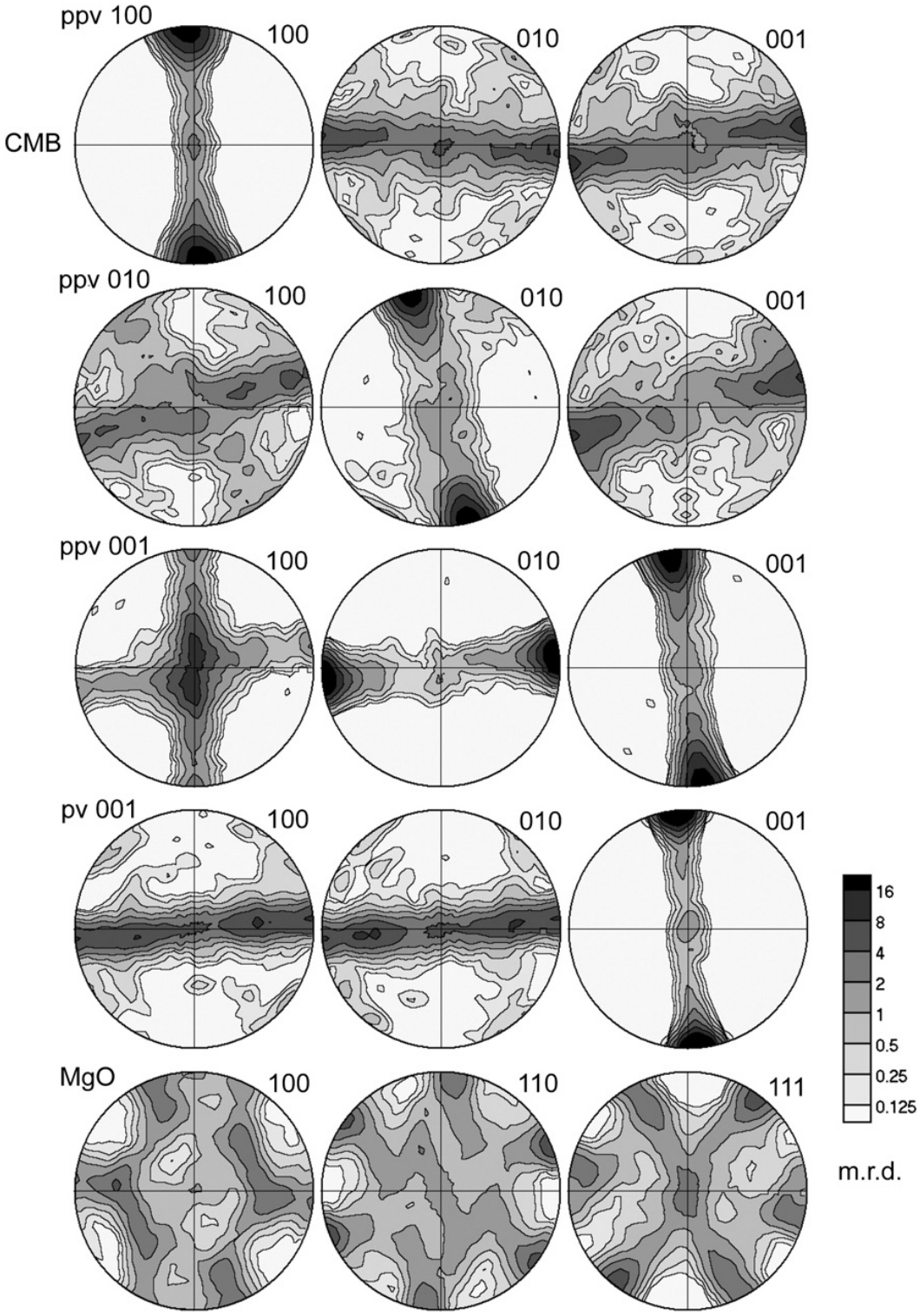

Figure 5.8: Resulting texturing or preferred orientation showing the density of all three poles for pPv_1^A, pPv_1^B,pPv_1^C, Pv and MgO. Time step 3600 along the lowermost tracer (see Figure 5.2). Equal area projection. Figure courtesy of Rudy Wenk.

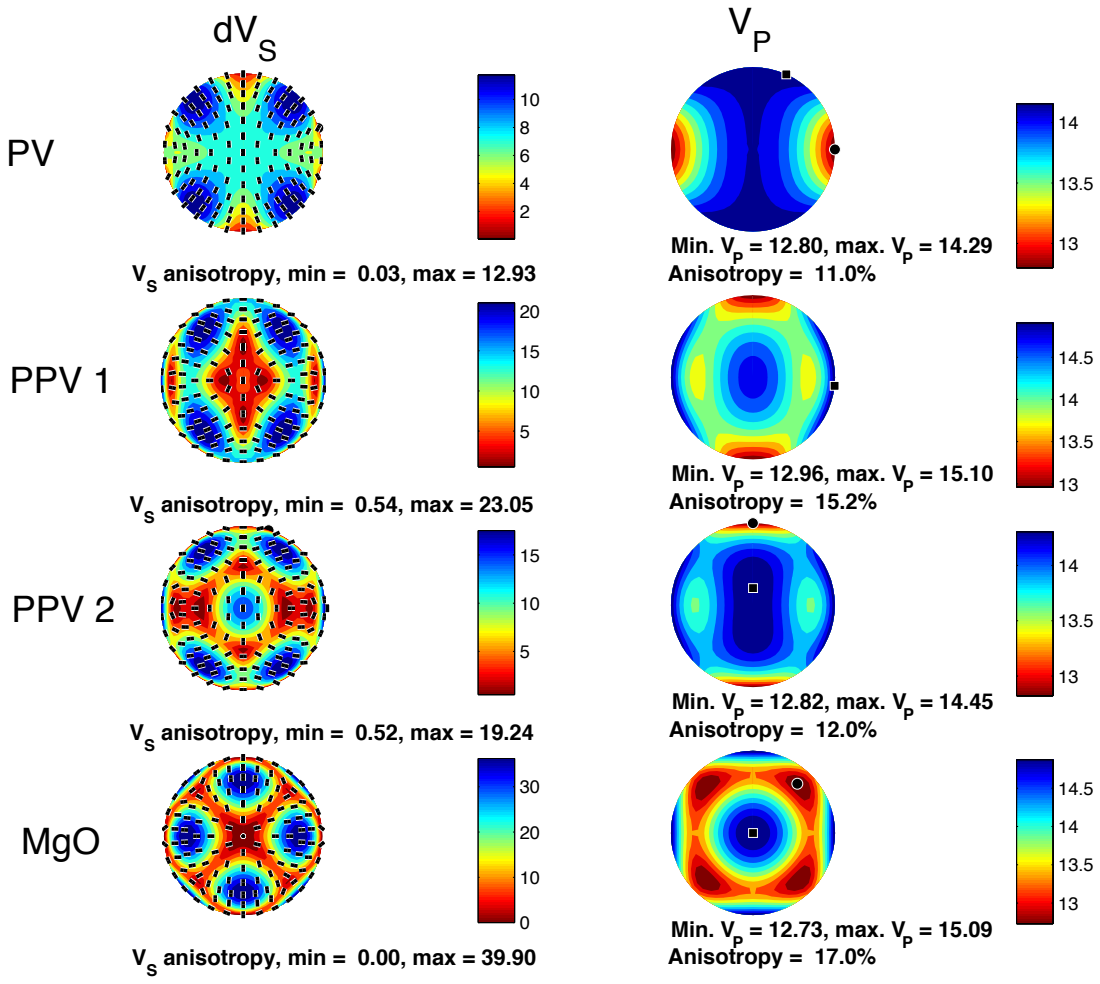

Figure 5.9: Anisotropy in the single crystals at 125 GPa and 3000 K applied in this study. On the left, differential shear wave velocities and the fast polarization direction (black bars). On the right, compressional wave velocity (km/s) as a function of propagation direction. Elastic constants are listed in Table 5.2.

5.2.3 Comparing to seismological results

From global tomographic models, we see a strong component of radial anisotropy in the lowermost mantle (Masters et al., 2000). Radial anisotropy represents the difference in velocity between horizontal and vertical polarized waves, often defined as $\xi = V_{SH}^2/V_{SV}^2$. In the models of Panning and Romanowicz (2006) and Kustowski et al. (2008), the main radial anisotropic signature beneath subduction zones is a faster V_{SH} than V_{SV} (or $\xi > 1$). From normal modes there is the suggestion that shear and compressional radial anisotropy may be anti-correlated (Beghein et al., 2006). We want to compare this signature with the radial anisotropy in our synthetically computed models.

For a given location, we compute ξ from the full elastic tensor, C, with coordinates (y,x,z) as:

$$\xi = \frac{V_{SH}^2}{V_{SV}^2} = \frac{C(6,6)}{C(5,5)} \quad (2D\ case) \tag{5.2}$$

$$\xi = \frac{V_{SH}^2}{V_{SV}^2} = \frac{2C(6,6)}{C(5,5) + C(4,4)} \quad (3D\ case) \tag{5.3}$$

For the 3D case we average both horizontal components.

The compressional radial anisotropy ϕ is computed as:

$$\phi = \frac{V_{PH}^2}{V_{PV}^2} = \frac{C(2,2)}{C(3,3)} \quad (2D\ case) \tag{5.4}$$

$$\phi = \frac{V_{PH}^2}{V_{PV}^2} = \frac{C(1,1) + C(2,2)}{2C(3,3)} \quad (3D\ case) \tag{5.5}$$

Other seismic observations come from splitting of shear body waves, e.g. ScS and SKS. To calculate the splitting in any given direction ($\mathbf{x}$) one computes the Christoffel matrix (Babuska and Cara, 1991):

$$\gamma_{kl} = C_{ijkl} x_i x_j / \rho \tag{5.6}$$

ρ is the density. γ_{kl} gives the matrix of squared velocities in that specific direction. Its eigenvalues give the squared phase velocities, V_P^2, V_{S1}^2, and V_{S2}^2 and the eigenvectors are the corresponding polarization directions.

5.2.3.1 CSEM full waveform modeling

To test the sensitivity of seismic phases to these models, forward modeling is essential. Until now, the tool that has been used the most is based on reflectivity synthetics for radial anisotropy (Moore, 2004). On the other hand, Maupin (1994) extended a WKBJ approximation approach first developed by Richards (1976) to the case of azimuthal anisotropy. Generalized ray theory has also been used (e.g. Sidorin et al. (1998)). These approaches

allow the testing of models, where an anisotropic elastic tensor is specified and synthetic seismograms are computed assuming a layered anisotropic structure. In view of the complexity of the actual structure and the possibility of lateral variations in the anisotropic as well as in the isotropic structure, it is necessary to be able to calculate synthetic seismograms using a method that can handle diffraction, the presence of a D$''$ discontinuity, as well as arbitrary lateral variations in anisotropic and elastic structure. For this purpose, one resorts to numerical methods. The Spectral Element Method (SEM), introduced to seismology by Faccioli et al. (1997) and further developed by Komatitsch and Vilotte (1998), Komatitsch and Tromp (1999, 2002); Chaljub et al. (2003), is accurate and well suited for this type of application, while quite computationally expensive. However, Capdeville et al. (2002) developed a hybrid method, which couples the SEM to a fast 1D normal mode computation across a spherical shell boundary (CSEM). The approach was later extended to the case of a heterogeneous region, in which the SEM computation is performed, sandwiched between two spherical shells with 1D structure (Capdeville et al., 2003). This considerably speeds up the computation, and has already been applied to the testing of heterogeneous structure in D$''$ for synthetic seismograms calculated down to $\sim$ 10s period (To et al., 2005; To and Romanowicz, 2009). In our work so far we have adapted the "sandwiched" CSEM code to include a full 3D elastic anisotropy model.

One challenging aspect of computing synthetic waveforms and comparing them to observed waveforms, is that the absolute velocities in our models are not correct. We have modeled a roughly pyrolitic composition. The fact that mean absolute velocities are not fit in the lower mantle could be due to the uncertainties in the behavior of MgO and (p)Pv at high pressures and temperatures. It could also mean that fitting the velocities requires incorporation (and knowledge of its behavior) of other major elements, as Fe, Ca and Al. With present day mineral physical constants, and uncertainties in the temperature profile, the velocities in the lower mantle (and definitely not the lowermost mantle) have not been fit in a consistant manner (Matas and Bukowinski, 2007; Cobden et al., 2008; Murakami et al., 2012). Here, we bypass this issue by taking the anisotropic component of the tensor and projecting it onto a 1D radial profile PREM. With that approach, we exclude any lateral isotropic variations, but any anomalies seen in our synthetic waves are purely due to the anisotropy in the model.

Another issue is the practical implementation of the model. We orient the 2D model along the longitude and extend the same model in the latitudinal direction, creating a 3D model. The individual elastic tensors are transposed from the (y, x, z)-coordinates to the (r, θ, ϕ)-coordinates of CSEM where r=-z, θ=y and ϕ=x. Where CSEM requests an elastic tensor at a given location (r, θ, ϕ), we return a triangulated interpolation between the nearest points along tracers in our model.

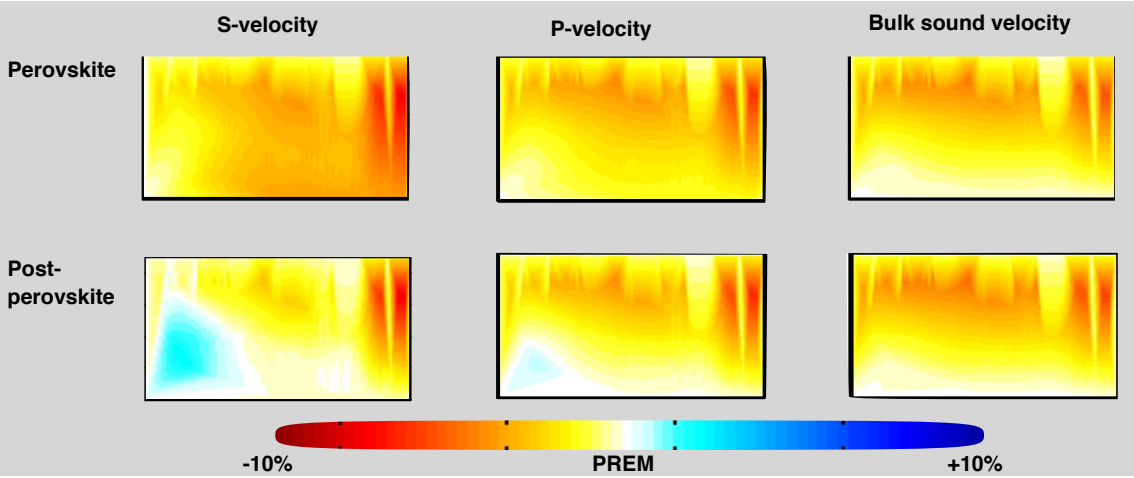

Figure 5.10: 2D isotropic velocity variations with respect to PREM along the slab and in the upwelling including temperature and pressure effects for the Pv and MgO model (top) and the pPv_1 and MgO model (bottom). Clearly, pPv can account for stronger isotropic velocity variations.

5.3 Results

5.3.1 2D Geodynamical Model

5.3.1.1 Isotropic Velocities

Initially the above tools and methods have been applied to a 2D slice through a subducting slab and upwelling plume (e.g. Figures 5.2).

As mentioned before, in general we will ignore isotropic velocity variations, as they are not representative of the lowermost mantle. This is due to incorrect ratio between (p)Pv and MgO and the simplification of excluding other major elements (e.g. Fe). However, we did attempt one run that varies the elastic constants as a function of pressure and temperature. This has little effect on the resulting anisotropy, but affects the variation in isotropic velocities. We do not evaluate the absolute resulting velocities, but present the isotropic velocities as deviations from PREM in Figure 5.10 . Variations are stronger than in typical inverted models. The temperature sensitivity of the shear modulus causes strong lateral S-wave velocity variations, while the bulk modulus and thus the bulk sound velocity have more sensitivity to vertical pressure variations. S-wave velocity variations are predicted to be stronger for pPv than for Pv. The occurrence of pPv can thus explain the increase of $dlnV_S$ in the lowermost mantle as seen in seismic inversion models.

5.3.1.2 Radial Anisotropy

Radial anisotropic models are shown in Figure 5.11, in which the case for pPv is expanded for three different dominating slip planes. As this figure shows, the different assemblages and deformation regimes result in different anisotropic signatures. The pPv assemblage for dominant slip planes of B (010) and C (001) corresponds with seismic observations of $V_{SH}>V_{SV}$ (blue), while the Pv assemblage has an opposite signature. It must be noted that applying elastic constants of (Stackhouse et al., 2005), switches the signature of pPv^B with a main slip plane of (010).

The P-wave anisotropy can further constrain the different dominant slip planes. The results for dominant slip planes of (010) and (001) have opposite signatures for P-wave anisotropy giving an additional constraint to distinguish between these two phases. (Beghein et al., 2006) find a likely anti-correlation between P and S wave anisotropy using normal modes, similar to the (001) case here. A number of local studies find anti-correlation between P and S wave velocities (Wysession et al., 1999; Tkalčić and Romanowicz, 2002), as well as global studies, which find an anti-correlation between shear wave and bulk sound velocities (Su and Dziewonski, 1997). Possibly these measurements indicate that the anti-correlation between SH and PH (or horizontal bulk sound velocity) is caused by anisotropy. Isotropic variations (Figure 5.10) alone cannot explain them.

We conclude that the latest experiments on pPv (Miyagi et al., 2010) are in good agreement and that dominant (001) slip in pPv combined with MgO can best explain the seismic observations, i.e. high anisotropy and polarization of fast S-waves parallel to the CMB in zones of lateral spreading as well as anti-correlation between P and S-wave anisotropy.

The results for the upwelling on the right in the plots (see Figure 5.2) are more difficult to interpret as we use a 2D model for these features, whereas in a realistic model, the 3D geometry is important as well as the presence of compositional variations.However, there is a sharp change in anisotropic signature, caused by the rotation of the already existing preferred orientation. The result is a boundary with a velocity jump that is sharper than is possible with isotropic variations due to temperature changes. Possibly, these changes across plume boundaries can be linked to seismic observations shown in Chapter 4 as well as observations of a sharp boundary for the African LLSVP (Ni et al., 2002; To et al., 2005). It also remains questionable whether dislocation creep can occur and whether pPv is stable at the higher temperatures.

5.3.1.3 Azimuthal Anisotropy

Interpreting the azimuthal anisotropy in our 2D model must be done with some caution, since we do not allow for deformation in the third dimension. In Figure 5.12 we show the fast and slow shear velocities and compressional velocity as a function of propagation direction

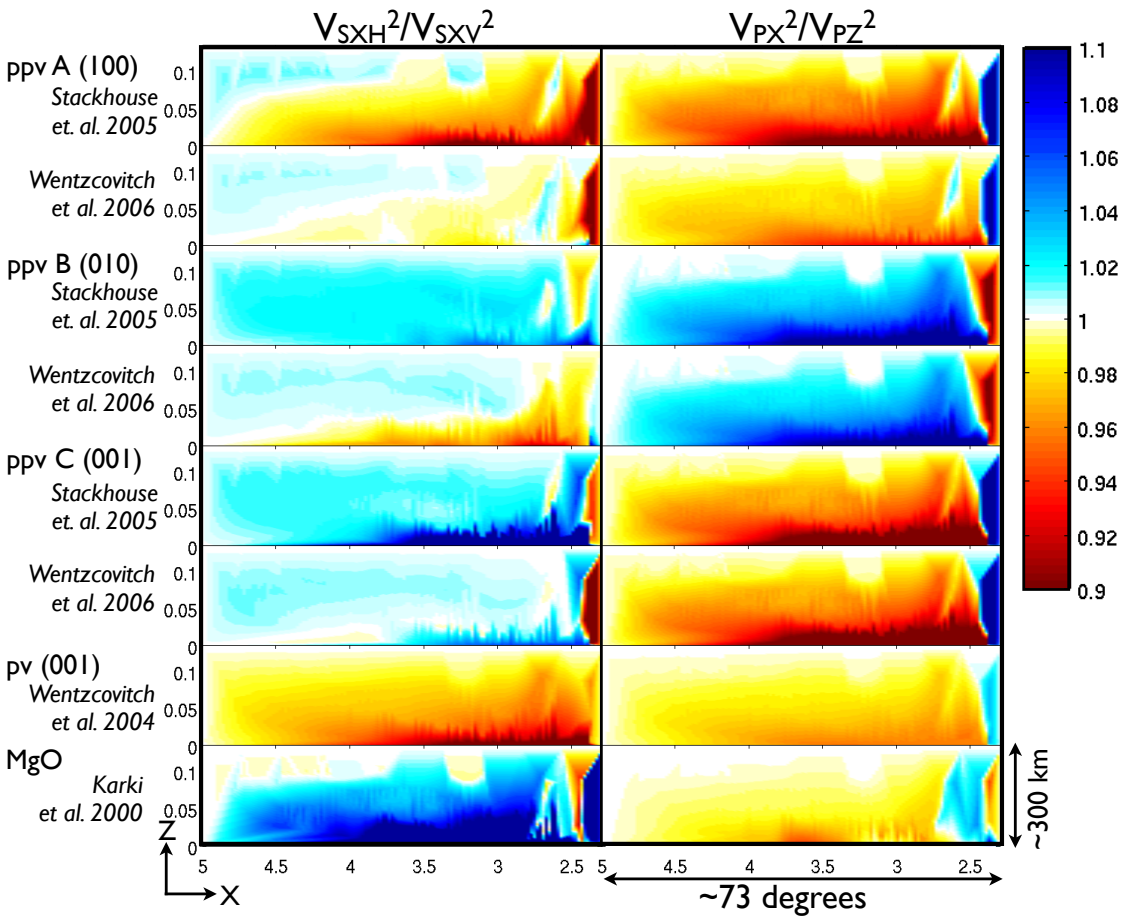

Figure 5.11: Calculated S-wave and P-wave anisotropy for single phase models in D″ expressed by $\xi = (V_{SXH}/V_{SXV})$ and (V_{PX}/V_{PZ}) for all seven models. V_{SXH} and V_{SXV} are the velocities of horizontally and vertically polarized wave traveling in the x-direction. Values less than 1.0 indicate that the fast S-wave is polarized parallel to the CMB. The ratio of the velocities of a P-wave traveling in the x-direction and a P-wave traveling in the vertical direction, quantifies the P-wave anisotropy. Values less than 1.0 indicate that the fast P-wave is parallel to the CMB. The behavior of the second phase MgO is the same for all models and only shown for the combination with Pv.

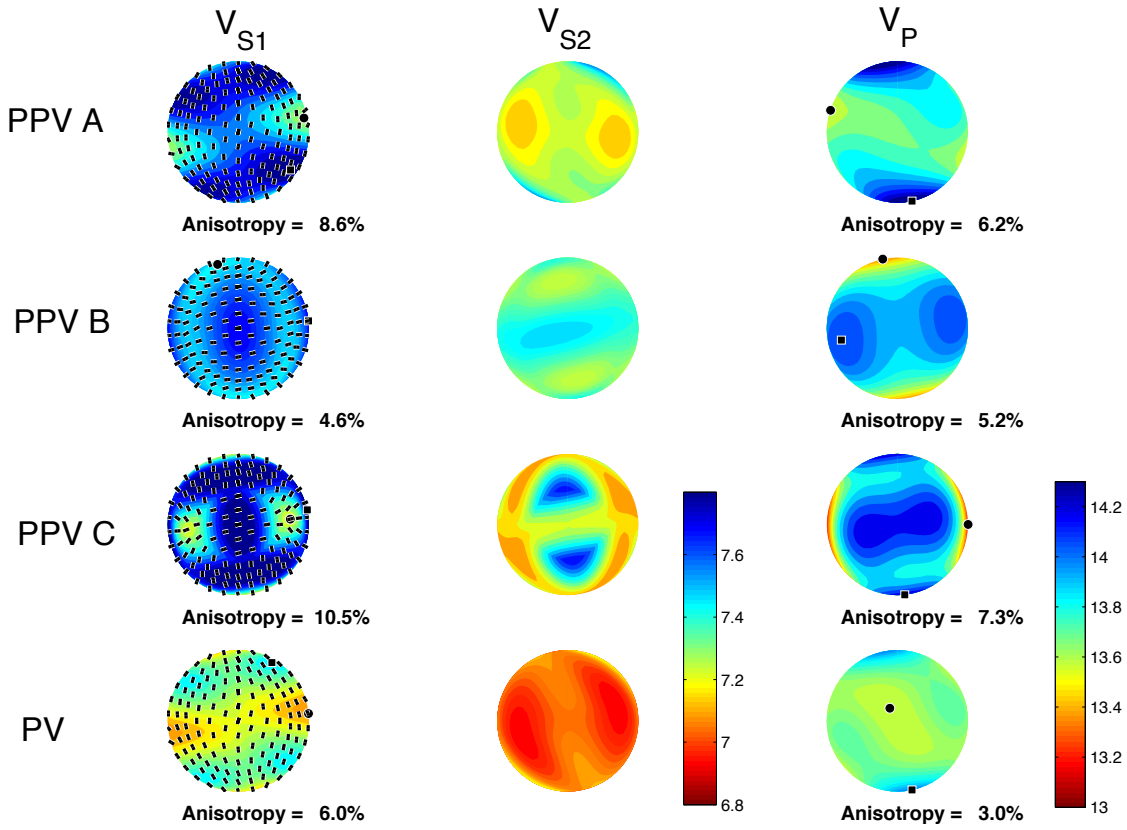

Figure 5.12: Fast and slow shear velocity (km/s), and compressional wave velocity (km/s) as a function of propagation direction at a single location (at time step 3600 along the lowermost tracer). Compositional models are MgO mixed with Pv, pPv_1^A, $\mathrm{pPv}_1^B$and pPv_1^C (from top to bottom). The core-mantle boundary is horizontal. Black lines indicate the fast polarization direction.

for one location near the core-mantle boundary. The azimuthal anisotropy is represented by the variation in seismic velocity along the horizontal axis. Azimuthal anisotropy is strongest for pPv^C.

It is not surprising that azimuthal anisotropy is weak in these models. The main component of deformation is co-axial plain strain: this results in the main slip system becoming horizontal and its pole becoming vertical (see Figure 5.8). The orientation of poles in the horizontal remains fairly random. That pPv^C (001) has the strongest azimuthal anisotropy is consistent with stronger texturing in the horizontal plane seen in Figure 5.8.

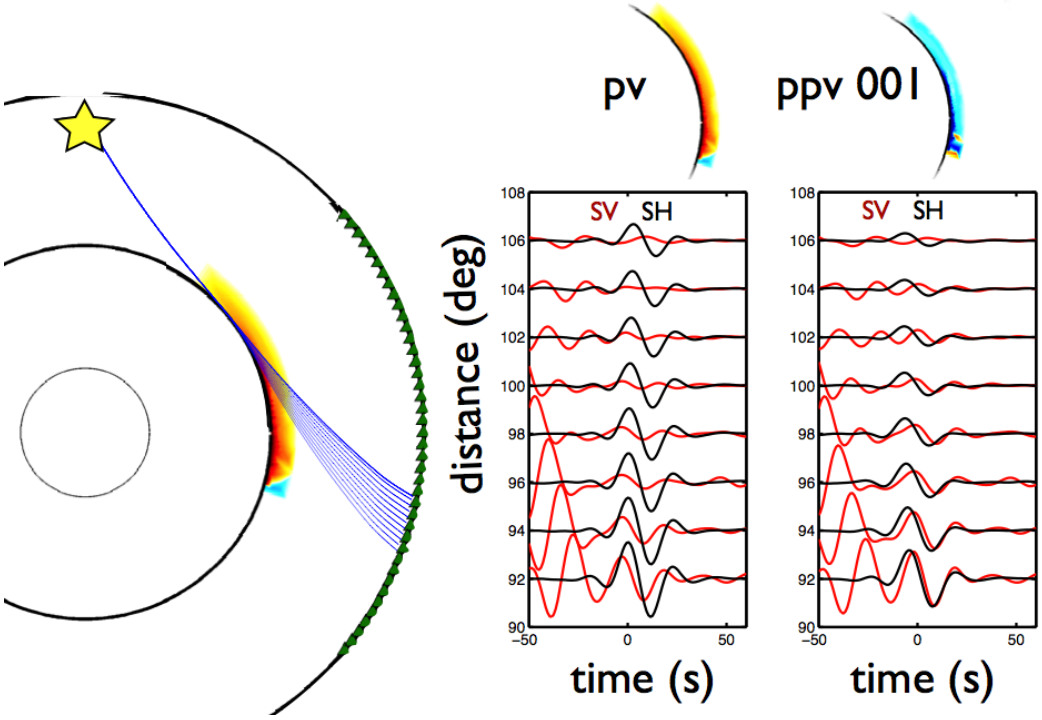

Figure 5.13: Synthetic waveforms as a function of distance between 92 and 106° for the models with Pv and pPv_1^C (001). The left panel shows the implementation of the model and example S_{diff} rays (in blue). Radial anisotropy is plotted with the same color scale as Figure 5.11. SH component is in black, SV component in red. Waveforms are aligned on the predicted S_{diff} arrival. Energy on the SV before the S_{diff} is the SKS and SKKS phase.

5.3.1.4 Synthetic waveforms

Synthetic waveforms are computed with CSEM (see Section 5.2.3.1) and presented in Figure 5.13. Note that to do this we only consider the anisotropic part of the model on top of the 1D radial model PREM, and disregard the isotropic velocity variations in our model. We consider the models for Pv and for pPv_1^C as two cases with opposite radial anisotropy signatures. The $S(_{diff})$ wave behaves as expected, the SH component is faster than the SV for pPv_1^C, and the opposite is true for Pv. The travel time differences are measurable at distances of 92°, but quickly increase with distance to more than 10 seconds. From the amplitudes we see two characteristics of shear diffracted waves: the SH component propagates more effectively than the SV component and both components propagate more effectively when the shear velocities are slow. This results in stronger SH amplitudes in the model for Pv, and strong SV amplitudes for pPv_1^C. The waveforms for pPv_1^C are consistent with typical observations beneath Alaska, where slab material might be present (Garnero and Lay, 1997)

5.3.2 3D geodynamical model

5.3.2.1 Comparing radial anisotropy between 3D and 2D

Our first test for the 3D geodynamical model is to confirm the results of the 2D geodynamical model, and validate our assumption that a slab can be simplified to a 2D case. In Figure 5.14 the computed S and P wave anisotropies as a function of propagation direction for a single location are plotted. These can be directly compared to those for the 2D model in Figure 5.12. The patterns of anisotropy are the same, but less strongly developed. The amount of anisotropy is smaller in our 3D model, because the location is not as far along the core-mantle boundary. We compute the deformation in the tracers until they start turning up again. In our 3D model, the tracers start to interact with an upwelling not far from where the slab subducts. We stop modeling the deformation when the tracer interacts with the upwelling.

We calculated the P and S wave radial anisotropy at many locations along the tracers. These values are plotted in Figures 5.15-5.18 for the different compositions at the tracer locations. The views are on the top and bottom of the slab; the slab is shown between colatitudes of 100 and 60°. At the furthest edge of the slab, the slab bends inwards, due to the boundary of the geodynamical model and the geometrical compression as it subducts. The signature of radial anisotropy often switches in this region. To avoid this problem, the slab will only cover half the width of the domain in our next model.

In the center of the subducting slab, the signatures are the same as in our 2D case. Pv signature of $V_{SV}>V_{SH}$ is consistent with the 2D case, but inconsistent with seismic observations. While the model of pPv_1^C shows $V_{SH}>V_{SV}$ and the opposite signature in P-wave radial anisotropy. Interestingly, the switch of signature for the pPv_1^A case with depth persists here too. The assumption that a 2D model correctly captures the behavior of a slab is validated.

5.3.2.2 Shear wave splitting

Seismic core phases, SK(K)S, propagate nearly vertically in the mantle and are therefore sensitive to a fast axis in the horizontal plane, i.e. azimuthal anisotropy. Differential splitting observations in SKS and SKKS phases have shown the presence of small scale lateral variations in anisotropy (Long, 2009; Lynner and Long, 2012). Here we evaluate the azimuthal anisotropy in our model. Figure 5.19 shows the fast axis of azimuthal anisotropy scaled to the strength of azimuthal anisotropy along 10% of the tracers in the lowermost 300 km. We only plot 1/5 of the data points along the tracer, and only if they cross a threshold of 0.5% anisotropy. For Pv, the least amount of points reach this threshold. We see that the model with Pv results in a fast axis direction orthogonal to the slab, and parallel to the slab subduction direction. The fast axis directions for all three pPv models are almost parallel to the slab. pPv_1^A appears most scattered, which can be due to strong variations in

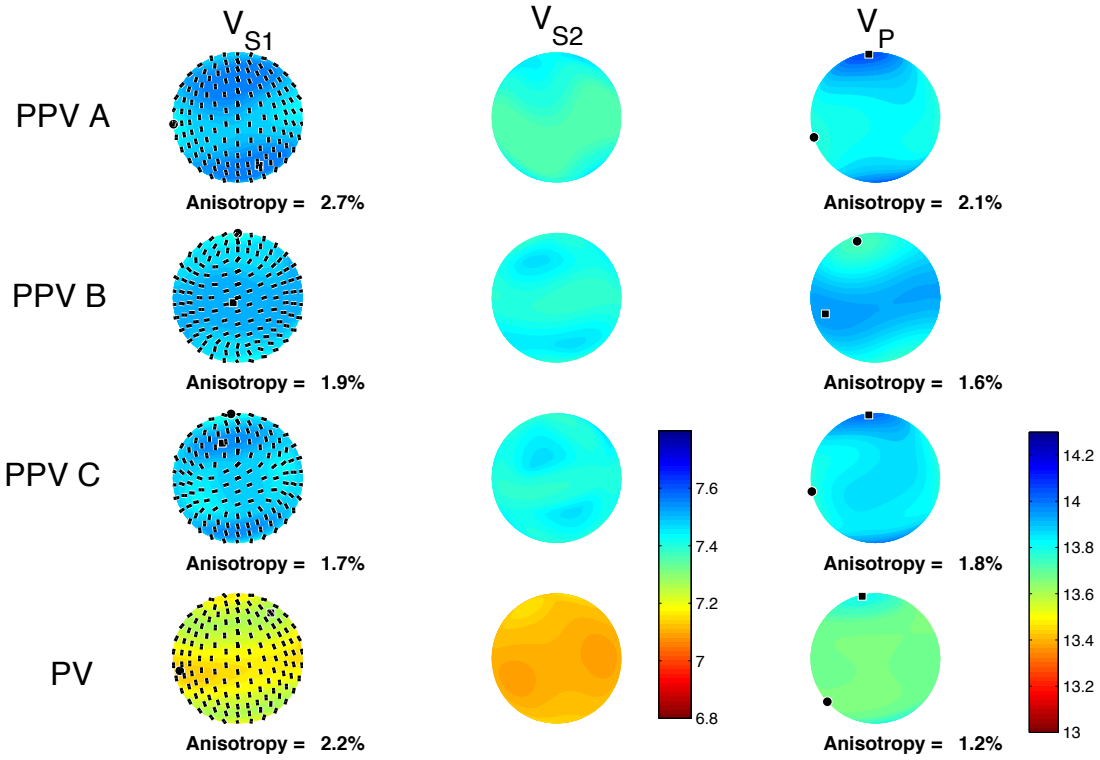

Figure 5.14: Fast and slow shear velocity (km/s), and compressional wave velocity (km/s) as a function of propagation direction at a single location (at time step 1925 along tracer 1312). Compositional models are MgO mixed with Pv, pPv_1^A, $\mathrm{pPv}_1^B$and pPv_1^C (from top to bottom). The horizontal axis is the core-mantle boundary. Black lines indicate the fast polarization direction.

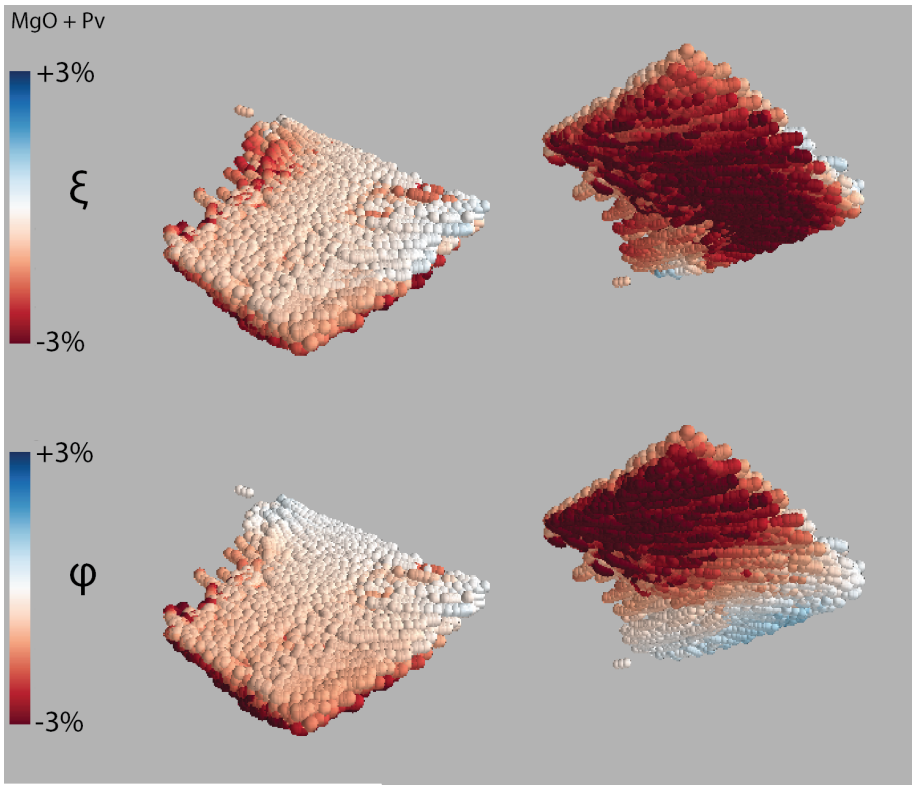

Figure 5.15: Transverse isotropic development at every time step along the tracers within the slab for a mixture of Pv and MgO. Slab is viewed from above (left) and below (right) for shear wave radial anisotropy (top) and compressional wave radial anisotropy (bottom).

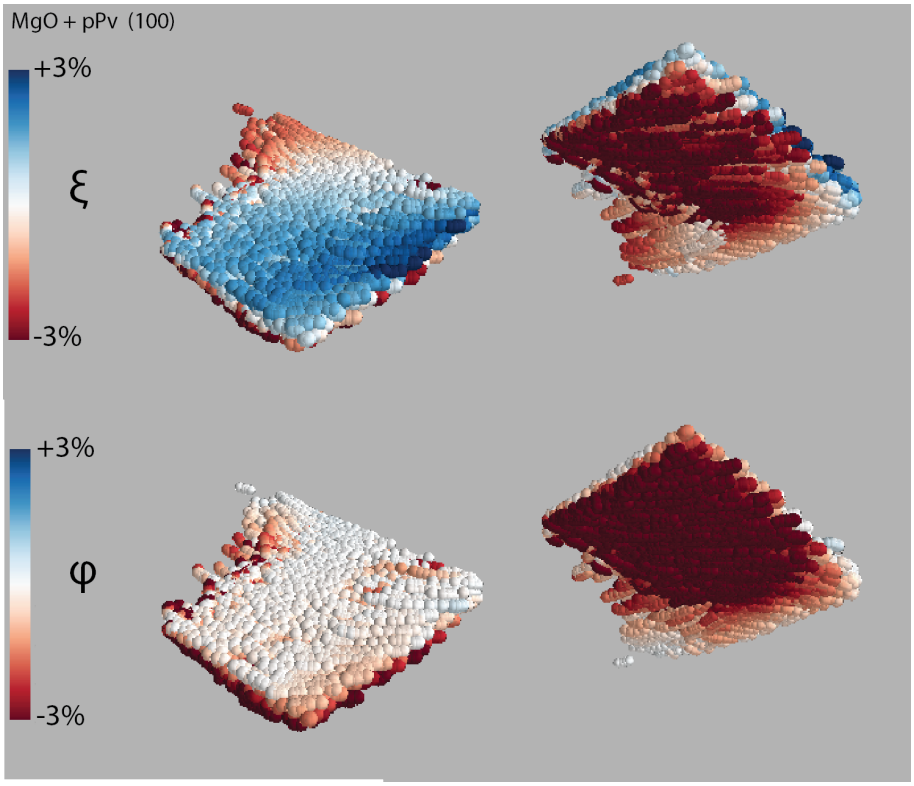

Figure 5.16: Transverse isotropic development at every time step along the tracers within the slab for a mixture of pPv_1^A and MgO. Slab is viewed from above (left) and below (right) for shear wave radial anisotropy (top) and compressional wave radial anisotropy (bottom).

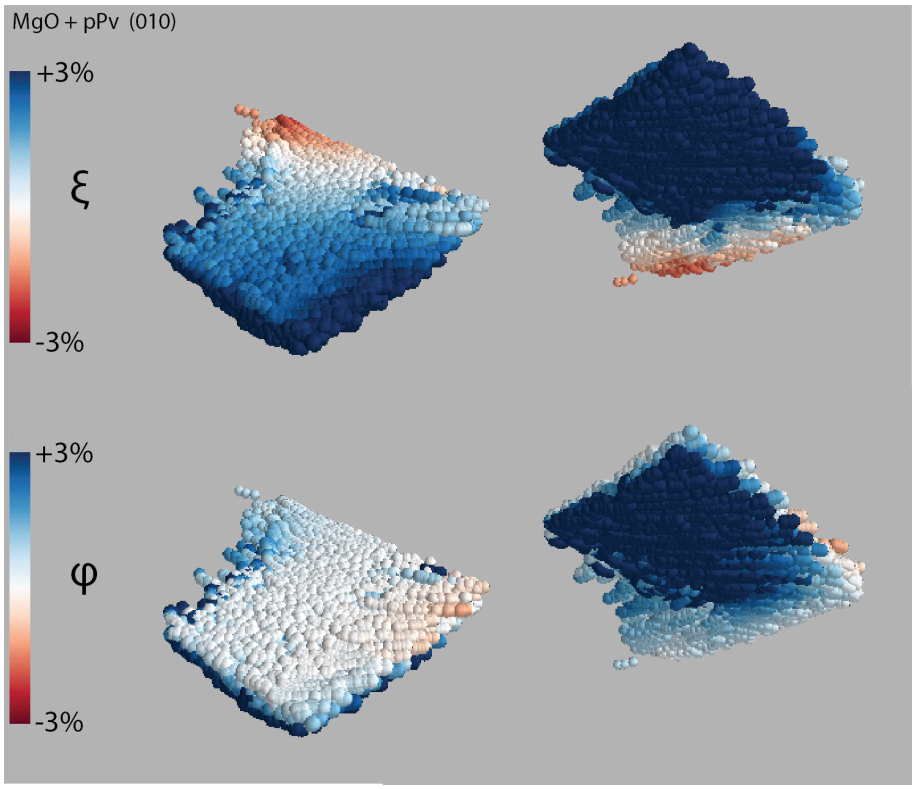

Figure 5.17: Transverse isotropic development at every time step along the tracers within the slab for a mixture of pPv_1^B and MgO. Slab is viewed from above (left) and below (right) for shear wave radial anisotropy (top) and compressional wave radial anisotropy (bottom).

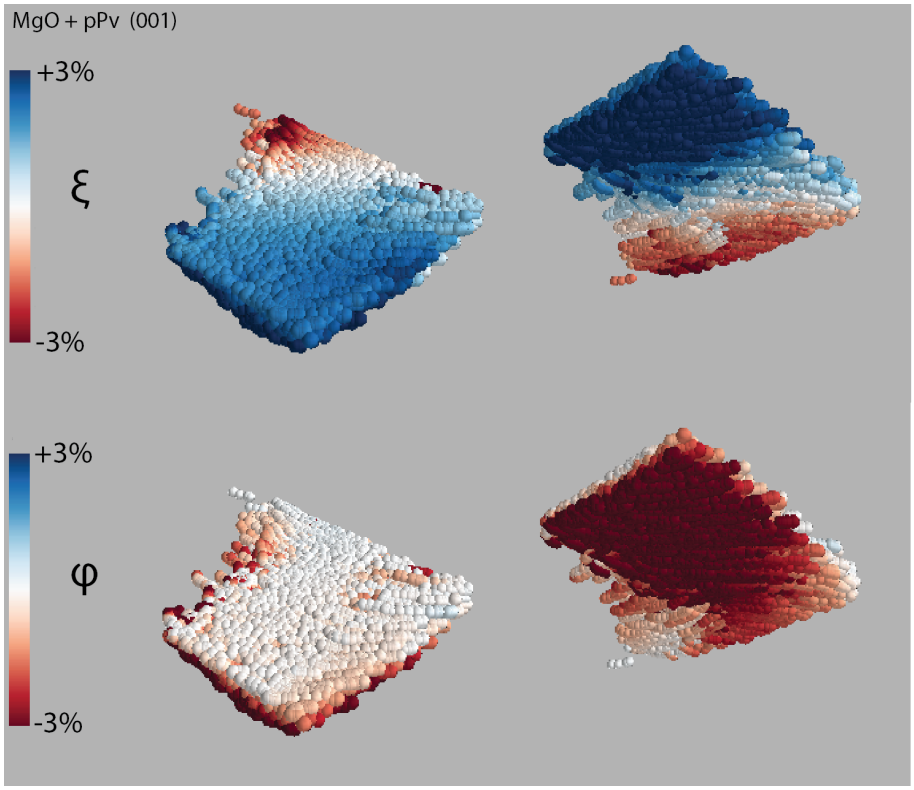

Figure 5.18: Transverse isotropic development at every time step along the tracers within the slab for a mixture of $\mathrm{pPv}_{\mathrm{I}}^{C}$ and MgO. Slab is viewed from above (left) and below (right) for shear wave radial anisotropy (top) and compressional wave radial anisotropy (bottom).

depth as seen in the radial anisotropy (Figure 5.16). Consistently with the 2D model, pPv_1^C has the strongest azimuthal anisotropy. However, none of these models develop anisotropy much stronger than 1%, and even though it extends over 300 km, the integrated splitting time will still be less than 0.5 second and thus difficult to detect in seismic phases.

Note that coverage of the fast axis directions outline the slab. This is not to say that there is no anisotropy outside the slab and a sharp contrast in anisotropy exists, but we have no tracers outside the slab and thus no knowledge of the deformational history of the material there.

It is also interesting to look at splitting in waves that cross the slab (Figure 5.20) compared to those that propagate parallel to the slab (Figure 5.21). Shear waves crossing the slab see different splitting patterns for the different compositions. Between colatitudes of 115 and 70° in Figure 5.20, the center of the slab shows little splitting for Pv and pPv_1^A, while stronger horizontal fast axes are seen for pPv_1^B and pPv_1^C. These results appear consistent with the mean radial anisotropic component. The tilt of the fast axis changes for most models at the edges of the slab. Results at the edges also appear more scattered. Only pPv_1^C appears horizontally fast all the way across.

Interestingly, pPv_1^C is the model that changes most strikingly for shear waves traveling in the N-S direction (Figure 5.21). Overall the fast axis in this direction is vertical for Pv, pPv_1^A and pPv_1^B. The fast axis is only consistently horizontal in crossing rays for pPv_1^B. In the radial anisotropic model for pPv_1^C we have seen that, on average, the horizontal component is fast (Figure 5.18).

Similar to azimuthal anisotropy, the tilted anisotropy both in E-W and N-S direction is weak. It remains to be seen in future synthetic full waveform modeling work if these models can be distinguished seismically and linked to actual seismic observations.

5.4 Discussion

A number of assumptions go into modeling LPO anisotropy in the lowermost mantle. Here we discuss the major ones.

Our geodynamical models include assumptions on the viscosity of the slabs. The slabs in the geodynamical models basically turn onto the core-mantle boundary with little buckling or ponding. Even though we assume the presence of pPv in our models, we do not take the effect of a Pv to pPv transition into the geodynamical models (Nakagawa and Tackley, 2011). Besides the thermodynamic effects of the transition itself, pPv is also predicted to be more viscous (Ammann et al., 2010). One other major drawback of the geodynamical modeling is the lack of thermo-chemical piles that represent the LLSVPs, although a lot is still unknown about them (McNamara and Zhong, 2005; Lassak et al., 2007; Li and McNamara, 2013). This prevents us from interpreting the regions of upwelling in our geodynamical

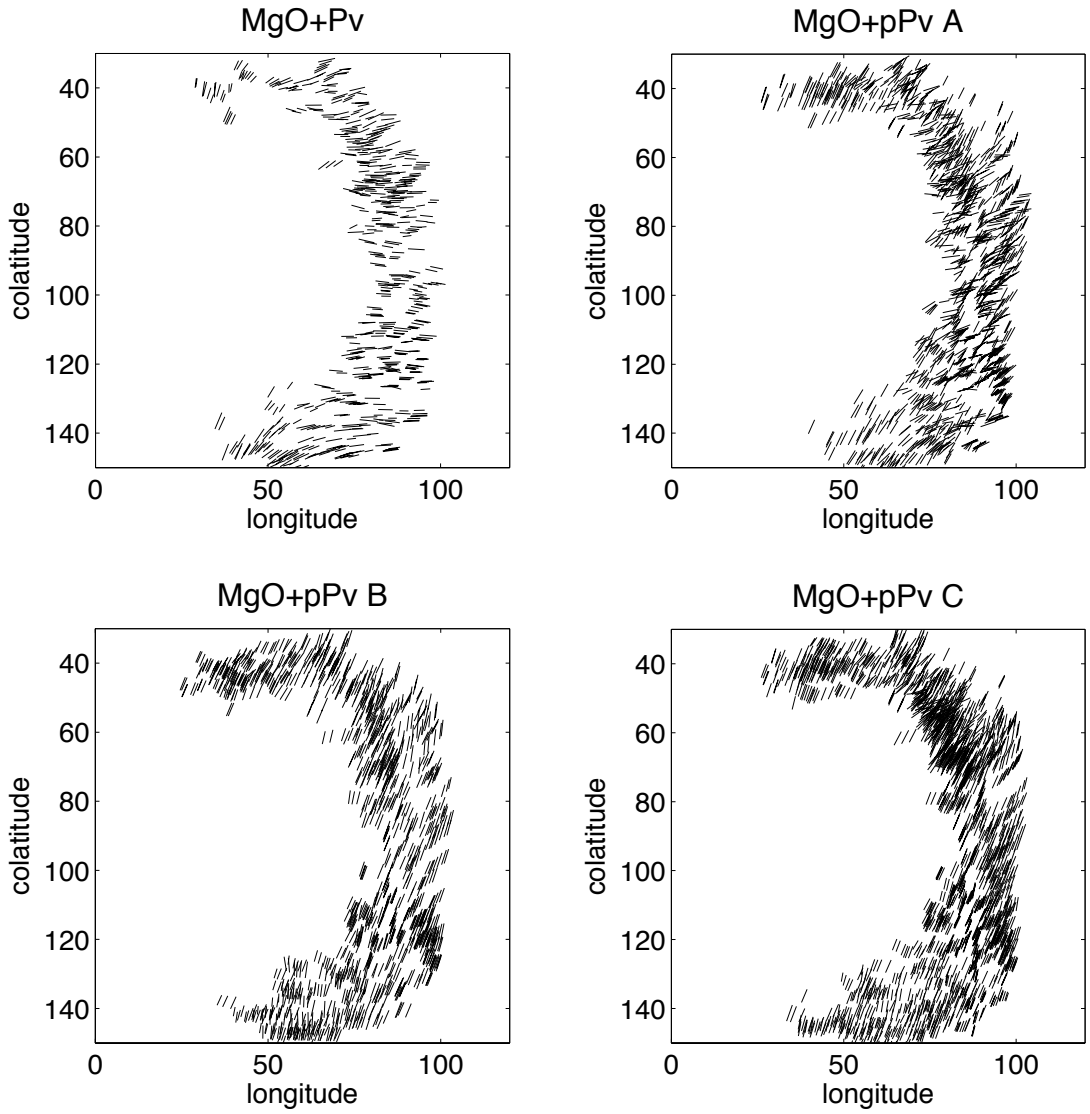

Figure 5.19: Fast axes of azimuthal anisotropy (i.e. splitting for shear waves traveling vertically) in the downwelling slab. Panels show fast axis direction for MgO mixed with Pv, pPv_1^A, pPv_1^B and pPv_1^C. Data coverage outlines the slab, and we lack knowledge of the deformational history of material outside this region.

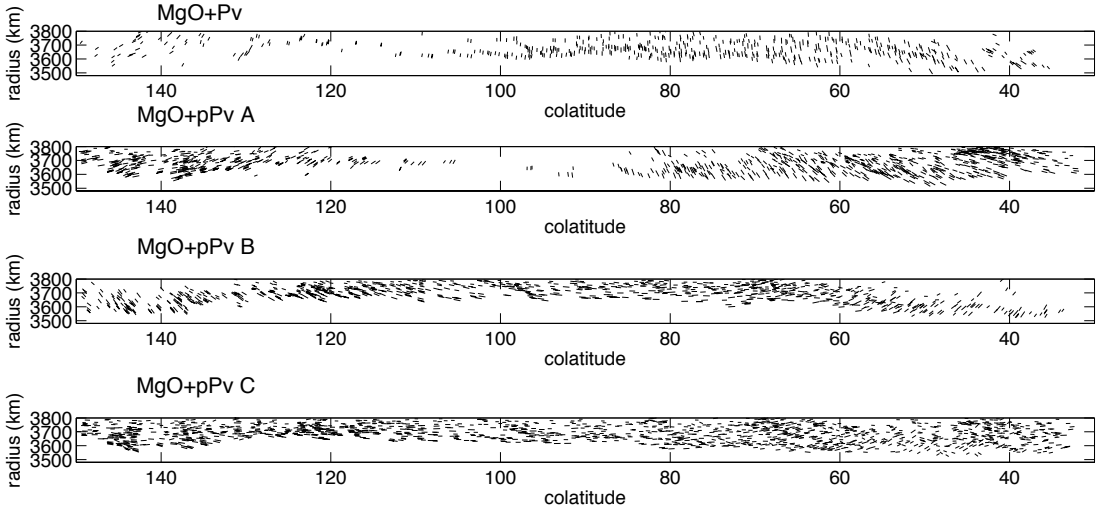

Figure 5.20: Fast axes of tilted anisotropy for shear waves propagating in the E-W direction crossing through the downwelling slab. Panels show fast axis direction for MgO mixed with Pv, pPv_1^A, pPv_1^B and pPv_1^C.

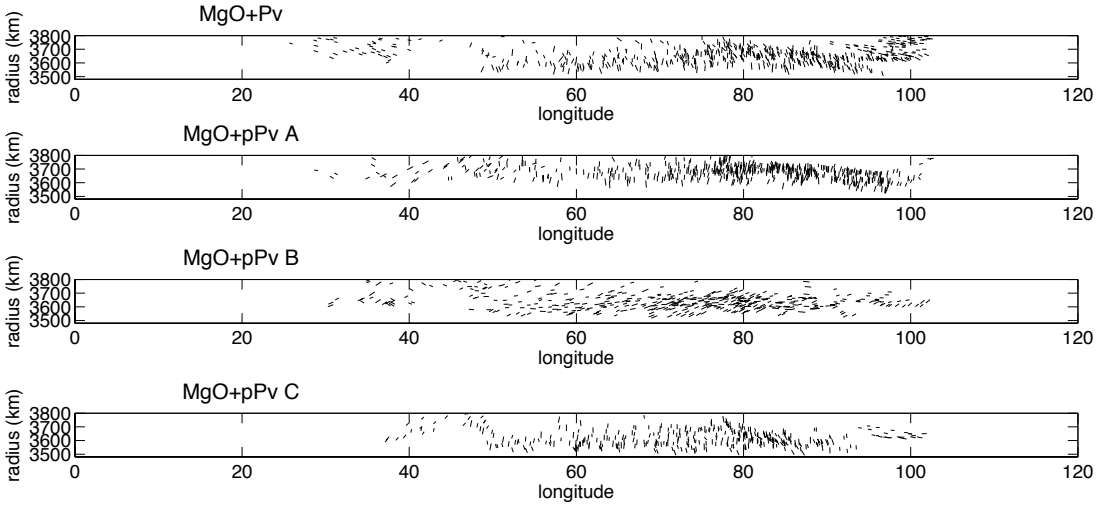

Figure 5.21: Fast axes of tilted anisotropy for shear waves propagating in the N-S direction propagating parallel to the slab. Panels show fast axis direction for MgO mixed with Pv, pPv_1^A, pPv_1^B and pPv_1^C.

model, as well as seismic observations around the LLSVPs.

Dislocation creep is the main mechanism to create LPO anisotropy. Whether dislocation creep is actually the main deformation mechanism in a subducting slab and the rest of the D″ remains a question. McNamara et al. (2001) model deformation regimes in a geodynamical model. Their modeling of rheology by dislocation and diffusion creep is based on empirical results from mineral physics experiments. The activities in both deformation mechanisms depend on temperature, grain size, stress and empirical constants. Their results show that dislocation creep could dominate in regions of downwelling, while the rest of the lower mantle is dominated by diffusion creep. This could explain the localization of anisotropy in regions where slab material could be present.

We assume pure Mg–Si–O phases and do not consider the influence of Fe-content or Ca-phases such as $CaSiO_3$ perovskite. This assumption leads to incorrect absolute velocities. The absolute velocities for perovskite lie closest to the PREM values of ∼7.2 km/s for S-waves and ∼13.65 km/s for P-waves (Dziewonski and Anderson, 1981), whereas for post-perovskite, velocities for Stackhouse et al., 2005 are higher than PREM. Results for Wentzcovitch et al. (2006) lie closer to PREM. However, the velocities are not directly comparable, as first-principle calculations are for infinite frequency, while seismic frequencies are sensitive to physical dispersion due to anelasticity. Physical dispersion lowers the intrinsic velocity at lower frequencies. Additionally, the densities used in these calculations (from first principles) are also lower than PREM (resulting in higher velocities). Inclusion of Fe could increase the densities and lower the velocities. How Fe-content can change the main slip systems also remains to be seen.

In the 2D model, we have seen strong anisotropy, while the 3D model has weak anisotropy. Is the anisotropy in the 2D model too strong? The anisotropy which is observed, e.g. in the Caribbean and under Alaska ($\xi_{max} = 1.04$, Figure 5.1) is smaller than the predictions of the model (ξ_{max}=1.35, $\xi_{mean} = 1.05$) which could be due to the underestimation of seismic anisotropy by averaging over long paths in the seismic data, especially in global models, or the overestimation of the amount of dislocation creep versus diffusion creep.

Other recent studies have followed a comparable approach. Walker et al. (2011) compute LPO anisotropy in 3D global flow models, which are based on a joint inversion of isotropic shear wave velocities and other geophysical constraints. After modeling LPO anisotropy along their tracers, they can calculate correlation coefficients between their global LPO anisotropic models and global models of shear radial anisotropy. Their correlation coefficients are mostly positive for pPv_1^A and pPv_1^B while pPv_1^C is mostly anti-correlated. They mention that this correlation results from regions under the Pacific and Africa where $V_{SV} > V_{SH}$ which correlate with strong horizontal flows in their model. Whether these are the regions of strong horizontal flow in the Earth remains a question. Their flow models, similar to ours, do not contain thermo-chemical piles. These piles might change the regions of $V_{SV} > V_{SH}$ into regions of upwelling. As the authors also mention, depending on the Clapeyron slope of the Pv to pPv transition, pPv might not be present in these warmer

regions and the anisotropic signature of Pv would be consistent with seismic observations. Additionally, the anisotropy seen beneath Pacific and Africa is weak, and might be apparent anisotropy due to the strong slow heterogeneity seen within and at the borders of these piles (e.g. Lay et al., 2006; He and Wen, 2009; Thorne et al., 2013, and Chapter 2). We focus our conclusions on regions of strong observed anisotropy in cold regions where pPv is most likely to be present (e.g. Alaska).

Walker et al. (2011) correlate the P wave radial anisotropy component with the global model of Soldati et al. (2003).There is very little correlation with this model. Even modeling isotropic P wave variations in the lowermost mantle is difficult (Li and van der Hilst, 2008; Simmons et al., 2012), while for P wave anisotropy one needs good coverage of vertical and horizontal crossing rays. Here we have focused our conclusion on the observation based on normal modes of Beghein et al. (2006) that S wave anisotropy is probably anti-correlated with P-wave anisotropy in the lowermost mantle.

While Walker et al. (2011) are not able to distinguish between pPv^A and pPv^B, Nowacki et al. (2013) continue to use direct observations of ScS splitting in paleosubducted regions to constrain a better fit with pPv^B over the other two models. This is a first link between direct seismic observations and these types of models. Correlation, however, is still very scattered and strongly depends on the geodynamical model being representative of the region.

The final word has not been said on the LPO anisotropy in the lowermost mantle. So far most studies have focused on three deformational models of pPv (Table 5.1), but others might be found. It is exciting to see that the differences in microscopic deformation result in different signatures at seismically observable scales.

5.5 Conclusions

Significant strains in the downwelling slabs combined with the sufficient intrinsic anisotropy in (post)-perovskite can result in seismically measurable anisotropy patterns. Interestingly, the microscopic deformation behavior of minerals can lead to different patterns on the macroscopic scales. We find that a mixture of perovskite and periclase results in inconsistent signature in radial anisotropy for S waves compared to seismic observations of $V_{SH} > V_{SV}$ beneath slab regions. For pPv, the signature varies with the most dominant slip plane. Postperovskite with a main slip plane of (001) (pPv^C) results in consistent radial anisotropy for S waves, as well as an opposite signature in radial anisotropy for P waves. A main slip plane of (010) (pPv^B) also shows consistent shear wave radial anisotropy, but is weaker in strength. Shear wave splitting with suitable crossing rays can further distinguish between these compositional models.

On the one hand this means that pPv would need to be present in the D″ to explain the anisotropy through lattice preferred orientation. An additional argument for that is that pPv can account for stronger variations in isotropic velocity, as also seen in the D″.

On the other hand, it shows that measuring dislocation creep behavior in DIA experiments is tricky and should be done with care. The experiments resulting in different dominant slip planes might have been caused by the use of analog materials or the interpretation of false patterns in phase transformations.

5.6 Acknowledgements

A number of the calculations and figures are done with help of the MSAT Matlab package (www1.gly.bris.ac.uk/MSAT/). This work was supported by NSF/CSEDI grant 1067513 and ERC grant 'WAVETOMO'.

Bibliography

Ammann, M., Brodholt, J., Wookey, J., Dobson, D., 2010. First-principles constraints on diffusion in lower-mantle minerals and a weak D" layer. Nature 465, 462–465.

Babuska, V., Cara, M., 1991. Seismic anisotropy in the Earth. Kluwer Academic Publishers.

Becker, T., Kustowski, B., Ekström, G., 2008. Radial seismic anisotropy as a constraint for upper mantle rheology. Earth Plan. Sci. Lett 267 (1), 213–227.

Beghein, C., Trampert, J., Heijst, H. V., 2006. Radial anisotropy in seismic reference models of the mantle. J. Geophys. Res 111 (B2), 1–9.

Capdeville, Y., Larmat, C., Vilotte, J. P., Montagner, J. P., 2002. A new coupled spectral element and modal solution method for global seismology- A first application to the scattering induced by a plume-like anomaly. Geophys. Res. Lett. 29, 1318–1322.

Capdeville, Y., To, A., Romanowicz, B., 2003. Coupling spectral elements and modes in a spherical Earth: an extension to the 'sandwich' case. Geophys. J. Int. 154 (1), 44–57.

Catalli, K., Shim, S., Prakapenka, V., 2009. Thickness and Clapeyron slope of the post-perovskite boundary. Nature 462 (7274), 782–785.

Chaljub, E., Capdeville, Y., Vilotte, J., 2003. Solving elastodynamics in a fluidsolid heterogeneous sphere: a parallel spectral element approximation on non-conforming grids. J. Compu. Phys. 158 (1), 131–141.

Cobden, L., Goes, S., Cammarano, F., Connolly, J., 2008. Thermochemical interpretation of onedimensional seismic reference models for the upper mantle: evidence for bias due to heterogeneity. Geophys. J. Int 175 (2), 627–648.

Eshelby, J., 1957. The determination of the elastic field of an ellipsoidal inclusion, and related problems. Proceedings of the Royal Society of London 241 (1226), 376–396.

Faccioli, E., Maggio, F., Paolucci, R., Quarteroni, A., 1997. 2D and 3D elastic wave propagation by a pseudo-spectral domain decomposition method. J. Seismol. 1 (3), 237–251.

Ford, S., Garnero, E., McNamara, A., 2006. A strong lateral shear velocity gradient and anisotropy heterogeneity in the lowermost mantle beneath the southern Pacific. J. Geophys. Res: Solid Earth 111 (B3).

Garnero, E., Lay, T., 1997. Lateral variations in lowermost mantle shear wave anisotropy. J. Geophys. Res 102, 8121–8135.

Garnero, E., Maupin, V., Lay, T., Fouch, M., 2004. Variable azimuthal anisotropy in Earth's lowermost mantle. Science 306 (5694), 259–261.

Grocholski, B., Catalli, K., Shim, S., Prakapenka, V., 2012. Mineralogical effects on the detectability of the postperovskite boundary. P Natl Acad Sci 109 (7), 2275–2279.

He, Y., Wen, L., 2009. Structural features and shear-velocity structure of the Pacific Anomaly. J. geophys. Res 114, B02309.

Hirose, K., Karato, S., 2006. Unsolved problems in the lowermost mantle. Geophys. J. Int. 33 (12).

Iitaka, T., Hirose, K., Kawamura, K., Murakami, M., 2004. The elasticity of the MgSiO3 post-perovskite phase in the Earth's lowermost mantle. Nature 430 (6998), 442–445.

Karato, S., 1998a. Seismic anisotropy in the deep mantle, boundary layers and the geometry of mantle convection. Geodynamics of Lithosphere & Earth's Mantle, 565–587.

Karato, S., 1998b. Some remarks on the origin of seismic anisotropy in the D" layer. Earth Plan. Space 50, 1019–1028.

Karato, S., Zhang, S., Wenk, H., 1995. Superplasticity in Earth's lower mantle: Evidence from seismic anisotropy and rock physics. Science 270 (5235), 458–461.

Karki, B., Wentzcovitch, R., Gironcoli, S. D., Baroni, S., 2000. Ab initio lattice dynamics of MgSiO3 perovskite at high pressure. Physical Review B 62 (22), 14750.

Kawai, K., Geller, R. R. J., Aug. 2010. The vertical flow in the lowermost mantle beneath the Pacific from inversion of seismic waveforms for anisotropic structure. Earth Plan. Sci. Lett 297 (1-2), 190–198.

Kendall, J., 2000. Seismic anisotropy in the boundary layers of the mantle. Geoph. Monogr. AGU 117, 133–160.

Kendall, J., Silver, P., 1996. Constraints from seismic anisotropy on the nature of the lowermost mantle. Nature 381 (6581), 409–412.

Kendall, J., Silver, P., 1998. Investigating causes of D" anistropy. Geodynamics Series 28, 97–118.

Komatitsch, D., Tromp, J., 1999. Introduction to the spectral element method for threedimensional seismic wave propagation. Geophys. J. Int 139 (3), 806–822.

Komatitsch, D., Tromp, J., 2002. Spectralelement simulations of global seismic wave propagationII. Threedimensional models, oceans, rotation and selfgravitation. Geophys. J. Int 150 (1), 303–318.

Komatitsch, D., Vilotte, J., 1998. The spectral element method: An efficient tool to simulate the seismic response of 2D and 3D geological structures. BSSA 88 (2), 368–392.

Kustowski, B., Ekström, G., Dziewoski, A., 2008. Anisotropic shear-wave velocity structure of the Earth's mantle: a global model. J. Geophys. Res 113 (B6), B06306.

Lassak, T., McNamara, A., Zhong, S., 2007. Influence of thermochemical piles on topography at Earth's core-mantle boundary. Earth Planet. Sci. Lett. 261 (3), 443–455.

Lay, T., Garnero, E., 2007. Reconciling the post-perovskite phase with seismological observations of lowermost mantle structure. Geophys. Mono. Ser. -AGU 174, 129.

Lay, T., Hernlund, J., Garnero, E. J., Thorne, M. S., Nov. 2006. A post-perovskite lens and D" heat flux beneath the central Pacific. Science 314 (5803), 1272–6.

Lay, T., Williams, Q., Garnero, E. J., 1998. The core-mantle boundary layer and deep Earth dynamics. Nature 392 (6675), 461–468.

Lay, T., Young, C., 1991. Analysis of seismic SV waves in the core's penumbra. Geophys. Res. Lett. 18 (8), 1373–1376.

Lebensohn, R., 2007. Self-consistent modelling of the mechanical behaviour of viscoplastic polycrystals incorporating intragranular field fluctuations. Philosophical Magazine 87 (28), 4287–4322.

Lebensohn, R., Tomé, C., 1993. A self-consistent anisotropic approach for the simulation of plastic deformation and texture development of polycrystals: application to zirconium alloys. Acta Metallurgica et Materialia 41 (9), 2611–2624.

Li, C., van der Hilst, R., 2008. A new global model for P wave speed variations in Earth's mantle. Geochem. Geophys. Geosyst. 9 (5).

Li, M., McNamara, A., 2013. The difficulty for subducted oceanic crust to accumulate at the Earth's core-mantle boundary. J. Geophys. Lett.: Solid Earth, in press.

Lin, J., Wenk, H., Voltolini, M., Speziale, S., Shu, J., Duffy, T., 2009. Deformation of lower-mantle ferropericlase (Mg, Fe) O across the electronic spin transition. Physics and Chemistry of Minerals 36 (10), 585–592.

Long, M., Becker, T., 2010. Mantle dynamics and seismic anisotropy. Earth Plan. Sci. Lett 297 (3), 341–354.

Long, M. D., Jun. 2009. Complex anisotropy in D beneath the eastern Pacific from SKSSKKS splitting discrepancies. Earth Plan. Sci. Lett 283 (1-4), 181–189.

Loubet, N., Ribe, N., Gamblin, Y., 2009. Deformation modes of subducted lithosphere at the core-mantle boundary: An experimental investigation. Geochem. Geophys. Geosyst 10 (10), Q10004.

Lynner, C., Long, M., 2012. Evaluating Contributions to SK(K)S Splitting from Lower Mantle Anisotropy: A Case Study from Station DBIC, Côte D'Ivoire. BSSA.

Masters, G., Laske, G., Bolton, H., Dziewonski, A., 2000. The relative behavior of shear velocity, bulk sound speed, and compressional velocity in the mantle: implications for chemical and thermal structure. Geoph. Monogr. AGU 117, 63–88.

Matas, J., Bukowinski, M. S. T., 2007. On the anelastic contribution to the temperature dependence of lower mantle seismic velocities. Earth Plan. Sci. Lett 259 (1-2), 51–65.

Matzel, E., Sen, M. K., Grand, S. P., 1996. Evidence for anisotropy in the deep mantle beneath Alaska. Geophys. Res. Lett. 23 (18), 2417.

Maupin, V., Dec. 1994. On the possibility of anisotropy in the D layer as inferred from the polarization of diffracted S waves. Phys. Earth Plan. Int 87 (1-2), 1–32.

Maupin, V., 2005. Azimuthal anisotropy in the D" layer beneath the Caribbean. J. Geophys. Res 110 (B8), 1–20.

McNamara, A. A. K., Karato, S. S.-I., van Keken, P., van Keken, P. E., Aug. 2001. Localization of dislocation creep in the lower mantle: implications for the origin of seismic anisotropy. Earth Plan. Sci. Lett 191 (1-2), 85–99.

McNamara, A. K., Zhong, S., May 2004. The influence of thermochemical convection on the fixity of mantle plumes. Earth Plan. Sci. Lett 222 (2), 485–500.

McNamara, A. K., Zhong, S., 2005. Thermochemical structures beneath Africa and the Pacific Ocean. Nature 7062, 1136–1139.

Merkel, S., Kubo, A., Miyagi, L., Spezile, S., Duffy, T., Mao, H., Wenk, H.-R., 2006. Plastic deformation of MgGeO3 post-perovskite at lower mantle pressures. Science 311 (5671), 644–646.

Merkel, S., McNamara, A., Kubo, A., Speziale, S., 2007. Deformation of (Mg, Fe) SiO3 post-perovskite and D"anisotropy. Science 316 (5832), 1729–1732.

Merkel, S., Wenk, H., Shu, J., Shen, G., Gillet, P., Mao, H. K., Hernley, R. J., 2002. Deformation of polycrystalline MgO at pressures of the lower mantle. J. Geophys. Res 101 (B11), 2271.

Miyagi, L., Kanitpanyacharoen, W., Kaercher, P., 2010. Slip Systems in MgSiO3 Post-Perovskite: Implications for D" Anisotropy. Science 329 (5999), 1639–1641.

Miyagi, L., Kanitpanyacharoen, W., Stackhouse, S., Militzer, B., Wenk, H.-R., 2011. The enigma of post-perovskite anisotropy: deformation versus transformation textures. Physics and Chemistry 38 (9), 665–678.

Miyagi, L., Merkel, S., Yagi, T., Sata, N., Ohishi, Y., Wenk, H., 2009. Diamond anvil cell deformation of CaSiO 3 perovskite up to 49GPa. Phys. Earth Plan. Int 174 (1), 159–164.

Miyajima, N., Walte, N., 2009. Burgers vector determination in deformed perovskite and post-perovskite of CaIrO 3 using thickness fringes in weak-beam dark-field images. Ultramicroscopy 109 (6), 683–692.

Molinari, A., Canova, G., Ahzi, S., 1987. A self consistent approach of the large deformation polycrystal viscoplasticity. Acta Metallurgica 35 (12), 2893–2994.

Moore, M. M., 2004. Shear wave splitting and waveform complexity for lowermost mantle structures with low-velocity lamellae and transverse isotropy. J. Geophys. Res 109 (B2), 1–26.

Moresi, L., Zhong, S., Gurnis, M., 1996. The accuracy of finite element solutions of Stokes's flow with strongly varying viscosity. Phys. Earth Plan. Int 97 (1), 83–94.

Murakami, M., Hirose, K., Kawamura, K., Sata, N., Ohishi, Y., 2004. Post-perovskite phase transition in MgSiO3. Science 304 (5672), 855–858.

Murakami, M., Ohishi, Y., Hirao, N., Hirose, K., 2012. A perovskitic lower mantle inferred from high-pressure, high-temperature sound velocity data. Nature 285 (7396), 90–94.

Nakagawa, T., Tackley, P., 2005. Deep mantle heat flow and thermal evolution of the Earth's core in thermochemical multiphase models of mantle convection. Geochem., Geophys., Geosyst. 6 (Q08003).

Nakagawa, T., Tackley, P., 2011. Effects of low-viscosity post-perovskite on thermo-chemical mantle convection in a 3-D spherical shell. Geophys. Res. Lett. 38 (4), L04305.

Ni, S., Tan, E., Gurnis, M., Helmberger, D., 2002. Sharp sides to the African superplume. Science 296 (5574), 1850–1853.

Nowacki, A., Walker, A., Wookey, J., Kendall, J., 2013. Evaluating post-perovskite as a cause of D" anisotropy in regions of palaeosubduction. Geophys. J. Int. 192 (3), 1085–1090.

Nowacki, A., Wookey, J., Kendall, J., 2010. Deformation of the lowermost mantle from seismic anisotropy. Nature 467 (7319), 1091–1094.

Nowacki, A., Wookey, J., Kendall, J.-M. J., Oct. 2011. New advances in using seismic anisotropy, mineral physics and geodynamics to understand deformation in the lowermost mantle. J. Geodyn. 52 (3-4), 205–228.

Okada, T., Yagi, T., Niwa, K., Kikegawa, T., 2010. Lattice-preferred orientations in post-perovskite-type MgGeO 3 formed by transformations from different pre-phases. Phys. Earth Plan. Int 180 (3), 195–202.

Panning, M., Romanowicz, B., 2006. A three-dimensional radially anisotropic model of shear velocity in the whole mantle. Geophys. J. Int. 167 (1), 361–379.

Richards, P. G., 1976. On the adequacy of plane-wave reflection/transmission coefficients in the analysis of seimsic body waves. Seismological Society of America 66 (3), 701–717.

Rokosky, J. M., Lay, T., Garnero, E. J., Aug. 2006. Small-scale lateral variations in azimuthally anisotropic D structure beneath the Cocos Plate. Earth Plan. Sci. Lett 248 (1-2), 411–425.

Russell, S., Lay, T., Garnero, E., 1998. Seismic evidence for small-scale dynamics in the lowermost mantle at the root of the Hawaiian hotspot. Nature 396 (6708), 255–258.

Sidorin, I., Gurnis, M., Helmberger, D., Ding, X., 1998. Interpreting D seismic structure using synthetic waveforms computed from dynamic models. Earth Plan. Sci. Lett 163 (1), 31–41.

Simmons, N., Myers, S., Johanneson, G., Matzel, E., 2012. LLNL-G3Dv3: Global P wave tomography model for improved regional and teleseismic travel time prediction. J. Geophys. Res.: Solid Earth 117 (B10).

Soldati, G., Boschi, L., Piersanti, A., 2003. Outer core density heterogeneity and the discrepancy between PKP and PcP travel time observations. Geophys. Res. Lett. 30 (4), 1190.

Stackhouse, S., Brodholt, J., 2007. The high-temperature elasticity of MgSiO3 post-perovskite. Geophysical Monograph Series 174, 99–114.

Stackhouse, S., Brodholt, J. P., Wookey, J., Kendall, J.-M., Price, G. D., Jan. 2005. The effect of temperature on the seismic anisotropy of the perovskite and post-perovskite polymorphs of MgSiO3. Earth Plan. Sci. Lett 230 (1-2), 1–10.

Stretton, I., Heidelbach, F., Mackwell, S., Langenhorst, F., 2001. Dislocation creep of magnesiowüstite (Mg_{0.8} Fe_{0.2} O). Earth and Planetary . . . 194 (1), 229–240.

Su, W.-j., Dziewonski, A. M., Mar. 1997. Simultaneous inversion for 3-D variations in shear and bulk velocity in the mantle. Phys. Earth Plan. Int 100 (1-4), 135–156.

Tan, E., Choi, E., Thoutireddy, P., Gurnis, M., Aivazis, M., 2006. GeoFramework: Coupling multiple models of mantle convection within a computational framework. Geochem. Geophys. Geosyst 7 (6), Q06001.

Thorne, M., Garnero, E., Jahnke, G., Igel, H., McNamara, A., 2013. Mega ultra low velocity zone and mantle flow. Earth Plan. Sci. Lett 364, 59–67.

Tkalčić, H., Romanowicz, B., 2002. Short scale heterogeneity in the lowermost mantle: insights from PcP-P and ScS-S data. Earth Plan. Sci. Lett 201 (1), 57–68.

To, A., Romanowicz, B., 2009. Finite frequency effects on global S diffracted traveltimes. Geophys. J. Int. 179 (3), 1645–1657.

To, A., Romanowicz, B., Capdeville, Y., Takeuchi, N., 2005. 3D effects of sharp boundaries at the borders of the African and Pacific Superplumes: Observation and modeling. Earth Plan. Sci. Lett. 233 (1-2), 1447–1460.

Tsuchiya, T., Tsuchiya, J., Umernote, K., Wentzcovitch, R., 2004. Phase transition in MgSiO 3 perovskite in the Earth's lower mantle. Earth Plan. Sci. Lett 224 (3), 241–248.

Vinnik, L., Breger, L., Romanowicz, B., 1998. Anisotropic structures at the base of the Earth's mantle. Nature 393 (6685), 564–567.

Vinnik, L., Farra, V., Romanowicz, B., 1989. Observational evidence for diffracted SV in the shadow of the Earth's core. Geophys. Res. Lett. 16 (6), 519–522.

Vinnik, L., Romanowicz, B., Le Stunff, Y., Makeyeva, L., 1995. Seismic anisotropy in the D layer. Geophysical research ... 22 (13), 16571660.

Walker, a. M., Forte, a. M., Wookey, J., Nowacki, a., Kendall, J.-M., Oct. 2011. Elastic anisotropy of D predicted from global models of mantle flow. Geochem. Geophys. Geosyst. 12 (10), 1–22.

Walte, N., Heidelbach, F., Miyajima, N., Frost, D., Rubie, C., 2009. Transformation textures in postperovskite: Understanding mantle flow in the D layer of the Earth. Geophys. Res. Lett. 36 (4).

Wenk, H., Lonardeli, I., Pehl, J., Devine, J., Prakapenka, V., Shen, G., Mao, H., 2004. In situ observation of texture development in olivine, ringwoodite, magnesiowüstite and silicate perovskite at high pressure. Earth Plan. Sci. Lett 226 (3), 507–519.

Wenk, H., Speziale, S., Mcnamara, a., Garnero, E., May 2006. Modeling lower mantle anisotropy development in a subducting slab. Earth Plan. Sci. Lett 245 (1-2), 302–314.

Wentzcovitch, R., 2010. Thermodynamic properties and phase relations in mantle minerals investigated by first principles quasiharmonic theory. Rev. Mineral. Geochem. 71 (1), 59–98.

Wentzcovitch, R., Karki, B., Cococcioni, M., de Gironcoli, S., Jan. 2004. Thermoelastic Properties of MgSiO3-Perovskite: Insights on the Nature of the Earths Lower Mantle. Phys. Rev. Lett 92 (1), 1–4.

Wentzcovitch, R. M., Tsuchiya, T., Tsuchiya, J., Jan. 2006. MgSiO3 postperovskite at D" conditions. P Natl Acad Sci of the United States of America 103 (3), 543–6.

Wookey, J., Helffrich, G., 2008. Inner-core shear-wave anisotropy and texture from an observation of PKJKP waves. Nature 454 (7206), 873–876.

Wysession, M., Langenhorst, A., Fouch, M., Fischer, K., 1999. Lateral variations in compressional/shear velocities at the base of the mantle. Science 284 (5411), 120–125.

Yamazaki, D., Karato, S., 2002. Fabric development in (Mg, Fe) O during large strain, shear deformation: implications for seismic anisotropy in Earth's lower mantle. Phys. Earth Plan. Int 131 (3), 251–267.

Zhong, S., Zuber, M. T., Moresi, L., Gurnis, M., 2000. Role of temperature-dependent viscosity and surface plates in spherical shell models of mantle convection. J. Geophys. Res. 105 (B5), 11063.

Chapter 6

Convection in the inner core

Over the past two decades arguments have been made for and against the occurrence of thermal convection in the inner core. Here we use numerical simulations of thermochemical convection to develop parameterized models for the thermal and chemical evolution of the inner core. A broad search of parameter values shows that thermal convection is feasible, particularly in the early stages of the inner core. For a thermal conductivity of 36 $\mathrm{Wm^{-1}K^{-1}}$, the minimum core-mantle boundary heat flux required for convection is $\sim$4.1 TW, corresponding to a maximum inner core age of 1.93 Gy. A heat flux greater than $\sim$6.3 TW (age $<$1.26 Gy) maintains convection in the inner core through present day. Changes in the concentration of light elements due to inner-core growth can also affect convection by producing a stable chemical stratification at the top of the inner core. Numerical simulations suggest that the concentration of light elements in the inner core is homogenized when the rate of entrainment exceeds the rate at which excess light is supplied through solidification. Representative results for the influence of light elements and a thermal conductivity of 36 $\mathrm{Wm^{-1}K^{-1}}$ imply that the inner core is convectively stable for heat flows below 4.3 TW or inner core ages older than 1.8 Gy. Convective velocities of several cm/yr are obtained for a nominal viscosity of 10^{18} Pa s, yielding strain rates of $10^{-15}\mathrm{s^{-1}}$. Calculations over a range of Rayleigh numbers, Ra, confirm that the convective velocities are proportional to $Ra^{1/2}$. Termination of convection at an early stage of evolution may provide an explanation for a distinct anisotropy in the innermost region of the inner core or a shallow isotropic layer.

6.1 Introduction

The center of the early Earth was too hot for solidification. As the Earth cooled an iron-rich solid began to crystallize at the center, forming the inner core (Jacobs, 1953). Estimates for the age of the inner core range from 0.5 Gy to 2.5 Gy (Labrosse et al., 2001). The current radius of the core is 1220 km, and consequently its volume is less than 1% of the entire Earth. The inner core consists of an iron-nickel alloy, mixed with some lighter

elements (Jephcoat and Olson, 1987). The concentration of light elements incorporated into the solid is uncertain, but it is probably less than the concentration of light elements in the surrounding liquid core (5-15% of its mass, (e.g. McDonough and Sun, 1995; Alfè et al., 2002)). Three phases of iron under core conditions have been proposed (Stixrude and Brown, 1998): fcc (face-centered cubic), bcc (body-centered cubic) and hcp (hexagonal close-packed). Hcp (Stixrude and Cohen, 1995; Tateno et al., 2010) or a mixed phase between hcp and fcc (Ishikawa et al., 2011) is thought to be most stable .

Observations of the inner core primarily come from seismology. Three-quarters of a century ago Lehmann (1936) discovered the existence of an inner core. Much later Dziewonski and Gilbert (1971) confirmed its expected solid state with observations of core-sensitive normal modes. In the last twenty years, large differences in travel times of body waves (e.g. Morelli et al., 1986; Creager, 1992) and anomalous splitting of normal modes (e.g. Woodhouse et al., 1986; Tromp, 1993; Durek and Romanowicz, 1999; Beghein and Trampert, 2003) indicate that the inner core is seismically anisotropic. Simple models with cylindrical anisotropy (Tromp, 1993) and axisymmetrical structure (Durek and Romanowicz, 1999) have been proposed. The latter might be explained by low order convection (Romanowicz et al., 1996; Buffett, 2009). However, other measurements suggest that the inner core structure is more complex than initially expected. For example, anisotropy is stronger in the western hemisphere than in the eastern hemisphere (e.g. Tanaka and Hamaguchi, 1997; Irving et al., 2009; Deuss et al., 2010) and the top couple hundred kilometers appear to be isotropic (e.g. Shearer, 1994; Song and Helmberger, 1995; Irving and Deuss, 2011). Most recently the shallow layering and lateral variations have been shown to be characteristically different between the two hemispheres (Waszek and Deuss, 2011). There is also the possibility of a distinct anisotropic region in the innermost inner core (e.g. Niu and Wen, 2001; Ishii and Dziewonski, 2002; Calvet et al., 2006; Cao and Romanowicz, 2007). Observations of velocity dispersion along polar paths suggest that attenuation also exhibits an anisotropic behavior (Souriau, 2009). Tkalčić (2010) suggest small scale variations in anisotropy.

A number of hypotheses have been proposed to explain the presence of inner core anisotropy. Suggestions include the formation of texture during solidification due to dendritic growth (Bergman, 1997), Maxwell stresses from the magnetic field (Karato, 1999; Buffett and Wenk, 2001), or by later plastic deformation due to anisotropic growth of the core (Yoshida et al., 1996; Deguen and Cardin, 2009; Deguen et al., 2011). Alboussière et al. (2010) and Monnereau et al. (2010) propose a lopsided growth, in which translation of the inner core produces melting in the eastern hemisphere and crystallization in the western. This translational motion causes no deformation within the inner core, but permits a hemispherical variations in increasing grain size and loss of texture due to annealing from the western hemisphere to the eastern hemisphere (Bergman et al., 2010).

Jeanloz and Wenk (1988) first suggested the possibility of a convecting inner core caused by radiogenic heating, which is not required in our model. Earlier numerical models for the inner core convection due to radiogenic heating (Weber and Machetel (1992)) are qualitatively similar to the results presented here, but require implausible levels of radiogenic heating. Yukutake (1998) argued that convection is unlikely in its current thermal state,

whereas Buffett (2009) suggested that convection is possible during the early stages, based on a model for the thermal evolution of the growing inner core. Most recently Deguen and Cardin (2011) have explored several cases of thermal and thermochemical convection in a numerical model, including the behavior during cessation of convection.

Here we use numerical simulations of thermochemical convection in the inner core to develop a parameterized convection model. The parameterized model to assess the entire evolution of the inner core, beginning with the initiation of crystallization at the center of the Earth. We also survey a broad range of physical parameters, with and without the inclusion of compositional buoyancy due to fractionation of light elements on solidification. The numerical simulations are based on CitcomS (Zhong et al., 2000; Tan et al., 2006), with appropriate modifications for the geometry and gravity field of the inner core. The numerical results are used to scale the convective cooling and parameterizing the influence of compositional buoyancy. Convective flow is dominated by small-scale downwelling when the Rayleigh number is well above the critical value for convection. We use the predicted flow to evaluate strain-rates and stresses, and to draw inferences about the origin of seismic anisotropy in the inner core.

6.2 Methods

6.2.1 Temperature at the inner-core boundary

We begin with a discussion of the parameterized model and subsequently use the results of the numerical simulations to tune the parameters of that model. Vigorous convection in the outer core maintains a mean state in the liquid that is isentropic and well mixed. Departures from a well-mixed mean state have been suggested at the top (Garnero et al., 1993) and at the bottom (Cormier, 2009) of the outer core, though we do not consider these complications here. As the outer core cools, solidification initiates at the center when the core temperature first intersects the pressure-dependent liquidus temperature. Continued cooling of the outer core causes the inner core to grow as the intersection of the core temperature and liquidus temperature moves outward. Consequently, the temperature at the surface of the inner core is set by the liquidus temperature, $T_L(c)$ at the current radius, c, of the inner core.

Buffett et al. (1996) present a simplified model for the growth of the inner core, which is driven by a prescribed surface-integrated heat flow, Q, at the core-mantle boundary (CMB). The model is based on a heat budget for the core, in which the leading order terms include secular cooling, latent heat released by solidification and heat produced by compositional arrangement in the gravity field. The temperature change in the heat budget is related to a change in the inner-core radius using estimates of the radial gradient in the liquidus

temperature. The resulting model for inner-core radius can be written as

$$M[\widetilde{c}(t)^2 + (H_L + H_G)\widetilde{c}(t)^3] = \int_0^t Q dt \tag{6.1}$$

where $M = 9.8 \times 10^{29}$ J is the heat loss required to cool the entire core to the solidification temperature and $\tilde{c}(t) = c/b$ is a dimensionless inner-core radius, which is scaled by the outer core radius $b = 3.48 \times 10^6$ m. Dimensionless parameters $H_L(= 2.2)$ and $H_G(= 0.88)$ characterize the influence of latent heat and compositional rearrangement, respectively. (The ratio of latent heat or compositional rearrangement to secular cooling varies is specified by $3H_{L,G}\,\tilde{c}(t)/2$.) Differentiating (6.1) gives the growth rate of the inner core growth:

$$M[2\widetilde{c}(t) + 3(H_L + H_G)\widetilde{c}(t)^2]\frac{d\widetilde{c}(t)}{dt} = Q \tag{6.2}$$

Strictly speaking, Q represents the CMB heat flow minus any radioactive heating in the outer core. Estimates for Q are uncertain, but typical values are on the order of 10^{12} W. Time variations in Q are also permitted in the model, but the uncertainties are too large to justify the introduction of more parameters (Buffett, 2002; Labrosse and Macouin, 2003).

The temperature at the radius of the inner-core boundary is determined by the liquidus temperature at the corresponding pressure. It is convenient to represent the pressure at $r = c(t)$ in terms of a pressure decrease relative to the value at the center $r = 0$. In this case, the liquidus temperature at the inner core boundary can be approximated by Lindeman's law (Stacey and Davis (2008))

$$T_L\,(c) = T_L(0)\exp\left[\frac{2(\gamma - \frac{1}{3})}{K_T}\Delta P\,(c)\right] \tag{6.3}$$

in which $T_L(0)$ is the liquidus temperature at the center of the Earth, γ is the Gruneisen parameter and K_T is the isothermal bulk modulus. When the inner-core density, ρ, is constant, the pressure decrease is $\Delta P(c) = -\frac{2}{3}\pi G\rho^2 b^2 c^2$, where G is the gravitational constant. (See Table 6.1 for all parameters.)

6.2.2 Internal temperature T_i

Convection in the inner core cannot occur until the internal temperature gradient exceeds the isentropic gradient, which is equivalent to an adiabatic gradient with the usual assumption of reversible processes. Figure 6.1a illustrates several representative examples of internal temperature when the inner core cools by conduction alone. The temperature profiles (indicated by the dashed lines) must match the liquidus temperature at the current inner-core radius ($c = 1220$ km). In one example the conductive temperature profile exceeds the local adiabat in the inner core (solid line), whereas the other case is less than the adiabat. When convection occurs with a superadiabatic temperature gradient, the internal temperature evolves toward an adiabatic profile with a thermal boundary layer at the top of the inner core (Figure 6.1b). We can specify the internal temperature $T_i(r)$ by the value at

$r = 0$. Extrapolating this value along the adiabat to $r = c$ yields a temperature, $T_i(c)$, which exceeds the boundary value by $\Delta T(c) = T_i(c) - T_L(c)$. This temperature difference gives the temperature drop across the thermal boundary layer. Alternatively we can represent the internal temperature by a potential temperature $\theta(r) = T_i(r) - T_a(r)$, where $T_a(r)$ is an adiabatic profile, which is anchored to the temperature at the inner-core boundary (e.g. $T_a(c) = T_L(c)$). When ΔT is small, the gradients in $T_i(r)$ and $T_a(r)$ are nearly identical. In this case, the internal temperature within the convecting part of the inner core is well approximated by $\theta(r) = \Delta T$ (see Figure 6.1b).

A positive value for ΔT indicates that the internal temperature is superadiabatic, whereas a negative value indicates a subadiabatic temperature profile. Convection occurs when ΔT exceeds a threshold for the onset of thermal instabilities. We define a Rayleigh number by

$$Ra \equiv \frac{\alpha_T g(c) \Delta T(c) c^3}{\nu \kappa} \tag{6.4}$$

where α_T is the coefficient of thermal expansion, $g(c)$, the gravitational acceleration at $r = c$, ν the kinematic viscosity, and κ is the thermal diffusivity. The critical threshold for a spherical geometry with linear variations in $g(r)$ is $Ra_c = 3091$ (Chandrasekhar, 1981). Initially the value of Ra is small because both c and $g(c)$ are small. However, convection becomes more likely as c (and $g(c)$) increase, so long as the rate of inner-core growth is fast enough to produce sufficiently positive values for $\Delta T(c)$. When $\Delta T(c)$ is too low to drive inner core convection, shallow flow might still occur due to lateral variations in heat flux at the inner-core boundary (Yoshida et al., 1996; Deguen and Cardin, 2009; Deguen et al., 2011).

Changes in the internal temperature of the inner core are governed by energy conservation. Heat is lost by a combination of convection and conduction down the adiabatic gradient. We lump these terms together into a single radial heat flux q_r. In addition, new material is continually added to the inner core at the local liquidus temperature $T_L(c)$. The new material is relatively cold and is eventually mixed by convection into the interior. Conservation of heat requires

$$\frac{d}{dt} \int_{V(t)} \rho C_P T_i \, dV = \int_{S(t)} q_r \, dS + \int_{S(t)} \rho C_P T_L \frac{dc}{dt} \, dS \tag{6.5}$$

where the specific heat, Cp, is assumed to be constant. By expressing the left-hand side of (4) in terms of the interior temperature, T_i, we assume that the boundary layer cools at the same rate as the interior. We show below that the temperature drop across the boundary layer is small and relatively constant in time, which means that the boundary region cools together with the interior. Explicitly accounting for the time-dependent volume of the inner core gives

$$\frac{d}{dt} \int_{V(t)} \rho C_P T_i \, dV = \int_{V(t))} \rho C_P \frac{dT_i}{dt} \, dV + \int_{S(t)} \rho C_P T_i(c) \frac{dc}{dt} \, dS \tag{6.6}$$

Combining (6.5) and (6.6) gives an equation for the evolution of T_i

$$\int_{V(t)} \rho C_P \frac{dT_i}{dt} dV = \int_{S(t)} q_r \, dS - \int_{S(t)} \rho C_P \Delta T(c) \frac{dc}{dt} dS \tag{6.7}$$

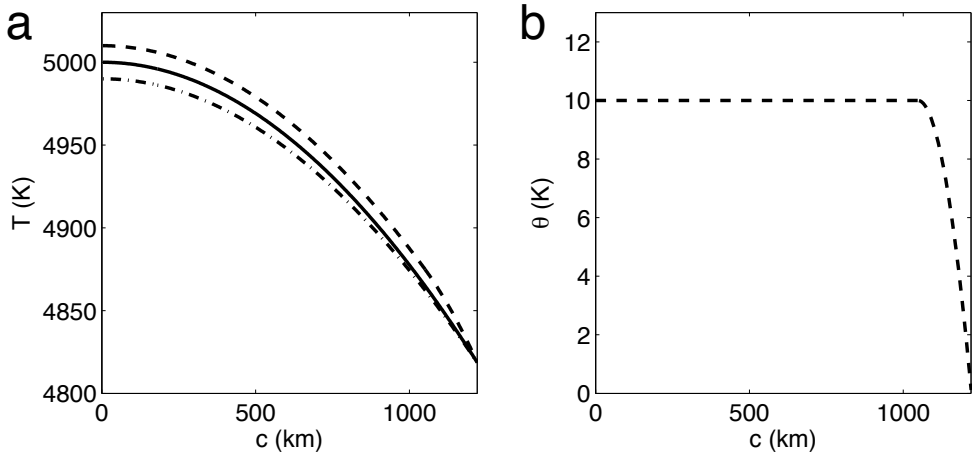

Figure 6.1: **a.** A representative adiabatic profile (solid line) is depicted for the present-size inner core (c=1220 km). Two conductive temperature profiles are shown for comparison; one is superadiatic (dashed line) and the other subadiabatic (dot-dashed line). **b.** The potential temperature $\theta(r) = T_i(r) - T_a(r)$ is assumed to be uniform in the convecting interior of the inner core and equal to the value of the temperature drop across the thermal boundary layer.

where $\Delta T(c) = T_i(c) - T_L(c)$ corresponds to the temperature difference between the well-mixed interior and the boundary. When the change in temperature across the inner core is small compared with T_i (i.e. $(T_i(0) - T_i(c))/T_i(0) << 1$), we can assume that dT_i/dt is independent of position and write

$$M_i C_p \frac{dT_i}{dt} = \int_{S(t)} q_r \, dS - \int_{S(t)} \rho C_P \Delta T(c) \frac{dc}{dt} dS \tag{6.8}$$

where $M_i = 4\pi\rho c^3/3$ is the mass of the inner core. The growth-rate, dc/dt, is specified by the imposed CMB heat flow, according to (6.2), so a solution for T_i requires an estimate for the radial heat flow q_r.

When the inner core is convecting (i.e. $\Delta T(c)$ sufficiently large to exceed the critical Ra), the radial heat flux is given by

$$q_r = -k \frac{\partial T_a(c)}{\partial r} + q_{conv} \tag{6.9}$$

where k is the thermal conductivity of iron and the adiabatic gradient at $r = c$ is

$$\frac{\partial T_a\,(c)}{\partial r} = \left(\frac{\gamma T_L(c)}{K_S} \right) \frac{\partial P}{\partial r} \tag{6.10}$$

The convective heat flux, q_{conv}, is parameterized in terms of $\Delta T(c)$, using conventional boundary layer theory (Turcotte and Schubert, 2002). Assuming that thermal boundary

layer grows by conduction to the point of thermal instability, the time-averaged heat flux is given by

$$q_{conv} = \gamma k \left(\frac{\alpha_T g(c)}{Ra_{bl} \nu \kappa} \right)^{1/3} \Delta T(c)^{4/3} \tag{6.11}$$

where Ra_{bl} refers to the critical value for instabilities in the boundary layer. In the regime where boundary-layer theory is appropriate, we expect the boundary layer to be thin and the effect of boundary curvature to be small. Averaging the heat flux over the time required for the boundary layer to become unstable in a plane layer sets the value of $\gamma = 2.61$(Turcotte and Schubert, 2002, page 274) for use in (11). The corresponding temperature drop across the thermal boundary layer in an internally heated sphere is:

$$\theta = \frac{\Delta T}{\Delta T_c} = \left(\frac{2}{\gamma} \right)^{3/4} \left(\frac{Ra}{Ra_{bl}} \right)^{-1/4} = 0.82 \left(\frac{Ra}{Ra_{bl}} \right)^{-1/4} \tag{6.12}$$

where ΔT_c is the superadiabatic temperature drop across the inner core in the absence of convection. Note that ΔT_c will also be used to normalize the temperature in the numerical case.

In section 6.4.2 we use a numerical convection model (CitcomS) to assess the relationship in (12). We find good agreement with parameterization of q_{conv} in terms of $\Delta T^{4/3}$. However, the best-fitting value of γ for a sphere with radially varying gravity is $\gamma = 4.9$. (see 6.4.2). The adjusted value of γ is subsequently used in all parameterized models. When the inner core is not convecting, we use the solution for conductive cooling from Buffett (2009) to evaluate q_r.

A typical solution for $T_i(r)$ is initialized with $T_i(c) = T_L(c)$ at time the inner core begins to solidify. The liquidus temperature evolves with inner-core growth, based on (6.2) and (6.3), while $T_i(c)$ is governed by (6.8). Time steps of 10^5 years are used in the numerical integration for $T_i(c)$. At each time step new values for $T_i(c)$ and $T_L(c)$ are used to update the temperature drop $\Delta T(c) = T_i(c) - T_L(c)$ and convective heat flux q_r. Results are presented in the section 3, after introducing the effects of chemical stratification.

6.2.3 Compositional stratification

The density gradient at the top of the inner core is sensitive to small changes in composition. When solidification excludes impurities in the liquid, we expect the concentration of impurities to increase in the residual liquid. Indeed, the exclusion of one or more light elements is thought to be an important source of buoyancy for driving flow in the liquid outer core. As the concentration of light elements increases in the liquid we can reasonably expect changes in the composition of the solid. It is customary to express the concentration of light elements in the solid (denoted by C_s) as a fraction, χ, of the light-element concentration C in the liquid (e.g. $C_s = \chi C$). In this case an increase in C with time creates a stable stratification as the inner core grows. Theoretical calculations for commonly proposed light elements (Alfè et al. (2002)) suggest that the partitioning of O into the solid is

small ($\chi < 0.02$), whereas S and Si readily partition into the solid ($\chi > 0.8$). We consider a large range of values for χ to investigate the potential role of composition on convection.

By definition, the mass of light element in the outer core is $\rho C V_l$, where V_l is the volume of liquid. When the inner core grows by dc the volume of the liquid changes by dV_l ($= -4\pi c^2 dc$) and a mass of light element, $\rho\chi C dV_l$, is transferred from the liquid into the solid. Conservation of light element requires

$$\rho\chi C dV_l = d(\rho C V_l) = \rho(dC)V_l + \rho V_l dC \tag{6.13}$$

Substituting for V_l and dV_l yields

$$\frac{\mathrm{d}C}{\mathrm{d}c} = 3C(1-\chi)\frac{c^2}{(b^3 - c^3)} \tag{6.14}$$

which describes how the concentration of light elements in the liquid core changes as the inner core grows. Assuming that the concentration of light element incorporated into the solid is $C_s = \chi C$, where χ is assumed constant, the change in the composition of the inner core is $dC_s/dc = \chi dC/dc$. A competition between the thermal and compositional buoyancy can dramatically shorten the duration of thermal convection in the inner core.

In order to quantify the influence of composition we assess the conditions required for thermal convection to homogenize the composition of the inner core. We begin by integrating (6.14) for the composition of the liquid as a function of inner core radius

$$C(c) = C(0)\left[\frac{b^3}{b^3 - c^3}\right]^{1-\chi} \tag{6.15}$$

where $C(0)$ is the initial composition of the fluid prior to the formation of the inner core. The composition of the inner core in the absence of mixing is

$$C_s(c) = C(0)\chi\left[\frac{b^3}{b^3 - c^3}\right]^{1-\chi} \approx C(0)\chi\left[1 + (1-\chi)\frac{c^3}{b^3}\right] \tag{6.16}$$

where the approximation represents a first-order Taylor series expansion in $(c/b)^3$. By comparison, the composition in a convectively mixed inner core is

$$\bar{C}_s(c) = \frac{1}{V_s}\int_{V_s} C_s(c)\, dV_s = C(0)\chi\left[1 + \frac{1}{2}(1-\chi)\frac{c^3}{b^3}\right] \tag{6.17}$$

where V_s is the volume of the inner core. As new material is added to the inner core by solidification, the compositional difference between the boundary and a well mixed interior is

$$\Delta C_s = C_s(c) - \bar{C}_s(c) = \frac{1}{2}\left(\frac{c}{b}\right)^3 C(0)\chi(1-\chi) \tag{6.18}$$

Therefore, we expect the influence of compositional buoyancy to be weak when the inner core is sufficiently small. However an increase in ΔC_s as the inner core grows can make

convective entrainment of the light element more difficult as time progresses. The magnitude of the compositional buoyancy depends on the coefficient of compositional expansion, α_C (see Table 1 for parameter values).

Sleep (1988) developed a simple model for the entrainment of a dense chemical layer at the base of the mantle. The same model can be applied here to quantify the convective entrainment of light elements by cold thermal downwellings. For cylindrical downwellings the maximum volume fraction of entrained material in the plume (denoted by E) is

$$E = \frac{1}{2}\frac{\alpha_T \Delta T}{\alpha_C \Delta C_s} \tag{6.19}$$

where ΔT is the temperature deficit in the plume and ΔC_s is the intrinsic density difference between the material in the boundary region and the interior. We use the temperature drop across the thermal boundary layer to quantify the temperature deficit in the plume and evaluate ΔC_s using (6.18).

The total convective heat flux can be related to the total volume flux, F, of material in the plumes by

$$\int_S q_{conv}\, dS = \rho C_p \Delta T F \tag{6.20}$$

Similarly, the total convective flux of light element into the interior is

$$\int_S I_{conv}\, dS = \rho \Delta C_s E F \tag{6.21}$$

Expressing the entrainment of light elements in terms of the heat flux gives

$$\int_S I_{conv}\, dS = \frac{1}{2C_p}\frac{\alpha_T}{\alpha_C}\int_S q_{conv}\, dS \tag{6.22}$$

By comparison, the supply of light element due to inner-core growth is given by

$$\int_S I_{input}\, dS = 4\pi\rho C_s(c) c^2 \frac{\mathrm{d}c}{\mathrm{d}t} \tag{6.23}$$

When the convective entrainment of light element exceeds the supply of light element due to inner core growth, we assume that the excess light element is effectively mixed into the interior. However, once the supply of light element outpaces the convective entrainment, a layer of excess light elements grows downward into the convectively mixing interior. Deguen and Cardin (2011) find a transitional regime where thermal convection continues below a chemically stratified layer. Here we use the onset of growth of a chemically stratified layer to indicate the maximum radial extent of thermal convection.

6.3 Results

6.3.1 A representative case

To illustrate the results of the model we choose a CMB heat flux of 7 TW, corresponding to an inner core age of 1.1 Gy for the simple growth model in (1). A representative value for the thermal conductivity is 36 $\mathrm{Wm^{-1}K^{-1}}$ (Stacey and Davis, 2008), but a wide range of values for both k and Q are considered in the next section [1]. Other parameter values are given in Table 6.1. Figure 6.2 shows results for the representative case as a function of time. At the present time (i.e. inner-core age $t = 1.1$ Gy) convection occurs with a boundary-layer temperature jump of $\Delta T \sim 0.9\ K$ (Fig. 6.2b) and a Rayleigh number of $\sim 4.3 \times 10^6$ (Fig. 6.2c). Convection terminates once the age of the inner core reaches $t = 1.7$ Gy. For this particular case convection extends beyond the present day.

If convection did not occur (say due to a strong compositional stratification), the temperature in the interior would be higher. Figure 6.2b shows the superadiabatic temperature difference between the top and bottom of the inner core when convection is not permitted (dashed line). The superadiabatic temperature difference for this purely conductive case decreases at later stages as the inner core growth slows down. Allowing for convection enhances the cooling of the inner core and shortens the time the inner core spends in a superadiabatic state. The Rayleigh number (6.2c), and thus the vigor of convection, increases initially with time due to its dependence on c and $g(c)$. In fact, the peak value of Ra occurs after the peak in the superadiabatic temperature for the convecting case (solid line in Fig. 6.2b).

Figure 6.2d compares the convective entrainment of light elements with the supply of light elements due to inner-core growth. For this example, we assume a light element composition of $C(0) = 0.06$ in the outer core and a partitioning ratio of $\chi = 0.2$ during solidification. For these particular parameters the entrainment of light element exceeds the supply only during the initial stages. A transition occurs around 0.4 Gy when a layer of light element layer begins to thicken. The inner-core radius at the time of transition is roughly 750 km.

Figure 6.3 summarizes the maximum radial extent of convection for different choices of $C(0)$ and χ. Results for values of χ above 0.5 are inferred by reflecting the results below $\chi = 0.5$ because of the factor $\chi(1-\chi)$ in the definition of the compositional stratification in the inner core (see equation 16). For low χ very little light element is incorporated into the inner core, so the resulting compositional stratification is weak. On the other hand, values of χ close to one cause very little fractionation of light element, so the composition of the liquid does not evolve with time. In either case, the stabilizing influence of composition is weak when $\chi(1-\chi)$ is small. Multiple light elements in the liquid can fractionate differently and this may have an important influence on the stratification. For example, theoretical

[1] Recent results show that conductivity values could be two or three times higher than our representative value here. The consequences of this are discussed in the afterword in Section 6.7

Parameter	Value	Unit	Comment/reference
k thermal conductivity	36	$Wm^{-1}K^{-1}$	Varied in 6.3.2 Stacey and Davis (2008)
Q heat flux at CMB	7×10^{12}	W	Varied in 6.3.2 Lay et al. (2008)
γ Gruneisen parameter	1.4	-	Vočadlo et al. (2003)
K_T isothermal bulk modulus	1.2×10^{12}	Pa	Vočadlo et al. (2003)
K_S adiabatic bulk modulus	1.3×10^{12}	Pa	Vočadlo et al. (2003)
ρ density	1.3×10^{4}	kgm^{-3}	Vočadlo et al. (2003)
η dynamic viscosity	10^{18}	Pas	Dumberry and Bloxham (2002)
ν kinematic viscosity	7.7×10^{13}	m^2s^{-1}	η/ρ
C_P specific heat	8×10^{2}	$JKg^{-1}K^{-1}$	Stacey and Davis (2008)
α_T thermal expansion	10^{-5}	K^{-1}	Vočadlo et al. (2003)
$T_L(0)$ Melting temp. at center	5000	K	Vočadlo and Alfè (2002)
κ thermal diffusivity	3.5×10^{-6}	m^2s^{-1}	$k/(\rho C_P)$
α_C compositional effect on density	0.6	-	Braginsky and Roberts (1995)
C conc. of light elem. in OC	0.06	-	Alfè et al. (2007)
χ frac. of light elem. incorporated	0.2	-	Alfè et al. (2007)

Table 6.1: Parameter values used in the model.

calculations suggest that the value of χ for O is close to zero and close to one for both S and Si ((Alfè et al., 2002)), implying a weak compositional stratification. However, there are also plausible values of $C(0)$ and χ where compositional stratification is sufficient to suppress thermal convection at all times (black squares in Fig. 3).

6.3.2 Sensitivity to Parameter Values

Many of the parameters used in this study are poorly known; the two most important parameters are the CMB heat flux and the thermal conductivity. Here we present results for a CMB heat flux betweeen 4 to 14 TW and for a conductivity between 20 to 70 $\mathrm{WK^{-1}m^{-1}}$. Figure 6.4 shows the maximum radial extent of convection with and without the influence of compositional stratification. The results can be organized into three regions; one where no convection occurs (*squares*), one where convection has ceased for present day (*circles*) and one where convection is still ongoing (*triangles*). For the nominal conductivity value of 36 $\mathrm{WK^{-1}m^{-1}}$ the critical heat flux value for convection to occur is 4.1 TW, which corresponds to a maximum age of 1.93 Gy. When the inner core is younger than 1.26 Gy, or CMB heat fluxes higher than 6.3 TW, convection would occur today in the absence of chemical stratification. Figure 6.4b shows the radius at which convection terminates when compositional stratification is included, using $C = 0.06$ and $\chi = 0.2$. For the nominal thermal conductivity, the minimum heat flux needed to initiate convection increases to 5.5 TW (with a corresponding inner core age of $\sim$1.4 Gy). To sustain convection until the present time requires a Q of 9.4 TW ($\sim$ 0.8 Gy).

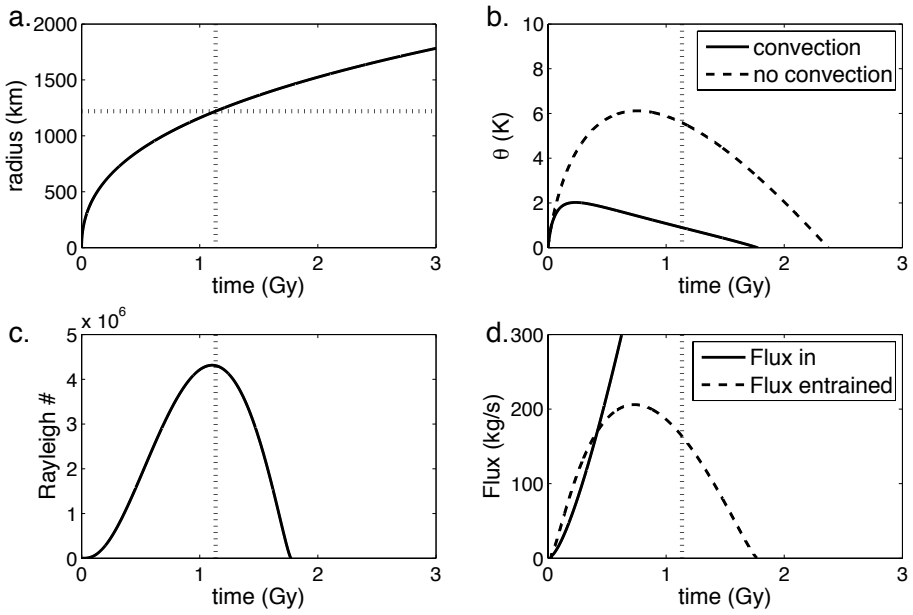

Figure 6.2: Inner core thermal history for a 7 TW CMB heat flux and a conductivity of 36 $\mathrm{Wm^{-1}K^{-1}}$ (other values are given in table 6.1). **a.** Radius of inner core as a function of time. Present-day inner core radius and time are shown by the dotted lines. **b.** Super-adiabatic temperature change as a function of time, for a case in which convection occurs (solid line) and a case with no convection allowed (dashed line). **c.** Rayleigh number as a function of time. The Rayleigh number peaks later than the temperature jump, due to its dependence on the inner core size. **d.** Flux of light elements into the inner core due to solidification compared with the rate of convective entrainment.

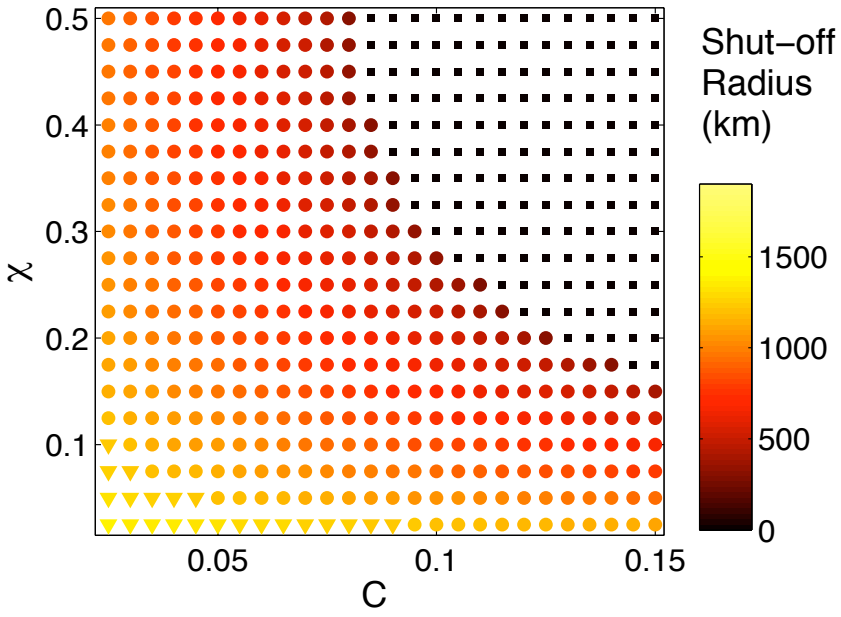

Figure 6.3: Role of compositional gradient on the termination of convection in the representative case ($Q = 7$ TW and $k = 36$ $\mathrm{Wm^{-1}K^{-1}}$). A range of values for light element concentration in the outer core and the incorporation of light element into the solid during solidification. Squares indicate cases where chemical stratification suppresses all convection. Circles denote the occurrence but termination of convection before the present day, whereas triangles indicate ongoing convection.

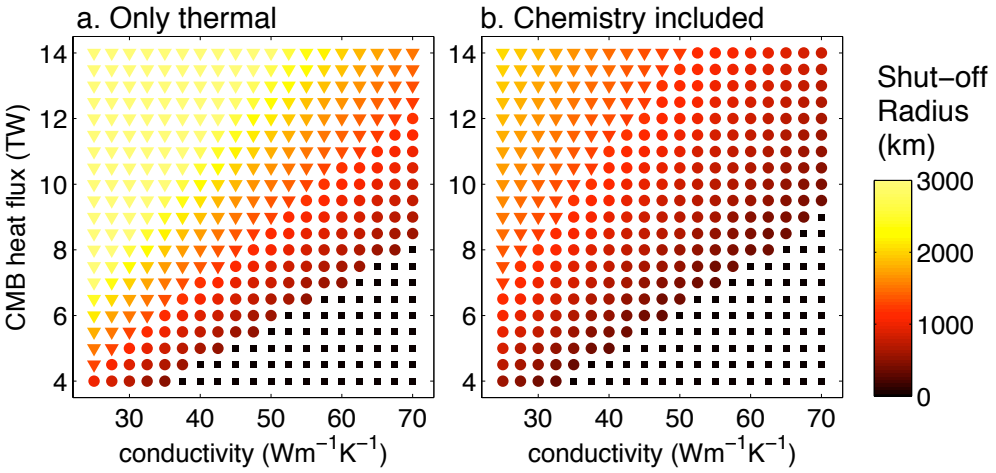

Figure 6.4: Radius of termination for a range of CMB heat fluxes and conductivities. a. is without influx of light element at the top of the inner core, while b. assumes a 6% light element concentration in the outer core and 20% incorporation into the solid inner core. Compositional 'shut-down' is assumed when light element influx exceeds the convective entrainment (example in figure 6.2d).

6.4 Numerical results

6.4.1 Setup of CitcomS

Numerical simulations based on CitcomS (Zhong et al., 2000; Tan et al., 2006) are used to scale the convective heat flux in the purely thermal case and to characterize the entrainment and mixing of light element from the top of the inner core in the thermochemical case. CitcomS is a finite element model for thermal convection in a spherical shell. This software was originally written to deal with mantle convection, so a few adaptations are needed for application to the inner core. Obviously the main complication is that the inner core is a sphere and not a spherical shell, creating a singularity at the center of the mesh. To avoid changing the mesh, we decreased the radius of the inner sphere to 0.1% of the ICB value without causing instabilities at the center elements. Additionally the gravitational acceleration was altered to vary linearly with radius. The adapted code reproduces the critical onset of convection as derived for a sphere by Chandrasekhar (1981).

Convection in the inner core is driven by cooling the surface faster than the interior. In the parameterized model we use a simple thermal history of the core to prescribe the temperature and radius of the inner core as a function of time. To assess the parameterized model using CitcomS, we solve directly for the superadiabatic temperature perturbation $\theta = T_i - T_a$, where T_i is the total temperature in the inner core and T_a the adiabatic temperature profile that matches the value at the boundary (e.g. $T_a(c) = T_L(c)$). In this

case the cooling of the inner core can be represented as a heat source in the equation for θ. We begin with the energy equation for T_i, which can be written as

$$\frac{\partial T_i}{\partial t} + v \cdot \nabla T_i = \kappa \nabla^2 T_i + H_r / C_p \tag{6.24}$$

where H_r would include any radioactive heating, although we assume this to be zero. An equation for θ is obtained by substituting $T_i = T_a + \theta$ into (15), yielding

$$\frac{\partial \theta}{\partial t} + v \cdot \nabla \theta = \kappa \nabla^2 \theta - \frac{\partial T_a}{\partial t} + \kappa \nabla^2 (T_a) - v \cdot \nabla T_a \tag{6.25}$$

The last term vanishes because motion through an adiabatic gradient produces no change in the potential temperature θ. The next two terms from the right are combined into a single heat source for θ, which we denote by H_θ / C_p. When the radial change in T_a is small compared with T_a (as in the case of the inner core), both $\partial T_a / \partial t$ and $\kappa \nabla^2 T_a$ are nearly constant in space. Over time scales that are short compared with the growth of the inner core we can also treat $\partial T_a / \partial t$ as constant in time.

Next, we express the energy equation in nondimensional form using $c(t)$ as a length scale, which maps the growing inner core onto the unit sphere. The dimensionless position vector in the inner core is $\bar{r}' = \bar{r}/c(t)$. We also use $c(t)^2/\kappa$ as the time scale, and scale the temperature using the superadiabatic temperature change across the inner core, based on the steady, conductive solution of the heat equation with the imposed heat source H_θ. We denote the conductive solution by θ_c and define the temperature scale by

$$\Delta \theta_c = \theta_c(0) - \theta_c(c) = \frac{1}{6} \frac{H_\theta}{C_p} \left(\frac{c(t)^2}{\kappa} \right) \tag{6.26}$$

Numerical solutions for θ are obtained at specific epochs from the thermal history, resulting in fixed length, time and temperature scale. However, the time dependent length scale introduces in one additional term in the dimensionless temperature equation for $\theta'(\bar{r}', t')$ because both the position vector $\bar{r}' = \bar{r}/c(t')$ and t' change with time. The dimensionless heat equation becomes

$$\frac{\partial \theta'}{\partial t'} + \frac{1}{c} \frac{dc}{dt'} \bar{r} \cdot \nabla' \theta' + v' \cdot \nabla' \theta' = \nabla'^2 \theta' + H'_\theta \tag{6.27}$$

where the additional term involving dc/dt can be viewed as an advective heat flux (analogous to $v' \cdot \nabla' \theta'$). For most of the history of the inner core, this additional term is negibibly small because $dc/dt << v'$ (as shown below).

We can also interpret the additional term in (27) as a heat sink by establishing a connection with the global heat budget in (8). Integrating the additional term over the volume of the inner core (noting that the largest gradient in θ' is confined to the thermal boundary layer) gives

$$\int_V \frac{1}{c} \frac{dc}{dt} \bar{r} \cdot \nabla' \theta' dV \approx \int_S \Delta \theta' \frac{dc}{dt} dS \tag{6.28}$$

where $\Delta\theta'$ is the dimensionless temperature jump across the boundary layer. The surface integral in (28) can be viewed as a cooling term associated with the addition of new, cold material as the inner core grows; it is identical to the cooling term in the global heat budget in (8). To include this term as a heat sink in CitcomS, we would include a (negative) heat source in the outer boundary region of the inner core. Unfortunately, the standard version of CitcomS does not permit a spatially varying heat source, so instead we distribute the volume-integrated cooling uniformly across the inner core to enforce global heat conservation. The resulting error is small because the heat source due to inner-core growth is negligible over most of the history of the inner core. Nevertheless we include it in our numerical calculations. Consequently, H_θ contains one main source term due to the decreasing adiabatic temperature and two smaller terms due to conductive cooling along the adiabat and addition of new inner-core material. We evaluate H_θ at a particular epoch (or inner core radius) and run CitcomS to a statistical steady state. This approximation is reasonable because the time scale for change in H_θ is long compared with the time scale for convective overturn (see below). The Rayleigh number in CitcomS is defined by

$$Ra(c) \equiv \frac{\alpha_T g(c) \Delta\theta_c(c) c^3}{\nu\kappa} \tag{6.29}$$

where $\Delta\theta_c$ is evaluated using the heat source H_θ at a particular epoch.

6.4.2 Scaling the parameterized model

We estimate the temperature drop across the boundary layer from a series of simulations over a range of Rayleigh numbers and compare the results with the predictions of the parameterized model. Averaging the potential temperature over the interior (excluding the boundary layer region) gives a well-defined estimate of the temperature drop, $\bar{\theta}$. Results are plotted in Figure 6.5. The relationship between $\bar{\theta}$ and Ra is best fit by

$$\bar{\theta} = 0.51(Ra/Ra_{bl})^{-0.25} \tag{6.30}$$

, where $Ra_{bl} = 1000$ is the critical Rayleigh number in a boundary layer. The power $-1/4$ dependence on the Rayleigh number is the same as that obtained for the boundary layer model in the case of an internally heated fluid Turcotte and Schubert (2002) (see equation (6.12)). This suggests that the form of equation (6.11) for the convective heat is reasonably good despite the modest values for Ra. The numerical results also suggest that cooling is more effective in a sphere with variable gravity. The best-fitting solution for $\bar{\theta}$, implies a constant $\gamma = 4.9$ (instead of $\gamma = 2.61$) in equation (6.11). The higher value was used consistently in the parameterized model. Alternatively, we could have adjusted Ra_{bl} using the value of γ defined by Turcotte and Schubert (2002), The value of Ra_{bl} would decrease to 150 to match the numerical results for a spherical geometry with radially varying gravity, but the results for the parameterized model would be unchanged.

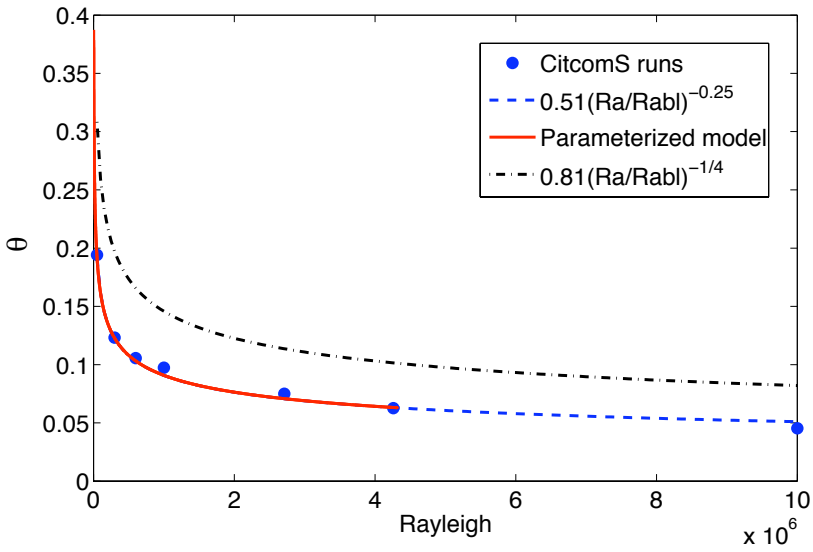

Figure 6.5: Ra-θ relationship for CitcomS (dots) and parameterized model (solid line). The best fit to the numerical results, $\bar{\theta} = 0.51(Ra/Ra_{bl})^{-0.25}$, (dashed line) is used to tune the parameterized model over the relevant range of Ra. The dot-dashed line represents equation (6.12) derived from Turcotte and Schubert (2002).

6.4.3 Results of the pure thermal case

Mean one-dimensional profiles of θ from the numerical solution are shown for two cases in Figure 6.6. A steep thermal boundary layer is evident above a relatively uniform internal temperature. The estimated temperature drops across the boundary, $\bar{\theta}$ are 1.1 K and 1.9 K for radii of 1220 and 973 km, respectively. The parameterized model is tuned to reproduce these values (see Figure 2a and b).

The spatial pattern of convection is shown in map view and cross-section in Figure 6.7. Roughly ten downwelling plumes are located at the inner core boundary at any given time. The lateral radius of an individual plume is on the order of 10^5 m. Peak velocities occur in the upper half of the inner core and the root-mean-square (rms) velocities over this region are on the order of cm/year. These results are in good agreement with the boundary layer model, which predicts that velocities scale as $Ra^{1/2}$, where κ/R is the velocity scale. The rms velocity and lateral length scale of the plumes implies a strain rate of 10^{-15} s^{-1} and stresses on the order of 10^3 Pa for a viscosity of 10^{18} Pa s . Weaker flow and slowers strain rates are predicted in the lower half of the inner core. Downwelling plumes eventually pond laterally where the gravitational force decrease towards zero. The lower velocities at the center may explain why the numerical method is stable with small elements near the innermost boundary.

The overturn time is on the order of 10^8 years, which is short compared with the

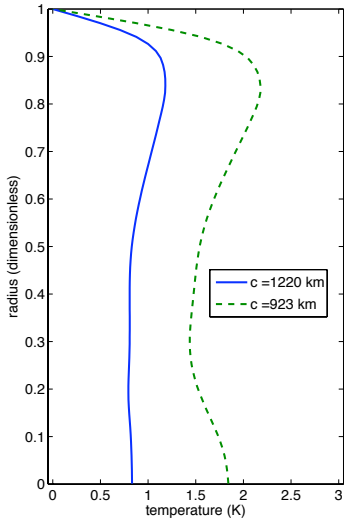

Figure 6.6: Mean 1D superadiabatic temperature profiles from CitcomS runs for an inner core of 1.1Gy at its current size (solid line) and at an age of 0.55 Gy, corresponding to a radius of 923 km (dashed line). The average temperature in the interior defines the temperature jump across the thermal boundary layer. The parameterized model is adjusted to approximate these results.

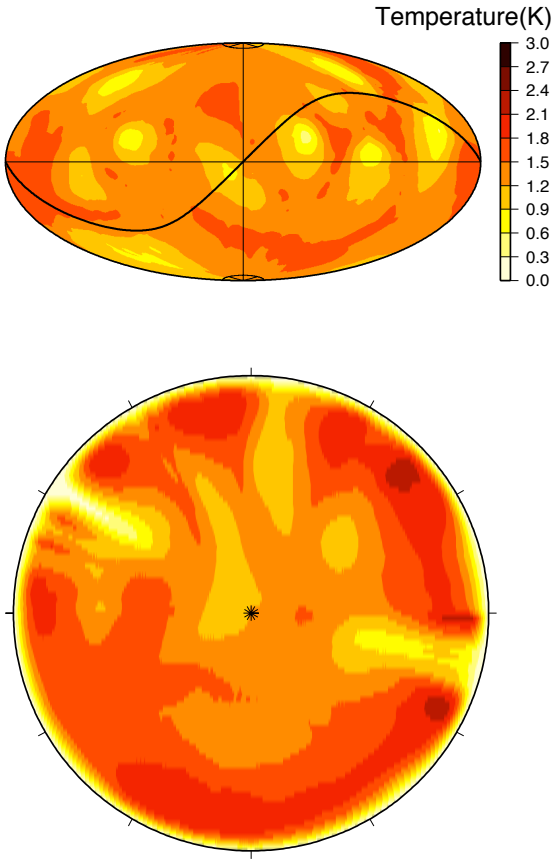

Figure 6.7: Spatial variations in superadiabatic temperature in map view at $r' = 0.5$ and in cross-section. Cross-sectional view is denoted on the map by the black line.

time for changes in the heat source H_θ. A characteristic time scale for the heat source is $H_\theta/(dH_\theta/dt)$, which is comparable to the age of the inner core ($\sim 10^9$ years) and is one order of magnitude higher than the overturn time. Many convective overturns are expected before cessation. This results supports the assumption that a quasi-steady convective tracks a slowly evolving heat source.

6.4.4 Results for the thermo-chemical case

Next we introduce compositional buoyancy to illustrate the mechanism of convective entrainment of light elements at the top of the inner core. The composition is tracked by tracer particles, applying the ratio method as implemented in CitcomS (Tackley and King, 2003). To ensure stability the inner sphere radius is increased to 10% for these cases. Additionally we decrease the thickness of shells at the top to increase resolution. Light element is added to a compositional distinct layer, which contrasts with the underlying well-mixed region according to equation (6.18) for $C = 0.06$ and $\chi = 0.02$. This initial condition in composition represents a layer of newly solidified material with a thickness of 46 km which has not yet been mixed into the interior. For the initial thermal state we adopt a final state from a purely thermal convection calculation. The initial maximum chemical density contrast across the boundary layer is 7.5 times higher than the maximum thermal density contrast. The volume fraction of entrainment is initially predicted to be around 0.067 (equation 6.19).

Figure 6.8 illustrates how the buoyant material accumulates and becomes entrained at downwelling plumes. This behavior is comparable to the response of a dense chemical layer at the bottom of the mantle, which becomes entrained in overlying convection (Sleep, 1988). As entrainment and mixing progresses the chemical density contrast between the interior and the light element layer decreases, the capacity of entrainment increases (see eq. (6.19), eventually removing the entire layer. In reality new light element is continually added to the top of the inner core by solidification, so the layer would not vanish (although it may become too thin to resolve in our calculations). The rms velocity has not significantly changed with the introduction of compositional effects. Any difference in the mean velocity between the thermochemical and the purely thermal case is small compared to temporal fluctuations. We use these numerical results to motivate the use of a simple convective entrainment parameterization, based on the carrying capacity of dense thermal plumes (section 6.2.3).

6.5 Discussion

The feasibility of convection in the inner core depends on two key physical properties in the core. The first is the thermal conductivity of the iron alloy in the inner core. Published values span a wide range (from 63 $\mathrm{Wm}^{-1}K^{-1}$ (Stacey and Anderson, 2001) to 28 $Wm^{-1}K^{-1}$ (Stacey and Loper, 2007). Here we adopt the recent estimate of 36 $\mathrm{Wm}^{-1}K^{-1}$

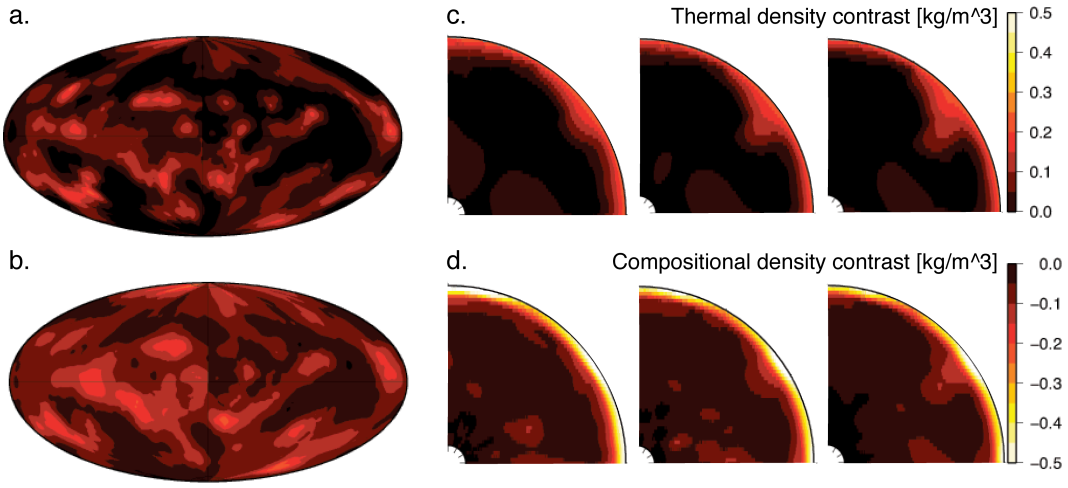

Figure 6.8: Thermal and compositional contributions to the density variations in thermo-chemical convection. Spatial variations in (a) thermal and (b) composition density are shown on a radial surface at $r' = 0.75$. The locations of cold (dense) downwellings coincide with regions of compositionally buoyant material (i.e. negative density contrast). Temporal variations in (c) thermal and (d) composition density is shown in a series of cross-section, separated by intervals of 9 Myr. A developing cold plume entrains light element from a compositionally distinct layer at the top (see text).

from Stacey and Davis (2008), but acknowledge that large uncertainties remain. Experiments up to 70 GPa and 2000K measure values of 32 $Wm^{-1}K^{-1}$ at the lower end of this range (Konôpková et al., 2011). On the other hand, recent theoretical calculations predict much higher thermal conductivities (Sha and Cohen, 2011), although the calculations did not reach the temperature conditions of the core. As shown in section 6.3.2, high values inhibit convection by promoting heat loss due to conduction along the adiabat. Even though the published range only spans a factor of two, our results show this can make a large difference in interpreting the inner core from a dynamical point of view. Further constraint on the thermal conductivity will be important for establishing the possibility of inner-core convection.

Heat flow at the CMB is a second key parameter. An intriguing recent estimate for the present day heat flux is based on seismic observations of phase stratification in the D" (Van der Hilst et al., 2007; Lay et al., 2008; Kawai and Tsuchiya, 2009). Here we adopt a constant CMB heat flux throughout the inner core history, but one could argue for higher (or lower) values in the past. Paleomagnetic measurements show that the Earth has sustained a dynamo for at least 3 Gy (e.g. Kono and Roberts, 2002) and provide estimations of the required CMB heat flux (Buffett, 2002; Labrosse and Macouin, 2003). A complex heat flow history is not justified for this study given the current uncertainties. However, our model illustrates that estimates of CMB heat flow at the early stages of the inner core are crucial in constraining the present day thermal state. High heat flow in early stages results in rapid initial growth which can establish a long-standing thermal instability (see Figures 6.2a and

6.2b). Present-day thermal convection could occur because of early high heat flows, even though present-day heat flow might be lower and not predict any thermal instability.

The liquidus temperature of iron at the center of the inner core is also uncertain, although the consequences for inner-core convection are less dramatic. We have adopted a modest temperature of 5000 K for the onset of solidification at the center of the Earth. Higher values have been proposed on the basis of theoretical calculations (Alfè, 2010). On the other hand, some experiments support lower values (Boehler et al., 2008). The liquidus temperature parameter controls the gradients in the adiabatic and liquidus temperature profiles, which establishes the relationship between core cooling and inner-core growth. With a higher liquidus temperature, the relative difference between these two gradients would increase, causing a decrease in the growth rate and making high demands on the CMB heat flux to sustain convection. Fortunately, the likely uncertainty in this value has only a modest effect on the occurrence of convection.

The viscosity is another important parameter that controls the onset and vigor of convection for a given superadiabatic temperature. We adopt a value of 10^{18} Pa s, which falls within estimates by Dumberry and Bloxham (2002). Both the strain-rate and the deformation mechanisms are directly dependent on the vigor of convection.

The question of inner core convection is partially motivated by the goal of explaining observations in seismic anisotropy. The strain rates associated with the (purely) thermal convection are around $10^{-15}s^{-1}$ for down-going plumes with lateral dimensions of 10^5 m. The time required to accumulate enough strain to produce a texture (typical strains on the order of unity) is several 10^7 years, which is slightly less than the overturn time. Similar strain rates have been proposed for flow confined to the top 100 km due to anisotropic growth of the inner core (Deguen et al., 2011) and for similar thermo-chemical convection (Deguen and Cardin, 2011). If the ongoing deformation is accommodated by dislocation glide, texturing of hcp iron could occur, causing seismic anisotropy through lattice preferred orientation (LPO). Although diffusion creep is more active at higher temperature, and does not cause texturing, the large grain sizes in the inner core can promote dislocation creep (van Orman, 2004). These strain rates also lie well within the range that predicts dislocation creep under inner core conditions (Reaman and Daehn, 2011). Although there remains uncertainty in the elastic properties of iron at inner core conditions, most recent ab initio calculations (Vočadlo et al., 2009; Sha and Cohen, 2010) and experimental results (Tateno et al., 2010) agree on a faster c-axis than a-axis in hcp iron. Iron stacked by fcc or mixed hcp/fcc, show even stronger c/a axes ratio (Ishikawa et al., 2011). Thus alignment of the c-axis along the rotation axis could explain the large scale seismic observation. The broad alignment of c-axes with the rotation axis could be explained by a degree-one mode of convection. In our representative case we see a much more complicated pattern of convection when the Rayleigh number is well above the critical value. In other cases, convection terminates during the growth of the inner core, leaving behind a fossil of the anisotropy that was produced by a lower degree convection during the termination process. This weak convection might align the crystal lattice along the rotation axis due to the effect of ellipticity (Buffett, 2009). A numerical simulation of cessation has recently been given

by Deguen and Cardin (2011), although they question whether the accumulation of strain during cessation is sufficient to produce a texture.

Our results offer a possible scenario to explain a distinct innermost inner core. When convection occurs at the early stages of the inner core, but terminates well before present day, we might expect a distinct anisotropy associated with the innermost region of the inner core that experienced convection. Alternatively, termination of convection at a later stage of the evolution might explain the observation of a shallow isotropic layer on the order of 100 km overlying a fossil anisotropy associated with a previously convecting state.

It is tempting to infer the possibilities of compositional layering and heterogeneity from our thermo-chemical runs. The eventual growth of a light element layer after the ceasing of convection seems an explanation of the occurrence of a shallow, sharp, 0.6% fast layer (as observed in the eastern hemisphere, Waszek and Deuss (2011)). However, estimates of compositional layering in our model are small with density jumps on the order of several kg/m^3. The resulting variation in bulk sound speed due to such a density jump is on the order of 0.01%. We can assume that the effect on bulk modulus is similarly negligible, making these variations invisible to the seismological eye. A different mechanism explaining a far larger jump in light element composition would be required to explain the observed layering.

At the present time, no single dynamical model satisfactory explains all seismic observations of the inner core, including observations of anisotropy in seismic wave speed and attenuation and the innermost inner core. The occurrence of distinctive hemispheres has recently been explained by a convective translational motion from the western to the eastern hemisphere and a return flow in the outer core (Alboussière et al., 2010; Monnereau et al., 2010). This model is effective in explaining the isotropic and attenuation differences between the two hemispheres, but it does not explain the change in amplitude of the N-S oriented fast axis, as no deformation occurs when inner core translates. It is appealing to assume that a combination of a translational motion and convection within the inner core will localize downwelling and thus increase the lateral variations in deformation explaining the hemispherical complexity. The asymmetry in the translational motion could confine downwellings, and thus deformation, to the cold, growing hemisphere. Subsequently annealing towards the eastern hemisphere will reduce the amount of texture (Bergman et al., 2010). Whether these variations can explain seismically measurable variations requires a more in-depth study, accounting strain accumulation and development of seismic anisotropy due to texturing with realistic estimates of the elastic constants for iron. More shallow complexity of seismic anisotropy could arise by including of lateral variations in heat flow (Deguen et al., 2011). In principle, it should be possible to produce 3D models of seismic anisotropic using convection simulations. Theoretical models have been developed for degree two flow by Wenk et al. (2000) and for deformation due to anisotropic growth by Deguen et al. (2011). However, there is no suggestion that our smooth dynamical models (or any combination with other mechanisms) could explain the observed sharpness of the hemispherical boundary as seen at the top of the outer core (Waszek et al., 2011). Other explanations for a sharp hemispherical boundary might include a transition in phase or deformation mechanism.

6.6 Conclusions

Our parameterized model of the thermal history of the Earth's inner core shows that a convective episode is plausible for a range of cooling rates. Present-day convection is possible for high core-mantle boundary heat fluxes and low conductivity of iron. In addition, an initial phase of rapid growth can establish the thermal conditions that sustain thermal convection over much of the inner core history. This exemplifies why a full thermal history is needed to determine the occurrence of a thermally unstable state in the inner core. The numerical model illustrates the style of flow and the associated strains. Texturing of iron under these strains offer an explanation for the observations of seismic anisotropy, but observed anisotropy variations and patterns cannot be fully explained. The incorporation of an increasing amount of light elements is entrained and eventually mixed, but can eventually decrease the duration of convection. The dwindling strength of convection with time could explain the radial decrease of anisotropic strength and the growth of a shallow isotropic layer.

6.7 Afterword

After the publication of this work, a new study Pozzo et al. (2012) based on first principle calculations found iron (mixed with light elements) to have conductivities that are two or three times higher than previously estimated (Stacey and Loper, 2007), and than applied in this study. The main argument against the previous estimations is that they are based on large extrapolations in pressure. The new values change the conclusions of this study. Higher conductivities make thermal convection as described here less likely as cooling along the adiabatic becomes more effective. That the inner core is thermally stabilly stratified throughout its history becomes more likely.

It has also been recently proposed that compositional convection could occur in the inner core (Gubbins et al., 2013). Here, we assumed a stabilizing compositional effect, where the partitioning coefficients of light elements between the solid inner core and liquid outer core remain constant. Gubbins et al. (2013) propose partition coefficients that increase with decreasing temperatures as the inner core grows. This leads to an increase of light elements with radius, which can cause compositional instabilities at the top. This chemical driven convection provides an alternative scenario to create similar deformation regimes as proposed here and could possibly explain observed seismic anisotropy.

6.8 Acknowledgement

We would like to thank the authors of CitcomS and CIG for freely providing this open source finite element code. Additionally, this article has been significantly improved thanks

to comments and suggestions made by Peter Olson and two anonymous reviewers. We would also like to thank Ian Rose for discussion and post-processing scripts for the application of CitcomS.

Bibliography

Alboussière, T., Deguen, R., Melzani, M., 2010. Melting-induced stratification above the Earth's inner core due to convective translation. Nature 466, 744–747.

Alfè, D., 2010. Iron at Earth's core conditions from first principles calculations. Rev. Mineral. Geochem. 71 (1), 337.

Alfè, D., Gillan, M., Price, G., 2002. Ab initio chemical potentials of solid and liquid solutions and the chemistry of the Earths core. J. Chem. Phys. 116, 7127.

Alfè, D., Gillan, M., Price, G., 2007. Temperature and composition of the Earth's core. Contemp. Phys. 48 (2), 63–80.

Beghein, C., Trampert, J., 2003. Robust normal mode constraints on inner-core anisotropy from model space search. Science 299 (5606), 552.

Bergman, M., 1997. Measurements of electric anisotropy due to solidification texturing and the implications for the Earth's inner core. Nature 389 (6646), 60–63.

Bergman, M., Lewis, D., Myint, I., Slivka, L., Karato, S., Abreu, A., 2010. Grain growth and loss of texture during annealing of alloys, and the translation of Earths inner core. Geophys. Res. Lett. 37 (22), L22313.

Boehler, R., Santamara-Prez, D., Errandonea, D., Mezouar, M., 2008. Melting, density, and anisotropy of iron at core conditions: new x-ray measurements to 150 gpa. Journal of Physics: Conference Series 121, 022018.

Braginsky, S., Roberts, P., 1995. Equations governing convection in Earth's core and the geodynamo. Geophys. Astro. Fluid 79 (1), 1–97.

Buffett, B., 2002. Estimates of heat flow in the deep mantle based on the power requirements for the geodynamo. Geophys. Res. Lett. 29 (12), 7–1.

Buffett, B., 2009. Onset and orientation of convection in the inner core. Geophys. J. Int. 179 (2), 711–719.

Buffett, B., Huppert, H., Lister, J., Woods, A., 1996. On the thermal evolution of the Earths core. J. Geophys. Res 101, 7989–8006.

Buffett, B., Wenk, H., 2001. Texturing of the Earth's inner core by maxwell stresses. Nature 413 (6851), 60–63.

Calvet, M., Chevrot, S., Souriau, A., 2006. P-wave propagation in transversely isotropic media:: I. finite-frequency theory. Phys. Earth Plan. Int. 156 (1-2), 12–20.

Cao, A., Romanowicz, B., 2007. Test of the innermost inner core models using broadband PKIKP travel time residuals. Geophys. Res. Lett 34 (8).

Chandrasekhar, S., 1981. Hydrodynamic and hydromagnetic stability. Dover Pubns.

Cormier, V., 2009. A glassy lowermost outer core. Geophys. J. Int. 179 (1), 374–380.

Creager, K., 1992. Anisotropy of the inner core from differential travel times of the phases pkp and pkikp. Nature 356 (6367), 309–314.

Deguen, R., Cardin, P., 2009. Tectonic history of the Earths inner core preserved in its seismic structure. Nat. Geosc. 2 (6), 419–422.

Deguen, R., Cardin, P., 2011. Thermo-chemical convection in Earth's inner core. Geophys. J. Int. 187 (3), 1101–1118.

Deguen, R., Cardin, P., Merkel, S., 2011. Texturing in the Earth's inner core due to preferential growth in its equatorial belt. Phys. Earth Planet. Int. submitted.

Deuss, A., Irving, J., Woodhouse, J., 2010. Regional variation of inner core anisotropy from seismic normal mode observations. Science 328 (5981), 1018.

Dumberry, M., Bloxham, J., 2002. Inner core tilt and polar motion. Geoph. J. Int. 151 (2), 377–392.

Durek, J., Romanowicz, B., 1999. Inner core anisotropy inferred by direct inversion of normal mode spectra. Geophys. J. Int. 139 (3), 599–622.

Dziewonski, A., Gilbert, F., 1971. Solidity of the inner core of the Earth inferred from normal mode observations. Nature 234, 465–466.

Garnero, E., Helmberger, D., Grand, S., 1993. Constraining outermost core velocity with SmKS waves. Geophys. Res. Lett. 20 (22), 2463–2466.

Gubbins, D., Alfe, D., Davies, C., 2013. Compositional instability of Earth's solid inner core. Geophys. Res. Lett., DOI: 10.1002/grl.50186.

Irving, J., Deuss, A., 2011. Stratified anisotropic structure at the top of Earth's inner core: a normal mode study. Phys. Earth Plan. Int. 186 (1-2), 59–69.

Irving, J., Deuss, A., Woodhouse, J., 2009. Normal mode coupling due to hemispherical anisotropic structure in Earth's inner core. Geophys. J. Int. 178 (2), 962–975.

Ishii, M., Dziewonski, A., 2002. The innermost inner core of the Earth: Evidence for a change in anisotropic behavior at the radius of about 300 km. PNAS 99 (22), 14026.

Ishikawa, T., Tsuchiya, T., Tsuchiya, J., 2011. Stacking-disordered phase of iron in the Earth's inner core from first principles. Phys. Rev. B 83 (21), 212101.

Jacobs, J., 1953. The Earth's inner core. Nature 172, 297–298.

Jeanloz, R., Wenk, H., 1988. Convection and anisotropy of the inner core. Geophys. Res. Lett. 15 (1), 72–75.

Jephcoat, A., Olson, P., 1987. Is the inner core of the Earth pure iron? Nature 325, 332–335.

Karato, S., 1999. Seismic anisotropy of the Earth's inner core resulting from flow induced by maxwell stresses. Nature 402 (6764), 871–873.

Kawai, K., Tsuchiya, T., 2009. Temperature profile in the lowermost mantle from seismological and mineral physics joint modeling. Proceedings of the National Academy of Sciences 106 (52), 22119.

Kono, M., Roberts, P., 2002. Recent geodynamo simulations and observations of the geomagnetic field. Rev. Geophys 40 (4), 1013.

Konôpková, Z., Lazor, P., Goncharov, A., Struzhkin, V., 2011. Thermal conductivity of hcp iron at high pressure and temperature. High Pressure Research 31 (1), 228–236.

Labrosse, S., Macouin, M., 2003. The inner core and the geodynamo. Comptes Rendus Geosciences 335 (1), 37–50.

Labrosse, S., Poirier, J., Le Mouel, J., 2001. The age of the inner core. Earth Planet. Sc. Lett. 190 (3-4), 111–123.

Lay, T., Hernlund, J., Buffett, B., 2008. Core-mantle boundary heat flow, nat. Nat. Geosc. 1, 25–32.

Lehmann, I., 1936. P'. Bur. Cent. Seism. Int. Ser. A 14, 3–31.

McDonough, W., Sun, S., 1995. The composition of the Earth 1. Chem. Geol. 120 (3-4), 223–253.

Monnereau, M., Calvet, M., Margerin, L., Souriau, A., 2010. Lopsided growth of Earth's inner core. Science 328 (5981), 1014.

Morelli, A., Dziewonski, A., Woodhouse, J., 1986. Anisotropy of the inner core inferred from PKIKP travel times. Geophys. Res. Lett. 13 (13), 1545–1548.

Niu, F., Wen, L., 2001. Hemispherical variations in seismic velocity at the top of the Earth's inner core. Nature 410, 1081–1084.

Pozzo, M., Davies, C., Gubbins, D., Alfe, D., 2012. Thermal and electrical conductivity of iron at Earth's core conditions. Nature 455, 355–358.

Reaman, D., Daehn, G., 2011. Predictive mechanism for anisotropy development in the Earth's inner core. Earth and Planetary Science 312, 436–442.

Romanowicz, B., Li, X., Durek, J., 1996. Anisotropy in the inner core: Could it be due to low-order convection? Science 274 (5289), 963.

Sha, X., Cohen, R., 2010. First-principles thermal equation of state and thermoelasticity of hcp fe at high pressures. Phys. Rev. B 81 (9), 094105.

Sha, X., Cohen, R., 2011. First-principles studies of electrical resistivity of iron under pressure. J. of Phys.: Condensed Matter 23, 075401.

Shearer, P., 1994. Constraints on inner core anisotropy from pkp(df) travel times. J. Geophys. Res. 99, 19–19.

Sleep, N., 1988. Gradual entrainment of a chemical layer at the base of the mantle by overlying convection. Geophysical Journal 95 (3), 437–447.

Song, X., Helmberger, D., 1995. Depth dependence of anisotropy of Earths inner core. J. Geophys. Res 100, 9805–9816.

Souriau, A., 2009. Inner core structure: Constraints from frequency dependent seismic anisotropy. CR Geosci 341 (6), 439–445.

Stacey, F., Anderson, O., 2001. Electrical and thermal conductivities of fe-ni-si alloy under core conditions. Phys. Earth Plan. Int. 124 (3-4), 153–162.

Stacey, F., Davis, P., 2008. Physics of the Earth. Cambridge University Press.

Stacey, F., Loper, D., 2007. A revised estimate of the conductivity of iron alloy at high pressure and implications for the core energy balance. Phys. Earth Planet. Int. 161 (1-2), 13–18.

Stixrude, L., Brown, J., 1998. The Earth's core. Rev. Mineral. Geochem. 37 (1), 261.

Stixrude, L., Cohen, R., 1995. High-pressure elasticity of iron and anisotropy of Earth's inner core. Science 267 (5206), 1972.

Tackley, P., King, S., 2003. Testing the tracer ratio method for modeling active compositional fields in mantle convection simulations. Geochem. Geophys. Geosyst 4 (4), 8302.

Tan, E., Choi, E., Thoutireddy, P., Gurnis, M., Aivazis, M., 2006. Geoframework: Coupling multiple models of mantle convection within a computational framework. Geochem. Geophys. Geosyst 7 (6), Q06001.

Tanaka, S., Hamaguchi, H., 1997. Degree one heterogeneity and hemispherical variation of anisotropy in the inner core from pkp (bc)pkp (df) times. J. Geophys. Res. 102 (B2), 2925–2938.

Tateno, S., Hirose, K., Ohishi, Y., Tatsumi, Y., 2010. The structure of iron in Earth's inner core. Science 330, 359–361.

Tkalčić, H., 2010. Large variations in travel times of mantle-sensitive seismic waves from the south sandwich islands: Is the Earths inner core a conglomerate of anisotropic domains? Geoph. Res. Lett. 37, L14312.

Tromp, J., 1993. Support for anisotropy of the Earth's inner core from free oscillations. Nature 366 (6456), 678–681.

Turcotte, D., Schubert, G., 2002. Geodynamics. Vol. 2nd edn. Cambridge Univ Press.

Van der Hilst, R., De Hoop, M., Wang, P., Shim, S., Ma, P., Tenorio, L., 2007. Seismostratigraphy and thermal structure of Earth's core-mantle boundary region. Science 315 (5820), 1813.

van Orman, J., 2004. On the viscosity and creep mechanism of Earth's inner core. Geophys. Res. Lett. 31, L20606.

Vočadlo, L., Alfè, D., 2002. Ab initio melting curve of the fcc phase of aluminum. Physic Rev. B 65 (21), 214105.

Vočadlo, L., Alfè, D., Gillan, M., Price, G., 2003. The properties of iron under core conditions from first principles calculations. Phys. Earth Plan. Int. 140 (1-3), 101–125.

Vočadlo, L., Dobson, D., Wood, I., 2009. Ab initio calculations of the elasticity of hcp-fe as a function of temperature at inner-core pressure. Earth Planet. Sc. Lett. 288 (3-4), 534–538.

Waszek, L., Deuss, A., 2011. Distinct layering in the hemispherical seismic velocity structure of Earth's upper inner core. J. Geophys. Res. 116, B12313.

Waszek, L., Irving, J., Deuss, A., 2011. Reconciling the hemispherical structure of Earth's inner core with its super-rotation. Nature Geosc. 4 (4), 264–267.

Weber, P., Machetel, P., 1992. Convection within the inner-core and thermal implications. Geophys. Res. Lett. 19 (21), 2107–2110.

Wenk, H., Baumgardner, J., Lebensohn, R., Tomé, C., 2000. A convection model to explain anisotropy of the inner core. J. Geophys. Res. 105 (B3), 5663–5678.

Woodhouse, J., Giardini, D., Li, X., 1986. Evidence for inner core anisotropy from free oscillations. Geophys. Res. Lett. 13 (13), 1549–1552.

Yoshida, S., Sumita, I., Kumazawa, M., 1996. Growth model of the inner core coupled with the outer core dynamics and the resulting elastic anisotropy. J. Geophys. Res 101, 28085–28103.

Yukutake, T., 1998. Implausibility of thermal convection in the Earth's solid inner core. Phys. Earth Plan. Int. 108 (1), 1–13.

Zhong, S., Zuber, M., Moresi, L., Gurnis, M., 2000. Role of temperature-dependent viscosity and surface plates in spherical shell models of mantle convection. J. Geophys. Res. 105 (B5), 11063.

Chapter 7

Conclusion and Outlook

We have provided new evidence for strong heterogeneity and dynamics in the deep Earth. First, we mapped out the largest ultra-low-velocity zone to date (Chapter 2). This was done on the basis of the most striking postcursors seen in shear diffracted phases; postcursors delayed from the main phase by 30 to 50 seconds. This is the first time that the lateral extent of a ULVZ has been mapped out. To model the sharp velocity boundaries of this feature we used 3D seismic forward modeling of the full waveforms, instead of inversion techniques that assume smooth velocity variations.

The zone is about 900 km across, and has a velocity reduction around 20% compared to surrounding material. The zone of ultra-slow velocities behaves as a lens, refracting the waves that travel through, and creating the postcursors. The frequencies of the observed postcursors constrain the ULVZ to be on the order of 20-30 km high. While it remains unclear whether the slow velocities are a result of partial melting or iron enrichment, the wide aspect ratio and flatness of the zone determined here suggest that it is much denser than its surroundings.

The ULVZ is centered at 172.5°W and 17.5°N at the northern margin of the Pacific LLSVP. The location of this mega ultra-low-velocity zone beneath the hotspot with the strongest heat flux on Earth, the Hawaiian hotspot, might not be a coincidence. To date we have seen no such complexities in shear diffracted waveforms elsewhere, though many areas of the CMB are not probed by shear diffracted waves recorded at broadband seismic arrays.

Secondly, we looked into another slow feature, named the Perm anomaly (Chapter 3). Clustering of global tomographic models suggests this is a unique feature. We constrain characteristics of this anomaly by analyzing its lens-like behavior and the resulting amplitude increase and delay in the focused waveforms. This anomaly is more similar to an LLSVP in its height (100s of kilometers) and velocity reduction (on the order of several

percent) and therefore could be composed of comparable material[1]. Only in its lateral extent is it more like the Hawaiian ULVZ, and thus an anomalous feature besides the two large African and Pacific LLSVPs. Studying the existence of this feature in geodynamical models can give insight into the origin and history of the LLSVPs. As with our investigation of the Hawaiian ULVZ, our use of spectral element forward modeling allows us to retain strong velocity reductions in the lowermost mantle, while other methods would underestimate these.

Besides variations in isotropic velocities, there are variations in anisotropic velocities in the lowermost mantle. We have observed strong variations across the African LLSVP margin (Chapter 4). Here we see the presence of strong tilted anisotropy further away from the margin, and weakening or rotation of the anisotropy towards the margin. Within the LLSVP, there is no apparent anisotropy. These observations suggest that the material in the LLSVP is compositionally different and creates a mechanical boundary. Furthermore, the material within the LLSVP is either intrinsically isotropic, or the convection in the LLSVP is weak. The observations took advantage of the simplified polarization properties of shear diffracted waves at large distances. After the diffracted portion of the path, the vertical component has attenuated and it is purely horizontally polarized, so any change is due to interaction with anisotropy. Here we have confirmed our observations of a fast axis tilted northward by forward modeling full waveforms. The use of shear diffracted waves at large distances has improved our coverage of anisotropic observations in the lowermost mantle.

Global anisotropy maps of the D" region show that, in general, $V_{SH} > V_{SV}$ in most of the fast region. Interpreting any anisotropic observations in terms of flow, means we assume lattice preferred orientation due to deformation to be the cause. In Chapter 5, we have tested this assumption by modeling anisotropy produced in 2D and 3D geodynamical models. We have modeled the results for different mineral physical compositions based on different studies. We conclude that to explain the general pattern of radial anisotropy in the lower mantle as well as the strong isotropic velocity variations, postperovskite needs to be present. We also see that strong slip along the (001) plane in postperovskite appears most consistent with seismologically observed radial anisotropy. Besides radial anisotropy, shear wave splitting is different between perovskite and the different postperovskite models for shear waves traveling parallel and across the slab. In future work these need to be linked to local seismic observations of shear wave splitting.

Finally, in Chapter 6, we investigate whether thermo-chemical convection can be the reason for observed compressional seismic anisotropy in the inner core. An episode of convection is plausible for a range of thermal conductivities and core-mantle boundary heat flows during the early stages of inner core history. We numerically model the resulting convection and find that the resulting strains are high enough to produce preferred orientation in iron. It is difficult to explain lateral variations in anisotropy in such a model, but radial variations, particularly larger anisotropy in the innermost inner core, can be explained by

[1]In hindsight, by analogy, the Perm anomaly could have been named SLSVP- Small Low Shear Velocity Province

early termination of convection. Termination can occur earlier when thermal conductivity is higher, core-mantle boundary heat flux is lower, or by the increased partitioning of lighter elements into the inner core resulting in a compositionally stable stratification. Given the complexity of the seismic variations in the inner core, a more complex model combining a translating inner core with thermo-chemical convection as well as possible variations in phase or deformation mechanisms might need to be proposed.